Aqueously altered igneous rocks sampled on the floor of Jezero crater, Mars

K A Farley, K M Stack, D L Shuster, B H N Horgan, J A Hurowitz, J D Tarnas, J I Simon, V Z Sun, E L Scheller, K R Moore, et al.

Aqueously altered igneous rocks sampled on the floor of Jezero crater, Mars

K.A. Farley[1*], K.M. Stack[2], D.L. Shuster[3], B.H.N. Horgan[4], J.A. Hurowitz[5], J..D. Tarnas[2], J.I. Simon[6], V.Z. Sun[2], E.L. Scheller[1], K.R. Moore[1], S.M. McLennan[5], P.M. Vasconcelos[7], R.C. Wiens[8]†, A.H. Treiman[9], L.E. Mayhew[10], O. Beyssac[11], T.V. Kizovski[12], N.J. Tosca[13], , Kenneth H. Williford[14], L. S. Crumpler[15], L.W. Beegle[2], J.F. Bell III[16], B.L. Ehlmann[1], Y. Liu[2], J.N. Maki[2], M.E. Schmidt[12], A.C. Allwood[2], H.E.F. Amundsen[17], R. Bhartia[18], T. Bosak[19], A.J. Brown[20], B.C. Clark[21], A. Cousin[22], O. Forni[22], T.S.J. Gabriel[23], Y. Goreva[2], S. Gupta[24], S.-E. Hamran[17], C.D.K. Herd[25], K. Hickman-Lewis[26,27], J.R. Johnson[28], L.C. Kah[29], P.B. Kelemen[30], K.B. Kinch[31], L. Mandon[32], N. Mangold[33], C. Quantin-Nataf[34], M.S. Rice[35], P. S. Russell[36], S. Sharma[2], S. Siljeström[37], A. Steele[38], R. Sullivan[39], M. Wadhwa[16], B.P. Weiss[19,2], A.J. Williams[40], B.V. Wogsland[29], P.A. Willis[2], T. A. Acosta-Maeda[41], P. Beck[42], K. Benzerara[11], S. Bernard[11], A.S. Burton[43], E.L. Cardarelli[2], B. Chide[44], E. Clavé[45], E.A. Cloutis[46], B.A. Cohen[47], A.D. Czaja[48], V. Debaille[49], E. Dehouck[34], A.G. Fairén[50,51], D.T. Flannery[52], S.Z. Fleron[53], T. Fouchet[32], J. Frydenvang[54], B.J. Garczynski[4], E.F. Gibbons[55], E.M. Hausrath[56], A.G. Hayes[51], J. Henneke[57], J.L. Jørgensen[57], E.M. Kelly[41], J. Lasue[22], S. Le Mouélic[33], J.M. Madariaga[58], S. Maurice[22], M. Merusi[31], P.-Y. Meslin[22], S.M. Milkovich[2], C.C. Million[59], R.C. Moeller[2], J.I. Núñez[28], A.M. Ollila[60], G. Paar[61], D.A. Paige[36], D.A.K. Pedersen[57], P. Pilleri[22], C. Pilorget[62,63], P.C. Pinet[22], J.W. Rice Jr.[16], C. Royer[11], V. Sautter[11], M. Schulte[64], M.A. Sephton[24], S.K. Sharma[41], S.F. Sholes[2], N. Spanovich[2], M. St. Clair[59], C.D. Tate[51], K. Uckert[2], S.J. VanBommel[65], A.G. Yanchilina[66], M.-P. Zorzano[51]

1 Division of Geological and Planetary Sciences, California Institute of Technology, Pasadena, CA 91125 USA
2 Jet Propulsion Laboratory, California Institute of Technology, Pasadena, CA 91109 USA
3 Department of Earth and Planetary Science, University of California Berkeley, Berkeley CA 94720 USA
4 Department of Earth, Atmospheric, and Planetary Sciences, Purdue University, West Lafayette, IN 47907 USA
5 Department of Geosciences, Stony Brook University, Stony Brook, NY, 11794-2100, USA
6 Center for Isotope Cosmochemistry and Geochronology, Astromaterials Research and Exploration Science Division, NASA Johnson Space Center, Houston, TX 77058 USA
7 School of Earth and Environmental Sciences, University of Queensland, Brisbane, Queensland 4072 Australia
8 Planetary Exploration Team, Los Alamos National Laboratory, Los Alamos, NM 87545 USA
9 Lunar and Planetary Institute, Universities Space Research Association, Houston TX 77058 USA
10 Department of Geological Sciences, University of Colorado, Boulder, Boulder, CO 80309 USA
11 Institut de Minéralogie, de Physique des Matériaux et de Cosmochimie, Centre National de la Recherche Scientifique, Sorbonne Université, Muséum National d'Histoire Naturelle, 75005 Paris, France
12 Department of Earth Sciences, Brock University, St. Catharines, ON L2S 3A1 Canada
13 Department of Earth Sciences, University of Cambridge, Cambridge, CB2 3EQ, United Kingdom
14 Blue Marble Space Institute of Science, Seattle, WA 98104 USA
15 New Mexico Museum of Natural History & Science, Albuquerque, NM 8710 USA
16 School of Earth and Space Exploration, Arizona State University, Tempe, AZ 85287 USA
17 Center for Space Sensors and Systems, University of Oslo, 2007 Kjeller, Norway
18 Photon Systems Inc. Covina, CA 91725 USA
19 Department of Earth, Atmospheric and Planetary Sciences, Massachusetts Institute of Technology, Cambridge, MA 02139
20 Plancius Research, Severna Park, MD 21146 USA
21 Space Science Institute, Boulder, CO 80301 USA
22 Institut de Recherche en Astrophysique et Planétologie, Université de Toulouse 3 Paul Sabatier, Centre National de la Recherche Scientifique, Centre National d'Etude Spatiale, 31400 Toulouse, France
23 Astrogeology Science Center, U.S. Geological Survey, Flagstaff, AZ, USA
24 Department of Earth Sciences and Engineering, Imperial College London, SW7 2AZ United Kingdom
25 Department of Earth and Atmospheric Sciences, University of Alberta, Edmonton, AB, T6G 2E3, Canada
26 Department of Earth Sciences, The Natural History Museum, Cromwell Road, London, SW7 5BD, United Kingdom
27 Dipartimento di Scienze Biologiche, Geologiche e Ambientali, Università di Bologna, I-40126 Bologna, Italy
28 Johns Hopkins University Applied Physics Laboratory, Laurel, MD, 20723-6005, USA
29 Department of Earth and Planetary Sciences, University of Tennessee, Knoxville TN 37996

30 Dept. of Earth & Environmental Sciences, Lamont Doherty Earth Observatory of Columbia University, Palisades NY 10964 USA
31 Niels Bohr Institute, University of Copenhagen, DK-1350 Copenhagen, Denmark
32 Laboratoire d'Etudes Spatiales et d'Instrumentation en Astrophysique, Observatoire de Paris, Centre National de la Recherche Scientifique, Sorbonne Université, Université Paris Diderot, 92195 Meudon, France
33 Laboratoire de Planétologie et Géosciences, Centre National de la Recherche Scientifique, Nantes Université, Université Angers, F-44000 Nantes, France
34 Laboratoire de Géologie de Lyon : Terre, Université de Lyon, Université Claude Bernard Lyon1, Ecole Normale Supérieure de Lyon, Université Jean Monnet Saint Etienne, Centre National de la Recherche Scientifique, Villeurbanne, France
35 Department of Geology, Western Washington University, Bellingham, WA, 98225 USA
36 Department of Earth, Planetary, and Space Sciences, University of California Los Angeles, Los Angeles, CA 90095 USA
37 Department of Methodology, Textiles and Medical Technology, Research Institutes of Sweden, 11486 Stockholm, Sweden
38 Earth and Planetary Laboratory, Carnegie Science, 5251 Broad Branch Rd, Washington D.C. 20015 USA
39 Cornell Center for Astrophysics and Planetary Science, Cornell University, Ithaca, NY 14853 USA
40 Department of Geological Sciences, University of Florida, Gainesville, FL, 32611 USA
41 Hawai'i Institute of Geophysics and Planetology, University of Hawai'i at Mānoa, Honolulu, HI 96822 USA
42 Institut de Planétologie et Astrophysique de Grenoble, Centre National de la Recherche Scientifique, Université Grenoble Alpes, 38000 Grenoble, France
43 NASA Johnson Space Center, Houston, TX 77058 USA
44 Planetary Exploration Team, Los Alamos National Laboratory, Los Alamos, NM 87545 USA
45 Centre Lasers Intenses et Applications, Centre National de la Recherche Scientifique, Commissariat à l'Energie Atomique, Université de Bordeaux, 33400 Bordeaux, France
46 Centre for Terrestrial and Planetary Exploration, University of Winnipeg, Winnipeg, MB, Canada R3B 2E9
47 NASA Goddard Space Flight Center, Greenbelt MD 20771 USA
48 Department of Geology, University of Cincinnati, Cincinnati, OH, 45221-0013 USA
49 Laboratoire G-Time, Université Libre de Bruxelles, Brussels, Belgium
50 Centro de Astrobiología (Consejo Superior de Investigaciones Científicas - Instituto Nacional de Técnica Aerospacial), 28850 Madrid, Spain
51 Department of Astronomy, Cornell University, NY 14853 USA
52 School of Earth and Atmospheric Sciences, Queensland University of Technology, Brisbane, 4001 Australia
53 Department of Geosciences and Natural Resource Management, University of Copenhagen, DK-1350 Copenhagen, Denmark
54 Globe Institute, University of Copenhagen, Copenhagen, DK-1350 Denmark
55 Department of Earth and Planetary Sciences, McGill University, Montreal, Quebec H3A 0E8 Canada
56 Department of Geoscience, University of Nevada, Las Vegas, Las Vegas, NV, 89154 USA
57 National Space Institute, Technical University of Denmark, 2800 Kongens Lyngby, Denmark
58 Department of Analytical Chemistry, University of the Basque Country, 48940 Leioa, Spain
59 Million Concepts, Louisville, KY 40204, USA
60 Los Alamos National Laboratory, Los Alamos, NM 87545 USA
61 Institute for Information and Communication Technologies, Joanneum Research, Steyrergasse 17, 8010 Graz, Austria
62 Institut d'Astrophysique Spatiale, Université Paris-Saclay, Orsay 91405, France
63 Institut Universitaire de France, Paris, France
64 Mars Exploration Program, Planetary Science Division, NASA Headquarters, Washington DC 20546
65 McDonnell Center for the Space Sciences, Department of Earth and Planetary Sciences, Washington University in St. Louis, St. Louis, MO, 63130 USA
66 Impossible Sensing, LLC.; 2700 Cherokee Street, St. Louis MO 63118 USA

Abstract: The Perseverance rover landed in Jezero crater on Mars to investigate ancient lake and river deposits. Here we report observations of the crater floor, below the crater's sedimentary delta, showing it consists of igneous rocks altered by water. The lowest exposed unit, informally

named Séítah, is a coarsely-crystalline olivine-rich rock accumulated on the floor of a magma body. Fe-Mg carbonates along grain boundaries indicate reaction with CO_2-rich water under water-poor conditions. Overlying Séitah is a unit informally named Máaz, interpreted as lava flows or as the chemical complement to Séitah in a layered igneous body. Voids in these rocks contain sulfates and perchlorates likely introduced by later near-surface brine evaporation. Core samples of these rocks were stored aboard Perseverance for potential return to Earth.

The Perseverance rover, part of the Mars 2020 mission, landed on the floor of Jezero crater on 2021 February 18. Perseverance was designed to characterize the geology, investigate records of past climate, and seek evidence of possible ancient life contained in rocks laid down when Martian surface conditions were more habitable than today (*1*). The multi-year mission is intended to select, collect and document about 35 rock and soil samples that may be transported to Earth by future missions for further analysis (*1*). We report results from the science campaign which ran until mission sol (Martian day) 290, exploring the geology and geochemistry of the Jezero crater floor geological units. These rocks, which form part of a regional stratigraphy unique on Mars, record an ancient period when impact cratering, volcanism, and water were actively shaping the surface of the planet.

Jezero crater, with a diameter of 45 km, lies on the western flank of Isidis, a giant impact basin of Noachian age (~4.0 Ga; (*2*)) and northeast of Syrtis Major, a younger shield volcano (*3*). Jezero was formed by an impact onto an early Noachian basement unit that includes Isidis impact deposits (*3–6*). The crater later hosted an open basin lake, fed by a large system of river valleys that were active in the late Noachian (~3.6-3.8 Ga; (*7*)) to early Hesperian (>3.2 Ga; (*8*)). Sediments delivered by those rivers into the crater lake produced a clay and carbonate bearing delta, which appears to be well preserved (*4*, *8–10*). The valleys that fed Jezero pass through a regional stratigraphy that includes an olivine-bearing unit, partially altered to carbonate (*11*, *12*), that overlies the Noachian basement. The olivine unit is in turn overlain by a low albedo crater-retaining unit, with spectral signatures of pyroxene (*5*, *13*). Mars's three largest impact basins are each surrounded by such olivine-bearing rocks (*14*); the olivine unit on the southern and western margins of Isidis basin is the largest contiguous olivine-rich unit on Mars, with several hypothesized origins: impact melt (*3*, *5*), extrusive or intrusive magmatism (*15–17*), volcanic ash fall (*18*), pyroclastic surge deposition (*19*), and detrital sedimentation (*20*).

Rock units potentially equivalent to this regional stratigraphy occur on the floor of Jezero crater (*9*, *21*). Orbital mapping of the Jezero crater interior (*21*) prior to landing delineated a pyroxene-bearing unit with a high density of superposed impact craters named Crater Floor Fractured Rough (hereafter Cf-fr), and an olivine-bearing unit named Crater Floor Fractured 1 (Cf-f-1). Perseverance directly accessed these two geologic units (**Fig. 1B**). The rocks of Cf-fr, informally named the Máaz formation, have been interpreted to be lava flows (*9*, *22*) or sandstones deposited by flowing water or wind (*21*, *23*). Crater counting on this unit constrains the ages of Jezero crater floor rocks, but studies have yielded inconsistent age estimates from 1.4 to 3.45 Ga (*9*, *22*, *24*). The spatially heterogeneous crater density on this unit (**Fig. 1B**) is likely the origin of this age discrepancy, and indicates the Máaz formation experienced a complex history of surface exposure. Olivine-bearing rocks occur outside Jezero crater, draping across the rim, and within the crater (*9*). The olivine-bearing rocks of the Cf-f-1 unit, informally named the Séítah formation, have been proposed to share an origin with the regional olivine-bearing unit (*9*, *21*,

25) possibly reworked or chemically modified by water within Jezero crater (*21*, *23*). Although the Séítah formation has been interpreted as older than the delta and its associated lake (*21*, *23*, *26*), the age of the Máaz formation relative to the delta is debated. The Máaz formation has been interpreted as one of the youngest units in the crater, post-dating all delta deposition (*28*), or as substantially older, predating the delta (*21*, *23*, *27*). Much of the Séítah formation is topographically higher than the Máaz formation, but previous studies agree it is nonetheless older (*23*, *27*).

During atmospheric entry, the Mars 2020 spacecraft's Terrain Relative Navigation system (*28*) autonomously selected the highest probability safe landing site available, which was at 18.4447°N, 77.4508°E, between the heavily cratered Máaz terrain to the east and the abundant aeolian bedforms of the Séítah terrain to the west (**Fig. 1**). The informally named Octavia E. Butler landing site (OEB) lies on a narrow strip of smooth topography, about 2 km SE of the delta scarp and within tens of meters of the Séítah-Máaz geologic contact. Neither the cratered terrain of the Máaz formation nor the rugged sandy terrain of the Séítah formation are suitable for rover operations, but a narrow smooth strip of Máaz rocks near their contact provided a traversable pathway for the mission's first science campaign. After completion of hardware commissioning and demonstration flights of the *Ingenuity* helicopter, in June 2021 the rover embarked on an out-and-back journey to the south and then west, with the goal of documenting the two formations. This route provided access to abundant surface exposure of Máaz rocks and more limited exposures of Séítah bedrock, along with a scarp informally named Artuby ridge that delimits the two units (Fig. 1C).

Observations

We used Perseverance to acquire co-located textural, compositional and mineralogical maps at both the microscopic and outcrop scale along a 2.4 km traverse of the Jezero crater floor. Subsurface structure was imaged with ground penetrating radar (*29*). We characterized the natural surfaces of rock outcrops along the rover traverse using the Mastcam-Z multi-spectral stereo camera (*30*), the WATSON (Wide Angle Topographic Sensor for Operations and eNgineering (*31*) microscopic camera, and Supercam laser-induced breakdown and visual-infrared spectroscopy (*32*). These instruments are most effective if there is little coating of rock surfaces by dust and other materials. When dust coating is thicker, and for the proximity science instruments, the SHERLOC (Scanning Habitable Environments with Raman & Luminescence for Organics & Chemicals) Raman and fluorescence spectrometer (*31*) and the PIXL (Planetary Instrument for X-ray Lithochemistry) X-ray fluorescence spectrometer (*33*)), rocks were studied after abrading a ~5 cm diameter, ~1 cm deep circular pit into each target. Debris was removed from the resulting abrasion patch using compressed N_2 gas (*34*). Proximity observations were taken at four abrasion sites (informally named Guillaumes, Bellegarde, Garde, and Dourbes; **Fig. 1B**); sample collection was attempted at each of these sites except Garde.

Outcrop and Geologic Descriptions of Máaz and Séítah formations

Máaz

The Máaz formation consists of blocky, massive, and layered bedrock (**Figs. 2 and S1**). Natural surfaces of Máaz formation rocks contain occasional mm-size grains and mm-to-cm-sized voids or pits. Many Máaz formation outcrops appear polished and grooved by aeolian abrasion. Others appear to be failing along concentric fractures consistent with spheroidal weathering (**Fig. S1C**). Máaz rocks are often partially covered by regolith, dust and sometimes a discontinuous purple coating or rind (**Fig. 3A**); rock textures are more clearly observed on mechanically abraded surfaces. Sedimentary structures formed by grain transport, such as migrating ripples and dunes, were not observed within this formation.

The Roubion member is exposed at the lowest elevation along the traverse and we therefore infer it to be the oldest interval of the Máaz sequence (**Fig. S5**). This member is comprised of meter-scale low-lying (<5 cm of relief) rock surfaces, which are polygonally fractured. The Guillaumes abrasion patch was performed on such an outcrop of the Roubion member; it reveals light and dark grains with a pervasive but heterogeneously distributed brown tint (**Fig. 3A**). In the least brownish regions, we observed mm-size interlocking dark gray/green and light-toned prismatic grains, with no evidence of intergranular porosity or visible cement. Though sometimes elongated, grains show no preferred orientation. If it is igneous, the relatively coarse grains suggest a moderately slow cooling rate (i.e., it is a holocrystalline or microgabbroic rock). Irregularly shaped voids or pits, up to 5 mm in diameter, are present within the abrasion patch, as are elongated crevices. The edges of these features, and several other areas on the abrasion surface, appear coated by a smooth red-brown or black mantle that partially or completely obscures underlying grains. In addition, many of the lighter-toned grains are variably stained reddish-brown. Mm-sized irregularly shaped patches of bright white material, some also stained brown, occur between grains, likely in filled voids, and as a surface coating on some of the prismatic grains. Collectively, these observations are consistent with an igneous rock that has experienced aqueous alteration (modification by reactions with water).

Up-section and westward along Artuby ridge, a ~1 km long linear scarp that reveals 2-3 meters of southwest-dipping stratigraphy on its northeastern side **(Fig. 2B)**, the Roubion member transitions into the Artuby member, distinguished by the presence of distinct layering. The Artuby member is composed of decimeter-thick layers with rounded protrusions and an apparently coarse granular surface texture, though this is sometimes obscured by regolith (**Fig. 2, S1**). The thick layers are separated by, and sometimes transition laterally into, thin recessive sub-cm-scale layers. The layered rocks of the Artuby member are typically overlain by a resistant caprock, the Rochette member, that can be traced laterally over hundreds of meters along the crest of Artuby ridge. This caprock also appears to extend southward from the ridge as fragmented blocky flat-lying exposures partially covered by regolith (**Fig. 1B**). The Rochette member is ~30-50 cm thick and sometimes appears structureless, but more commonly exhibits cm-scale layering. At an outcrop informally named Mure (**Fig. S1D,E),** the Rochette caprock exhibits thin layers that pinch out below more massive layers, and a ~2 cm wide chain of pits (possibly vesicles) that for ~75 cm traces the curvature of the layer in which it is enclosed. A second abrasion patch, Bellegarde, was performed on a tabular boulder of the Rochette member, on the crest of Artuby ridge. Bellegarde is characterized by smaller crystals (~0.5 mm) of similar appearance to Guillaumes (**Fig. 3**). These crystals are occasionally stained by a reddish-brown

material that is less pervasive than in Guillaumes but appears otherwise similar. Irregular white patches are also present, but there are no large pits or thick dark coatings in Bellegarde.

Resistant, blocky caprocks, like those of the Rochette member, are also observed in several ~1-2 m high scarps along the eastern edge of Séítah (west/southwest of OEB). Here, the Rochette member appears to be overlain by disaggregating low relief polygonal outcrops of the Nataani member. Rocks of the Nataani member appear morphologically and lithologically similar to the underlying Roubion member, but are distinct in their geographic extent, elevation, and inferred local stratigraphic relationships (**Fig. 1b and Fig. S5**). The low relief Nataani member transitions eastward and up-section into the boulder-forming hills of the Chal member. East of OEB and the southbound rover traverse, massive sub-meter to meter-scale boulders of the Chal member erode from hilly outcrops, with no signs of internal layering. This rough terrain extends to cover most of the crater floor and is associated with the highest crater densities observed within Jezero (**Fig. 1B**).

Séítah

Bedrock exposure of the Séítah formation is mostly limited to ~1 to 10 meter-tall ridges trending northeast-southwest, with the remainder of the region covered by sand ripples, loose rocks and boulders (**Fig. 4, S2**). The Séítah formation is comprised of the strongly layered Bastide member and the overlying Content member, which is structureless and characterized by abundant mm to cm size pits **(Fig. S2A)**. Long distance imaging shows that the Bastide member is widespread and exposed in outcrops throughout the several square kilometers of observed Séítah formation. Most layers of the Bastide member are 1-3 cm thick, but the thickest layers are apparently structureless over thicknesses of 10-40 cm. Thinner layers sometimes transition laterally into massive outcrops. There is an apparent thickening-upward trend within the Bastide member, in which thinly layered rocks transition up-section into thicker layered rocks that cap ridges (**Fig S2C**). Most layers are generally tabular and even in thickness, with planar layer-bounding surfaces, though some exhibit cm-scale undulations. Individual layers can sometimes be traced laterally over distances of several meters within an individual outcrop, but individual layers and distinctive sets of layers usually cannot be correlated between outcrops. We identified no indicators of transport by wind or water, such as planar lamination and ripple or dune-cross stratification. The pitted rocks of the overlying Content member do not exhibit layering, and lack olivine (see below). The Content member is observed only locally, exposed over lateral distances no greater than several meters. Its contact relationship with the Bastide member is unknown.

Natural surfaces of Bastide member outcrops show densely packed, clast-supported, homogenous 2-3 mm diameter dark grey or green grains (or crystals) with indistinct, lighter-toned material between grains (**Fig. 4C**). The grain size distributions do not vary across multiple outcrops, nor did we visually detect grain-scale sorting or grading at apparent layer boundaries. The mm-sized grains, when observed in abraded surfaces of Bastide (the Dourbes and Garde abrasion patches), are light-toned and mostly equant, but some elongated grains are also present (**Fig. 3C)** (37); we observed no gradation in grain size in the abrasion patches. Less common than the light-toned grains are slightly smaller dark gray-green grains that are sometimes angular, but more often appear to fill the space between lighter grains. Light brown material stains the light-toned grains and is concentrated between grains, in some cases encircling or rimming them.

A few sub-mm scale bright white patches are also present. Although a few natural surfaces of Bastide member rocks contain mm-scale pits, the occasional voids in the two abraded surfaces are much smaller.

Near the base of Artuby ridge, at the transition between the Máaz and Séítah formations, Séítah layering is observed both in outcrop and in the subsurface with ground penetrating radar. The layering typically dips ~10-15^{o} to the southwest (**Fig. S3**). These dips are consistent with those of Máaz formation rocks exposed along Artuby ridge. This indicates that Séítah formation bedrock lies stratigraphically below Máaz formation rocks, even though the Máaz formation is topographically lower than some Séítah exposures, confirming a pre-landing hypothesis (23). Thus, the Séítah formation is the lowest exposed stratigraphic unit on the Jezero crater floor, and is overlain by the Máaz formation. The boundary between the Séítah and Máaz formations is obscured by regolith, so it is unknown whether the units are separated by an unconformity. The inferred contact between the two units varies in elevation, by ~10 m along Artuby ridge and up to ~30 m around the entire Séítah exposure.

Máaz formation Geochemistry and Mineralogy

Mastcam-Z multispectral observations (*30*) of Máaz formation rocks along the traverse show broad absorption bands centered near 0.88-0.90 um, consistent with pyroxene or Fe^{+3}-bearing alteration minerals (**Fig. S4**). This is similar to the weak pyroxene bands observed from orbit across the eastern portion of the crater floor (*9*, *35*). 77 Máaz formation targets were analyzed with Supercam infrared (IR) spectroscopy (*32*); these frequently show a band at 1.92-1.93 μm, which we attribute to hydrated iron oxides, ferric smectites, and/or hydrated salts (**Fig. S6,** (*36*)). Weaker absorption features observed at 1.42 and 2.28 μm are consistent with Fe-OH bands in hydrated silicates (*36*).

Supercam laser-induced breakdown spectroscopy (LIBS, (*32*)) was used to characterize the elemental composition of 67 Máaz formation targets. At its typical operating distance of 2.7 meters from the rover, the laser beam interrogates a region ~350 um in diameter at each of the 5 to 10 observation points investigated on each rock target. In some cases, individual points had elemental abundances consistent with specific minerals rather than mixtures. From these we infer the presence of common igneous minerals (augite, plagioclase, ilmenite, ferrosilite, and unidentified iron oxides), at least some of which are moderately coarse grained (>350 um). No IR spectra or LIBS compositions consistent with olivine were observed in Máaz formation bedrock. **Fig. S8** shows the average composition of each analyzed rock target, which indicates that the Máaz formation is fairly homogenous and dominated by varying proportions of plagioclase and augite. The average LIBS-based composition of Máaz (**Table S1)** is broadly basaltic, with 48% SiO_2, low MgO (3 wt %) and high (20 wt %) FeO_T (total iron as Fe^{+2}).

PIXL X-ray fluorescence mapping (*33*) shows (Fig. 5) that the Guillaumes (Roubion member) and Bellegarde (Rochette member) abrasion patches are dominated by two distinct 0.5-1 mm scale common igneous phases. The blocky to prismatic white grains (**Fig. 3**) are chemically consistent with plagioclase (Al-rich regions in **Fig. 5A**), while the darker grains have the composition of pyroxene (specifically augite, Ca-rich regions). Also present are 100 um scale regions indicative of FeTi oxides and Ca phosphates. The red-brown to black material consists

mostly of Fe and Si, with molar Fe/Si ratios ranging from ~0.7 to 1.5 and MgO and Al_2O_3 both <4%. This composition overlaps with some igneous Fe-silicate minerals, such as Fe-bearing pyroxene and olivine, but is also consistent with several secondary Al-free Fe-silicates, such as greenalite, hisingerite, and cronstedtite. Alternatively, this material may be a mixture of iron oxide and silicates; Mastcam-Z multispectral data indicates the presence of hematite and/or goethite in both Máaz abrasion patches (**Fig. S4**). Coupled with its elemental composition, the color and textural properties of this material (**Fig. 3**) suggest in-situ aqueous alteration of one or more primary igneous minerals.

Raman spectroscopy indicates that the bright white void-filling material in the Máaz formation abrasion patches is at least partially composed of hydrous Ca-sulfate and Na-perchlorate, sometimes co-located with each other (**Fig. S7 A,B**). Elemental abundances support these identifications; a phase with molar Na/Cl ratio of about unity is consistent with Na-perchlorate, halite, or both.

In the average bulk composition of the Máaz abrasion patches (**Table S2**), the SO_3 ~ 3.0 wt % and Cl ~2.6 wt % are both far higher than typical unaltered Martian igneous rocks (*37*); if Máaz consists of igneous rocks, they have experienced addition of S and Cl-bearing materials. To estimate the primary chemical compositions of Guillaumes and Bellegarde, we computed a subset average of PIXL data by excluding salt-rich bright white areas (**Fig. 3;** (*38*)). This alteration-free compositional average (**Table S2**) indicates that the primary Máaz formation rocks were basaltic in composition, based on total alkalis and silica. Compared to Earth basalts, Máaz rocks are enriched in FeO_T (22 wt %) and P_2O_5 (2.2 wt %). Compositions estimated by X-ray fluorescence, which represent the analysis of just a few mm^2 of rock, are similar to the average composition of all Máaz formation rocks obtained by LIBS (Fig. S8).

Séítah formation Geochemistry and Mineralogy

Mastcam-Z multispectral images and Supercam IR spectra of Bastide member rocks of the Séítah formation are dominated by a broad 1 um absorption feature indicating olivine (**Fig. S4**). IR spectroscopy also shows a 1.9 um feature similar to, but weaker than, observed in Máaz formation rocks, which we attribute to mineral hydration (**Fig. S6,** (*36*)). Individual LIBS points on the prominent 2-3 mm grey-green grains observed on natural surfaces (**Fig. 3C**) commonly have compositions approaching those of pure olivine. The target-averaged LIBS compositions of 25 Bastide member rocks extend from olivine towards mixtures of augite and plagioclase (**Fig. S8**). The Bastide member compositions have only minor overlap with the dominantly plagioclase-augite Máaz formation rocks. The overall mean composition of all Bastide member targets is listed in **Table S1**.

Raman spectra of the Bastide member abrasion patches (Dourbes and Garde) confirm the abundant presence of olivine (**Fig. S7 C**). XRF elemental mapping (performed on Dourbes only;

Fig. 5B) indicates that 65% of the analyzed surface, associated with the light-toned grains (**Fig. 3**), is chemically consistent with approximately Fo_{55} olivine (i.e., 55% Mg and 45% Fe on an atom basis) (*39*). The olivine is partially surrounded with, and sometimes enclosed by, dark green augite (13% of the analyzed surface). A companion paper (*39*) interprets this relationship as consistent with poikilitic igneous texture in which late-forming augite grows around density-segregated olivine. Al-rich areas comprising 10% of the analyzed surface likely include feldspars; 0.1 mm scale phosphates and Cr- and Ti-bearing Fe-oxides are also present. The reddish-brown material that occurs between grains (**Fig. 3C**) is chemically complex. It often has Raman peaks consistent with carbonate, frequently associated with olivine peaks (**Fig. S7**). In other instances, Raman spectra consistent with hydrated sulfate (**Fig. S7**) yield Mg/S ratios that indicate the presence of $MgSO_4$. In elemental maps, the brown areas sometimes contain low SiO_2, elevated abundances of Fe and Mg, and low analytical oxide totals, consistent with carbonate with approximate composition $Fe_{0.5}Mg_{0.5}CO_3$. Raman signatures of the rare white patches indicate the presence of hydrated Ca and Mg sulfates and perchlorate (**Fig. S7**). A broad Raman signature at around 1020 cm^{-1}, widely distributed in the abrasion patch, is potentially amorphous silicate (**Fig. S7 G**).

Séítah formation rocks, like those of Máaz, appear to consist of primary igneous minerals (e.g., olivine, augite, plagioclase) and secondary aqueous alteration phases (carbonate, sulfates). Excluding material that is likely transported from elsewhere (*38*), the mean primary composition obtained by PIXL on Dourbes is ultramafic, with 20 wt% MgO and 40 wt% SiO_2 (**Table S2)**. Compared to the Bastide member LIBS average, this composition has lower SiO_2 and higher FeO, but is otherwise similar.

In contrast to the Bastide member targets, LIBS measurements of the Content member appear to be dominated by augite and feldspar, with no olivine. This is consistent with the appearance of this rock, which lacks the coarse grey-green olivine grains characteristic of the Bastide member. Only limited data on this member was acquired.

Interpretations and Hypotheses

Origins of Máaz and Séítah formations

We interpret the Bastide member of the Séítah formation as igneous. The grain size and high modal abundance of olivine, coupled with the poikilitic texture, indicate an olivine cumulate in which pyroxene, plagioclase, and primary Fe-Ti-Cr oxides crystallized from residual melt (*39*). These characteristics indicate slow cooling, differentiation, and crystal settling (*40*). Therefore, Bastide member rocks likely crystallized in a thick lava flow, a lava lake or impact melt sheet, or in an intrusion. On Earth, variations in crystal size or modal mineralogy define layers that often give cumulate rocks a sedimentary appearance in outcrop (*40*, *41*). Imaging, spectroscopic and LIBS observations revealed no evidence for such differences among Bastide layers, nor at their interface. The prominently layered appearance of the Séítah formation (**Fig. 4**) could arise from layer-parallel cooling joints, differential aqueous alteration, or subtle variations in rock composition or texture that enhance near-horizontal fracturing. Such features are likely to have

been accentuated by erosional processes, especially wind abrasion. This interpretation implies that the layering in Séítah corresponds to magmatic layering.

Based on their mineralogy, texture, and bulk composition, rocks of the *Máaz* formation are also most consistent with a primary igneous, rather than sedimentary, origin. We exclude the possibility that Máaz consists of basaltic sandstones due to the lack of sorting among grains of different size and specific gravity, the interlocking grain texture, the lack of evidence for pervasive intergranular porosity or cements in the Guillaumes and Bellegarde abrasion patches, and the apparent absence of subaqueous or aeolian transport features.

On Earth, the high abundance of olivine in olivine cumulate rocks is usually complemented by less mafic (i.e. less ferromagnesian) and commonly overlying materials that together constitute the parental melt composition (*40*). Within Jezero crater, rover observations, and more spatially extensive orbital spectroscopy (*35*), indicate the high olivine abundances characteristic of the Bastide formation are also found throughout Séítah, with olivine poor rocks (like the Content member) being rare. Thus, if a less mafic complement to the Bastide member previously existed in this region, it must have been at least partially removed by erosion. The Máaz formation could be the remnant of such a complement - it has abundant pyroxene and plagioclase, little magnesium, is moderately coarsely crystalline, and lies stratigraphically above the Bastide member, all as expected if the two units originated from a single differentiated igneous melt. The various members of the Máaz formation could be equivalent to layers in the igneous body.

As an alternative, the Máaz formation could be a sequence of younger basaltic lavas that flowed up against, and at least partially overtopped, the Séítah formation after erosional removal of the putative less mafic complement. The morphologically distinct Máaz members could then be cogenetic lava flows, with variable properties related to composition and/or eruption temperature. An extrusive igneous origin for Máaz would account for some of its morphologies and textures, e.g. the lobate structures in the Artuby member (**Fig. 2B**), possible vesicles in Guillaumes (**Fig. 3A**), and in the chain of pits in the Rochette member (**Fig. 2**). Variations in elevation of the Máaz - Séítah contact could reflect underlying topography of the Séítah formation on which the Máaz lavas were erupted. However, other features are less characteristic of lava flows, such as the cm-scale layers observed in the Rochette and Artuby members, and the lack of flow-orientation of elongated grains in the Máaz abrasion patches (**Fig. 3**).

The limited data on the Content member of the Séítah formation make it difficult to define its origin. It could also be a remnant of a once more expansive less-mafic complement to Bastide; a remnant of Máaz formation lava flows that overtopped the Bastide member; or remnant sedimentary rocks deposited atop the Bastide member.

Multiple sources of melting are possible for the igneous crater floor units within Jezero, and present data are insufficient to discriminate between the possibilities. The impact that created Jezero could have produced a sufficiently deep melt sheet to differentiate into an olivine cumulate, but we have found no evidence of associated impact breccias on the crater floor, and crater scaling relationships suggest the original Jezero floor is buried by about a kilometer of post-impact basin-filling materials (*4*, *22*). Although Jezero is close to the Isidis impact basin, and Bastide member petrology is similar to hypothesized olivine-rich cumulates in a melt sheet

potentially created by the Isidis impact (*3, 5*), Isidis cannot be the source since Jezero post-dates Isidis. There are no other impact basins of appropriate age, size and proximity to Jezero to be plausible sources. Alternatively, melting could have occurred without an impact, especially in the early Hesperian when the Martian mantle was substantially hotter than present. This is thought to be the origin of the nearby Syrtis Major shield volcano (*42*).

Magmas could have been introduced into Jezero crater over the rim or from below. Although the Jezero crater rim has been extensively eroded, materials like those in the Bastide member have been interpreted as draping its western side (9), and we suggest that hills on the southeast rim of Jezero could be of volcanic construction. However, these features are not contiguous with the Séítah formation. We consider the most likely scenario to be fissure-fed eruptions occurring both within Jezero and in the surrounding region. By analogy to some volcanically filled craters on the Moon (*43*) and other craters on Mars (*44*), magma injection could have occurred directly into the low-density materials of the crater floor at any time after Jezero formation. This process could lead to intrusive and/or extrusive igneous activity (*43*).

Séítah formation rocks were previously proposed to be part of a ~70,000 km^2 olivine-rich region associated with Isidis basin (*15, 18, 45, 46*). The widespread distribution of this olivine-rich material, apparent draping across topography, poor crater retention, and limited regolith cover have been interpreted as indicating a clastic origin (*5, 18–20*). That interpretation is difficult to reconcile with our conclusion that the Séítah formation is a slowly cooled magmatic differentiate. Despite their similarities, the regional olivine unit could have a distinct origin from Séítah. Alternatively, widespread injection and differentiation of compositionally similar magmas might have occurred throughout the region.

Aqueous processes

After emplacement of the igneous rocks on the crater floor, multiple forms of aqueous interaction modified but did not destroy their igneous mineralogy, composition, and texture. Evidence for alteration includes the presence of carbonate in the Séítah abrasion patches, the iron oxides in the Máaz formation abrasion patches which we presume are due to iron mobilization and precipitation, and the deposition of salts including sulfates and perchlorate. More broadly, the appearance of possible spheroidal weathering textures (**Fig. S1C**) suggests that aqueous alteration played a role in rock disintegration (*47*).

The similarity of Fe/Mg ratios in the carbonates and olivine within the Dourbes abrasion patch, rimming of olivine by carbonate, and their possible association with likely amorphous silicate are all consistent with in-situ olivine carbonation, in which olivine reacts with CO_2-rich water to produce this phase assemblage in close physical proximity (*48–50*). Olivine carbonation often occurs together with conversion of olivine to serpentine group minerals (serpentinization), but in the Séítah formation we have found no evidence for such minerals. The similarity of olivine and carbonate cation compositions, and the survival of substantial abundances of olivine, indicate aqueous alteration under rock-dominated conditions, possibly occurring over a short duration.

Olivine carbonation can occur over a broad range of temperatures, from hydrothermal or metamorphic conditions to low-temperature weathering (*11*). The presence of carbonate places a lower bound on fluid pH that depends on the concentrations of cations and dissolved inorganic carbon (*51, 52*). For example, if Mg and Fe concentrations ranged from 10^{-4} to 10^{-2} mol kg^{-1} and the initial dissolved inorganic carbon equilibrated with 0.1 to 10 bar CO_2(g), the pH would have a lower limit of 5.5-7.5 (at 25^{o}C).

Although we have found no evidence for carbonate in the Máaz formation abrasion patches, the abundant dark mantling material (**Fig. 3A**) could be a secondary serpentine group mineral produced by aqueous alteration of Fe-rich pyroxene or olivine (*53*). The presence of secondary Fe silicate without high abundances of carbonate in Máaz formation rocks could indicate a fluid with lower dissolved inorganic carbon concentrations than we inferred for the Séítah formation. These Fe silicates can also form across a wide range of temperatures, from ambient to hydrothermal; we cannot constrain the emplacement conditions without knowing the precise mineral composition. Alternatively, the Fe-rich materials could represent films of Fe oxides or oxyhydroxides coating and penetrating primary silicates, such that our elemental measurements include both phases. On Earth, iron staining of rocks is common when reduced Fe is released from aqueously altered igneous phases and then precipitated under oxidizing conditions. For example, sulfide dissolution by oxidizing solutions commonly yields hematite or goethite while simultaneously mobilizing sulfate (*54*).

Sulfate minerals, sodium perchlorate, and possibly other salts (e.g., halite) indicate that other styles of aqueous activity also occurred in the crater floor igneous formations. These salts fill pore spaces, voids, and cracks that themselves might have resulted from aqueous alteration, e.g., from volume expansion accompanying carbonation/serpentinization (*55*), dissolution of phases such as sulfides, or by chemical and physical erosion processes producing open space (such as the pits in Guillaumes). We have not observed sulfides, but if they were once present, their alteration could have contributed to the production of Ca, Mg, or Fe sulfates or mixtures of them in situ. However, the high sulfate concentrations observed in Guillaumes and Bellegarde suggest an external source for at least some of the sulfates. As has been proposed for rocks at Gale crater investigated by the Curiosity rover (*56*), perchlorate can be introduced into near-surface rocks by downward percolation and evaporation of brines, possibly associated with ephemeral wetting events extending into the Amazonian (<3 Ga). The co-occurrence of perchlorate and sulfate minerals indicates at least some of the sulfate could have been similarly sourced. The diversity of salt compositions in the analyzed white patches (e.g. their variety of S/Cl and Ca/Mg/Fe ratios) indicates that several different fluids could have been involved, possibly at different times, and possibly repeatedly. The extreme solubility of perchlorate salts indicates they are the youngest alteration materials in these rocks. Salt hydration and dehydration can cause substantial volume expansion (*57*), weakening the rock and contributing to the mechanical erosion and disaggregation of outcrop by aeolian processes across the floor of Jezero crater.

Although there is evidence for rock-dominated aqueous alteration and a diversity of secondary phases, there is no geochemical or mineralogical indication of extensive open-system aqueous alteration in which soluble cations (Ca, Na, K) are entirely removed, resulting in enrichments in aluminous phases (i.e. Al-rich clays) (*58*). The bulk compositions of both the Máaz and Séítah formations are consistent with near-pristine igneous rocks (except in S and Cl, see **Tables S1, S2**); hydrated aluminosilicates are rare or absent; and there is no textural or chemical evidence for extensive plagioclase alteration or olivine/pyroxene dissolution (*59*).

Geologic Models

We propose two scenarios for the history of the Jezero crater floor, given our inability to distinguish whether the Máaz formation consists of lava flows (hereafter Model 1) or an igneous complement to the olivine cumulate of the Séítah formation (Model 2).

During or after the formation of Jezero crater, a thick magma body or melt sheet (*39*) existed within the crater. This could have been emplaced on, or intruded into, a pre-existing crater fill. Differentiation and crystal settling formed the olivine cumulate (*39*) while also producing a less mafic complement (**Fig. 6A**). In Model 1, erosion removed most or all of this material, leaving at least tens of meters of topography on the residual olivine cumulate deposit (Fig. 6B), after which lava flows of the Máaz formation flowed around, and at least partially overtopped, the underlying topography (Fig. 6C). Deformation of unknown origin then tilted the originally flat-lying layers of both formations at least locally by ~10^{o} to the SW (Fig. 6D), as observed along Artuby ridge. In Model 2, both Máaz and Séítah were produced by magmatic differentiation similar to a layered igneous body (Fig. 6E). Deformation of unknown origin then uplifted Séítah relative to Máaz, tilting both (Fig. 6F).

In both models, the Máaz and Séítah formations later experienced further erosion that removed overlying Máaz formation rocks from above the Séítah formation (Fig. 6G). We adopt the interpretation (*21*, *27*) that the crater floor units were then at least partially buried by the delta and associated Jezero lake deposits (Fig. 6H). The late Noachian age (3.6-3.8 Ga (*7*)) of the largest river valley networks feeding Jezero, and the assumed Hesperian age of the exposed delta (*8*), provide a possibly long period of aqueous activity during which lacustrine and igneous processes both occurred, possibly driving hydrothermal interactions. However, we have found no evidence for remnant sedimentary units along Perseverance's traverse through Sol 290; if delta or lake sediments once covered both the Máaz and Séítah formations (Fig. 6H), they appear to have largely eroded away (Fig. 6I), with the exception of delta remnant mounds like Kodiak (*60*).

A variety of concurrent and subsequent processes, including rock-dominated alteration and salt deposition, modified the chemistry and mineralogy of these rocks as they interacted with aqueous solutions. Spatially and chemically distinct materials (carbonate, likely amorphous silicate, Fe-oxides, perchlorate, sulfates, and possibly Fe silicates) could be the product of multiple distinct aqueous events, differing in chemistry and possibly separated in time. Both hydrothermal waters and groundwater could have played a role.

Habitability and Preservation Potential

One proposed definition of a habitable environment is one in which liquid water, available energy, nutrients, and other physicochemical conditions are adequate for supporting known forms of life (*61*). On Earth, reactions of igneous rocks with water produce diverse habitats for microbial life (*62*, *63*). The oxidation and partitioning of iron into secondary phases during alteration processes, such as carbonation and serpentinization, can yield H_2 – a potential energy source – along with methane and other hydrocarbons, which can form raw materials for the synthesis of more complex organic molecules (*62*, *63*). The chemical reduction of nitrate, sulfate, and metal ions, along with hydrocarbon degradation, are thought to power microbial metabolisms in Earth's deep subsurface (*64*). Rocks of the Jezero crater floor appear to share the compositional components of these habitable environments. The soluble salts and vein-filling minerals we observe, such as iron oxides, perchlorate and sulfate salts, could have formed under low temperature, habitable conditions, but could also have formed under non-habitable conditions (*65*–*67*).

The potential for secondary aqueous phases to preserve evidence of life depends on how they formed. On Earth, studies of evaporitic and desert environments demonstrate the presence and preservation of microbial life in association with salts (*65*, *66*, *68*, *69*). Carbonate veins on Earth, produced through serpentinization and carbonation, can preserve biomarkers such as lipids (*70*–*72*) and/or organic structures interpreted as fossilized microbial communities (*71*). By analogy, we propose that the secondary phases in the altered igneous rocks of the Jezero crater floor might have the potential to record biosignatures, if ancient habitable environments existed.

Sample Collection

Laboratories on Earth have measurement capabilities superior to instruments which can be mounted on a Mars rover. An objective of the Mars 2020 mission is therefore to collect samples, in the form of drilled rock cores, for potential transport to Earth by another spacecraft in the 2030s. We attempted core acquisition on three different rock targets: two in the Máaz formation and one in the Séítah formation. The first coring attempt occurred near Guillaumes (**Fig. 1B**), in the low-lying, polygonal pavement of the Roubion member of the Máaz formation. Although the sample collection process appeared to execute as expected, the sample tube was subsequently found to contain no rock or rock fragments. A likely explanation is that this rock disintegrated during drilling, likely due to the rock's aqueous alteration (**Fig. 3A**). The sample tube was sealed and provides a sample of ambient Martian atmosphere instead. A second sample acquisition attempt was performed on the Rochette member on the crest of Artuby ridge near Bellegarde, and a third on the Séítah formation Bastide member near Dourbes; these were both successful (**Fig. 7**).

Aqueously altered igneous rocks have advantages as samples for Earth return. The formations these samples were taken from likely date from the late Noachian to early Hesperian; only a small fraction of Martian meteorites are this old (*73*). Their crystallization ages, along with the pressures and temperatures during igneous rock formation, could potentially be determined with current laboratory equipment. Because both the Máaz and Séítah formations are thought to extend beneath the delta in Jezero (*21*, *27*), igneous crystallization ages would provide upper

bounds on the age of the lake and the fluvial processes which deposited the delta (*60*), a lower bound on the age of the Jezero impact, and an upper bound on the age of the smaller craters on the Máaz formation. The igneous lithologies of the samples might be suitable for paleomagnetic analysis of the ancient Martian magnetic field (*74*).

References and Notes

1. K. A. Farley, K. H. Williford, K. M. Stack, R. Bhartia, A. Chen et al., Mars 2020 Mission overview. *Space Science Reviews*. **216**, 142 (2020).

2. S. C. Werner, The early martian evolution—Constraints from basin formation ages. *Icarus*. **195**, 45–60 (2008).

3. J. F. Mustard, F. Poulet, J. W. Head, N. Mangold, J.-P. Bibring et al., Mineralogy of the Nili Fossae region with OMEGA/Mars Express data: 1. Ancient impact melt in the Isidis Basin and implications for the transition from the Noachian to Hesperian. *Journal of Geophysical Research: Planets*. **112** (2007), doi:10.1029/2006JE002834.

4. B. L. Ehlmann, J. F. Mustard, C. I. Fassett, S. C. Schon, J. W. Head III et al., Clay minerals in delta deposits and organic preservation potential on Mars. *Nature Geoscience*. **1**, 355–358 (2008).

5. J. F. Mustard, B. L. Ehlmann, S. L. Murchie, F. Poulet, N. Mangold et al., Composition, morphology, and stratigraphy of Noachian crust around the Isidis basin. *Journal of Geophysical Research*. **114** (2009), doi:10.1029/2009je003349.

6. N. Mangold, F. Poulet, J. F. Mustard, J.-P. Bibring, B. Gondet et al., Mineralogy of the Nili Fossae region with OMEGA/Mars Express data: 2. Aqueous alteration of the crust. *Journal of Geophysical Research: Planets*. **112** (2007), doi:10.1029/2006JE002835.

7. C. I. Fassett, J. W. Head, Valley network-fed, open-basin lakes on Mars: Distribution and implications for Noachian surface and subsurface hydrology. *Icarus*. **198**, 37–56 (2008).

8. N. Mangold, G. Dromart, V. Ansan, F. Salese, M. G. Kleinhans et al., Fluvial regimes, morphometry, and age of Jezero crater paleolake inlet valleys and their exobiological significance for the 2020 Rover Mission landing site. *Astrobiology*. **20**, 994–1013 (2020).

9. T. A. Goudge, J. F. Mustard, J. W. Head, C. I. Fassett, S. M. Wiseman, Assessing the mineralogy of the watershed and fan deposits of the Jezero crater paleolake system, Mars. *Journal of Geophysical Research: Planets*. **120**, 775–808 (2015).

10. C. I. Fassett, J. W. Head III, Fluvial sedimentary deposits on Mars: Ancient deltas in a crater lake in the Nili Fossae region. *Geophysical Research Letters*. **32**, L14201 (2005).

11. B. L. Ehlmann, J. F. Mustard, S. L. Murchie, F. Poulet, J. L. Bishop et al., Orbital identification of carbonate-bearing rocks on Mars. *Science*. **322**, 1828–1832 (2008).

12. A. J. Brown, C. E. Viviano, T. A. Goudge, Olivine-carbonate mineralogy of the Jezero crater region. *Journal of Geophysical Research: Planets*. **125** (2020), doi:10.1029/2019JE006011.

13. B. L. Ehlmann, J. F. Mustard, G. A. Swayze, R. N. Clark, J. L. Bishop et al., Identification of hydrated silicate minerals on Mars using MRO-CRISM: Geologic context near Nili Fossae and implications for aqueous alteration. *Journal of Geophysical Research: Planets*. **114** (2009), doi:10.1029/2009JE003339.

14. A. Ody, F. Poulet, J.-P. Bibring, D. Loizeau, J. Carter et al., Global investigation of olivine on Mars: Insights into crust and mantle compositions. *Journal of Geophysical Research: Planets*. **118**, 234–262 (2013).

15. T.M. Hoefen, R.N. Clark, J.L. Bandfield, M.D. Smith et al., Discovery of olivine in the Nili Fossae region of Mars. *Science*. **302**, 627–630 (2003).

16. V. E. Hamilton, P. R. Christensen, Evidence for extensive, olivine-rich bedrock on Mars. *Geology*. **33**, 433–436 (2005).

17. L. L. Tornabene, J. E. Moersch, H. Y. McSween Jr., V. E. Hamilton, J. L. Piatek et al., Surface and crater-exposed lithologic units of the Isidis Basin as mapped by coanalysis of THEMIS and TES derived data products. *Journal of Geophysical Research: Planets*. **113** (2008), doi:10.1029/2007JE002988.

18. C. H. Kremer, J. F. Mustard, M. S. Bramble, A widespread olivine-rich ash deposit on Mars. *Geology*. **47**, 677–681 (2019).

19. L. Mandon, C. Quantin-Nataf, P. Thollot, N. Mangold, L. Lozac'H et al., Refining the age, emplacement and alteration scenarios of the olivine-rich unit in the Nili Fossae region, Mars. *Icarus*. **336**, 113436 (2020).

20. A. D. Rogers, N. H. Warner, M. P. Golombek, J. W. Head III, J. C. Cowart, Areally extensive surface bedrock exposures on Mars: Many are clastic rocks, not lavas. *Geophysical Research Letters*. **45**, 1767–1777 (2018).

21. V. Z. Sun, K. M. Stack, "Geologic map of Jezero crater and the Nili Planum region, Mars," *Scientific Investigations Map* (USGS Numbered Series 3464, U.S. Geological Survey, Reston, VA, 2020), doi:10.3133/sim3464.

22. S. C. Schon, J. W. Head, C. I. Fassett, An overfilled lacustrine system and progradational delta in Jezero crater, Mars: Implications for Noachian climate. *Planetary and Space Science*. **67**, 28–45 (2012).

23. K. M. Stack, N. R. Williams, F. Calef, V. Z. Sun, K. H. Williford et al., Photogeologic map of the Perseverance rover field site in Jezero crater constructed by the Mars 2020 Science Team. *Space Sci Rev*. **216**, 127 (2020).

24. S. Shahrzad, K. M. Kinch, T. A. Goudge, C. I. Fassett, D. H. Needham et al., Crater statistics on the dark-toned, mafic floor unit in Jezero crater, Mars. *Geophysical Research Letters*. **46**, 2408–2416 (2019).

25. J. D. Tarnas, K. M. Stack, M. Parente, A. H. D. Koeppel, J. F. Mustard et al., Characteristics, origins, and biosignature preservation potential of carbonate-bearing rocks within and outside of Jezero crater. *Journal of Geophysical Research: Planets*. **126** (2021), doi:10.1029/2021JE006898.

26. T. A. Goudge, K. L. Aureli, J. W. Head, C. I. Fassett, J. F. Mustard, Classification and analysis of candidate impact crater-hosted closed-basin lakes on Mars. *Icarus*. **260**, 346–367 (2015).

27. S. Holm-Alwmark, K. M. Kinch, M. D. Hansen, S. Shahrzad, K. Svennevig et al., Stratigraphic relationships in Jezero crater, Mars: Constraints on the timing of fluvial-lacustrine activity from orbital observations. *Journal of Geophysical Research: Planets*. **126** (2021), doi:10.1029/2021JE006840.

28. A. Nelessen, C. Sackier, I. Clark, P. Brugarolas, G. Villar et al., M. Lefland, "Mars 2020 Entry, Descent, and Landing System overview" in *2019 IEEE Aerospace Conference* (2019), pp. 1–20.

29. S.-E. Hamran, D. A. Paige, H. E. F. Amundsen, T. Berger, S. Brovoll et al., Radar Imager for Mars' Subsurface Experiment—RIMFAX. *Space Sci Rev*. **216**, 128 (2020).

30. J. F. Bell, J. N. Maki, G. L. Mehall, M. A. Ravine, M. A. Caplinger et al., The Mars 2020 Perseverance rover Mast Camera Zoom (Mastcam-Z) multispectral, stereoscopic imaging investigation. *Space Sci Rev*. **217**, 24 (2021).

31. R. Bhartia, L. W. Beegle, L. DeFlores, W. Abbey, J. Razzell Hollis et al., Perseverance's Scanning Habitable Environments with Raman and Luminescence for Organics and Chemicals (SHERLOC) Investigation. *Space Sci Rev*. **217**, 58 (2021).

32. R. C. Wiens, S. Maurice, S. H. Robinson, A. E. Nelson, P. Cais et al., The SuperCam Instrument Suite on the NASA Mars 2020 Rover: Body unit and combined system tests. *Space Sci Rev*. **217**, 4 (2020).

33. A. C. Allwood, L. A. Wade, M. C. Foote, W. T. Elam, J. A. Hurowitz et al., PIXL: Planetary Instrument for X-Ray Lithochemistry. *Space Sci Rev*. **216**, 134 (2020).

34. R. C. Moeller, L. Jandura, K. Rosette, M. Robinson, J. Samuels et al., The Sampling and Caching Subsystem (SCS) for the scientific exploration of Jezero crater by the Mars 2020 Perseverance rover. *Space Sci Rev*. **217**, 5 (2020).

35. B. H. N. Horgan, R. B. Anderson, G. Dromart, E. S. Amador, M. S. Rice, The mineral diversity of Jezero crater: Evidence for possible lacustrine carbonates on Mars. *Icarus*. **339**, 113526 (2020).

36. J. L. Bishop, J. F. Bell III, J. E. Moersch, Eds., *Remote Compositional Analysis: Techniques for Understanding Spectroscopy, Mineralogy, and Geochemistry of Planetary Surfaces* (Cambridge University Press, Cambridge, 2019).

37. J. Filiberto, D. Baratoux, D. Beaty, D. Breuer, B. J. Farcy et al., A review of volatiles in the Martian interior. *Meteoritics & Planetary Science*. **51**, 1935–1958 (2016).

38. See supplementary materials.

39. Y. Liu, M. M. Tice, M. E. Schmidt, A. H. Treiman, T. V. Kizovski et al., An olivine cumulate outcrop on the floor of Jezero crater, Mars, *Science*, in press.

40. L.R. Wager and G.M. Brown, *Layered Igneous Rocks* (W H Freeman & Co, 1967).

41. O. Namur, B. Abily, A. Boudreau, F. Blanchette, J. Bush et al., Igneous Layering in Basaltic Magma Chambers in Layered Intrusions, B. Charlier, O. Namur, R. Latypov, C. Tegner, Eds. (Springer Dordrecht, 2015), *Springer Geology*, pp. 75–152.

42. H. Hiesinger, J. W. Head III, The Syrtis Major volcanic province, Mars: Synthesis from Mars Global Surveyor data. *Journal of Geophysical Research: Planets*. **109** (2004), doi:10.1029/2003JE002143.

43. L. M. Jozwiak, J. W. Head, L. Wilson, Lunar floor-fractured craters as magmatic intrusions: Geometry, modes of emplacement, associated tectonic and volcanic features, and implications for gravity anomalies. *Icarus*. **248**, 424–447 (2015).

44. C. S. Edwards, J. L. Bandfield, P. R. Christensen, A. D. Rogers, The formation of infilled craters on Mars: Evidence for widespread impact induced decompression of the early martian mantle? *Icarus*. **228**, 149–166 (2014).

45. B. L. Ehlmann, J. F. Mustard, An in situ record of major environmental transitions on early Mars at Northeast Syrtis Major. *Geophysical Research Letters*. **39** (2012).

46. M. S. Bramble, J. F. Mustard, M. R. Salvatore, The geological history of Northeast Syrtis Major, Mars. *Icarus*. **293**, 66–93 (2017).

47. E. El-Hinnawi, S. D. Abayazeed, A. S. Khalil, Spheroidal weathering of basalt from Gebel Qatrani, Fayum Depression, Egypt. *Bulletin of the National Research Centre*. **45**, 1 (2021).

48. P. B. Kelemen, J. Matter, E. E. Streit, J. F. Rudge, W. B. Curry et al., Rates and mechanisms of mineral carbonation in peridotite: Natural processes and recipes for enhanced, in situ CO_2 capture and storage. *Annu. Rev. Earth Planet. Sci.* **39**, 545–576 (2011).

49. F. Wang, D. Dreisinger, M. Jarvis, T. Hitchins, Kinetics and mechanism of mineral carbonation of olivine for CO_2 sequestration. *Minerals Engineering*. **131**, 185–197 (2019).

50. F. Dufaud, I. Martinez, S. Shilobreeva, Experimental study of Mg-rich silicates: carbonation at 400 and 500 C and 1 kbar. *Chemical Geology*. **265**, 79–87 (2009).

51. S. He, J. W. Morse, The carbonic acid system and calcite solubility in aqueous Na-K-Ca-Mg-Cl-SO4 solutions from 0 to 90°C. *Geochimica et Cosmochimica Acta*. **57**, 3533–3554 (1993).

52. L. Chai, A. Navrotsky, Synthesis, characterization, and enthalpy of mixing of the (Fe,Mg)CO3 solid solution. *Geochimica et Cosmochimica Acta*. **60**, 4377–4383 (1996).

53. B. M. Tutolo, B. W. Evans, S. M. Kuehner, Serpentine–Hisingerite solid solution in Altered ferroan peridotite and olivine gabbro. *Minerals*. **9**, 47 (2019).

54. K. Bladh, The formation of goethite, jarosite, and alunite during the weathering of sulfide-bearing felsic rocks. *Economic Geology*. **77**, 176–184 (1982).

55. P. B. Kelemen, G. Hirth, Reaction-driven cracking during retrograde metamorphism: Olivine hydration and carbonation. *Earth Planet. Sci. Lett.* **345**, 81–89 (2012).

56. P. E. Martin, K. A. Farley, P. Douglas Archer Jr, J. V. Hogancamp, K. L. Siebach et al., Reevaluation of perchlorate in Gale Crater rocks suggests geologically recent perchlorate addition. *Journal of Geophysical Research: Planets*. **125** (2020), doi:10.1029/2019JE006156.

57. A. S. Goudie, H. A. Viles, *Salt Weathering Hazard* (Wiley, 1997).

58. H. W. Nesbitt, R. E. Wilson, Recent chemical weathering of basalts. *American Journal of Science*. **292**, 740–777 (1992).

59. M. A. Velbel, Aqueous Alteration in Martian Meteorites: Comparing Mineral Relations in Igneous-Rock Weathering of Martian Meteorites and in the Sedimentary Cycle of Mars, in *Sedimentary Geology of Mars*, J. P. Grotzinger, R. E. Milliken, Eds. (2012).

60. N. Mangold, S. Gupta, O. Gasnault, G. Dromart, J. D. Tarnas et al., Perseverance rover reveals an ancient delta-lake system and flood deposits at Jezero crater, Mars. *Science* **374**, 711-717 (2021), doi:10.1126/science.abl4051.

61. C. S. Cockell, T. Bush, C. Bryce, S. Direito, M. Fox-Powel et al., Habitability: A review. *Astrobiology*. **16**, 89–117 (2016).

62. T. O. Stevens, J. P. McKinley, Lithoautotrophic microbial ecosystems in deep basalt aquifers. *Science*. **270**, 450–455 (1995).

63. K. H. Nealson, F. Inagaki, K. Takai, Hydrogen-driven subsurface lithoautotrophic microbial ecosystems (SLiMEs): do they exist and why should we care? *Trends in Microbiology*. **13**, 405–410 (2005).

64. O. U. Mason, T. Nakagawa, M. Rosner, J. D. V. Nostrand, J. Zhou et al., First investigation of the microbiology of the deepest layer of ocean crust. *PLOS ONE*. **5**, e15399 (2010).

65. N. Stivaletta, R. Barbieri, D. Billi, Microbial colonization of the salt deposits in the driest place of the Atacama Desert (Chile). *Orig Life Evol Biosph*. **42**, 187–200 (2012).

66. K. C. Benison, How to search for life in Martian chemical sediments and their fluid and solid inclusions using petrographic and spectroscopic methods. *Frontiers in Environmental Science*. **7**, 108 (2019).

67. S. McMahon, T. Bosak, J. P. Grotzinger, R. E. Milliken, R. E. Summons et al., A field guide to finding fossils on Mars. *Journal of Geophysical Research: Planets*. **123**, 1012–1040 (2018).

68. M. R. Mormile, M. A. Biesen, M. C. Gutierrez, A. Ventosa, J. B. Pavlovich et al., Isolation of Halobacterium salinarum retrieved directly from halite brine inclusions. *Environ Microbiol*. **5**, 1094–1102 (2003).

69. B. A. Schubert, T. K. Lowenstein, M. N. Timofeeff, M. A. Parker, Halophilic Archaea cultured from ancient halite, Death Valley, California. *Environ Microbiol*. **12**, 440–454 (2010).

70. S. A. Newman, S. A. Lincoln, S. O'Reilly, X. Liu, E. L. Shock et al., Lipid biomarker record of the serpentinite-hosted ecosystem of the Samail Ophiolite, Oman and implications for the search for biosignatures on Mars. *Astrobiology*. **20**, 830–845 (2020).

71. F. Klein, S. E. Humphris, W. Guo, F. Schubotz, E. M. Schwarzenbach et al., Fluid mixing and the deep biosphere of a fossil Lost City-type hydrothermal system at the Iberia Margin. *Proceedings of the National Academy of Sciences*. **112**, 12036–12041 (2015).

72. A. S. Templeton, E. T. Ellison, C. Glombitza, Y. Morono, K. R. Rempfert et al., Accessing the subsurface biosphere within rocks undergoing active low-temperature serpentinization in the Samail Ophiolite (Oman Drilling Project). *Journal of Geophysical Research: Biogeosciences*. **126** (2021), doi:10.1029/2021JG006315.

73. A. Udry, G. H. Howarth, C. D. K. Herd, J. M. D. Day, T. J. Lapen et al., What Martian meteorites reveal about the interior and surface of Mars. *Journal of Geophysical Research: Planets*. **125** (2020), doi:10.1029/2020JE006523.

74. A. Mittelholz, A. Morschhauser, C. L. Johnson, B. Langlais, R. J. Lillis et al., The Mars 2020 candidate landing sites: A magnetic field perspective. *Earth and Space Science*. **5**, 410–424 (2018).

75. A.C. Allwood and J.A. Hurowitz, PIXL Raw and Processed Data Bundle (2021), *Planetary Data System; doi:10.17189/1522645*.

76. S.E. Hamran and D.P. Paige, Mars 2020 Perseverance Rover RIMFAX Raw and Calibrated Data Products Data Bundle (2021), *Planetary Data System; doi:10.17189/1522644*.

77. L. Beegle, Mars 2020 SHERLOC Data Bundle (2021), *Planetary Data System, doi:10.17189/1522643.*

78. S.A. Maurice, and R.C. Wiens, Mars 2020 SuperCam Data Bundle (2021), *Planetary Data System, doi:10.17189/1522646*.

79. J.F. Bell and J.N. Maki, Mast Camera Zoom Data Bundle, from Operations Team, calibrated products (2021), *Planetary Data System, doi:10.17189/BS6B-4782*.

80. J.N. Maki, Mars 2020 Engineering Camera Data Bundle (2021), *Planetary Data System, doi:10.17189/1522847*.

81. J. N. Maki, D. Gruel, C. McKinney, M. A. Ravine, M. Morales et al., The Mars 2020 Engineering Cameras and microphone on the Perseverance rover: A next-generation imaging system for Mars exploration. *Space Science Reviews*. **216**, 137 (2020).

82. A. Wang, J. J. Freeman, B. L. Jolliff, I.-M. Chou, Sulfates on Mars: A systematic Raman spectroscopic study of hydration states of magnesium sulfates. *Geochimica et Cosmochimica Acta*. **70**, 6118–6135 (2006).

83. F. M. McCubbin, N. J. Tosca, A. Smirnov, H. Nekvasil, A. Steele, et al., Hydrothermal jarosite and hematite in a pyroxene-hosted melt inclusion in martian meteorite Miller Range (MIL) 03346: Implications for magmatic-hydrothermal fluids on Mars. *Geochimica et Cosmochimica Acta*. **73**, 4907–4917 (2009).

84. W. J. Abbey, R. Bhartia, L. W. Beegle, L. DeFlores, V. Paez et al., Deep UV Raman spectroscopy for planetary exploration: The search for in situ organics. *Icarus*. **290**, 201–214 (2017).

85. J. Razzell Hollis, W. Abbey, L. W. Beegle, R. Bhartia, B. L. Ehlmann et al., A deep-ultraviolet Raman and Fluorescence spectral library of 62 minerals for the SHERLOC instrument onboard Mars 2020. *Planetary and Space Science*. **209**, 105356 (2021).

86. S. Maurice, R. C. Wiens, P. Bernardi, P. Caïs, S. Robinson et al., The SuperCam instrument suite on the Mars 2020 rover: Science objectives and mast-unit description. *Space Sci Rev*. **217**, 47 (2021).

87. C. Royer, F. Poulet, J.-M. Reess, C. Pilorget, V. Hamm et al., Pre-launch radiometric calibration of the infrared spectrometer onboard SuperCam for the Mars2020 rover. *Review of Scientific Instruments*. **91**, 063105 (2020).

88. K. M. Stack, C. S. Edwards, J. P. Grotzinger, S. Gupta, D. Y. Sumner et al., Comparing orbiter and rover image-based mapping of an ancient sedimentary environment, Aeolis Palus, Gale crater, Mars. *Icarus*. **280**, 3–21 (2016).

89. Mars 2020 Terrain Relative Navigation HiRISE Orthorectified Image Mosaic, doi.org/10.5066/P9QJDP48.

90. Mars 2020 Terrain Relative Navigation HiRISE DTM Mosaic, doi.org/10.5066/P9REJ9JN.

91. R. F. Kokaly, R. N. Clark, G. A. Swayze, K. E. Livo, T. M. Hoefen et al., USGS Spectral Library Version 7, *Data Series* (Report 1035, Reston, VA, 2017), p. 68.

92. R. B. Anderson, O. Forni, A. Cousin, R. C. Wiens, S. M. Clegg et al., Post-landing major element quantification using SuperCam laser induced breakdown spectroscopy. *Spectrochimica Acta Part B: Atomic Spectroscopy*. **188**, 106347 (2022).

Acknowledgments: The authors thank three anonymous reviewers for helpful suggestions that improved this manuscript. This work was enabled by a large and dedicated team of engineers that designed, built, and operate the Mars 2020 spacecraft. We thank John Arballo for drafting many of the figures in this paper.

Funding: This effort was carried out in part at the Jet Propulsion Laboratory, California Institute of Technology under a contract with the National Aeronautics and Space Administration (80NM0018D0004). KAF, KMS, JDT, VZS, YL, JNM, ACA, YG, PAW, ELC, SMM, RCM, SFS, NS, and KU were supported by NASA grant 80NM0018D0004 through JPL. DTF was supported by Australian Research Council grant DE210100205. EFG was supported by Canadian Space Agency grant 21EXPCOI1. EAC was supported by Canadian Space Agency grant 19PACOI0 and Natural Sciences and Engineering Research Council of Canada grant RGPIN-2021-02995. CDKH, TVK, and MES were supported by Canadian Space Agency M2020 Participating Scientist grants. MM was supported by E.U.'s Horizon 2020 research and innovation programme under the Marie Skłodowska Curie grant agreement No 801199. GP was supported by ESA PRODEX Experiment Arrangement PEA 4000117520. VD was supported by Fonds pour la Recherche Scientifique. AJW, SJV, DLS, JIS, LEM, TB, and EMH were supported by NASA Mars 2020 Participating Scientist grants. RCW was supported by NASA Mars 2020 Contracts NNH15AZ24I and NNH13ZDA018O for Supercam and a LANL internal LDRD grant. SKS was supported by JPL subcontract no. 1654163. AG was supported by the Royal Society Leverhulme Trust Senior Research Fellowship (SRF\R1\21000106) and the UK Space Agency AURORA programme. MPZ was supported by the Spanish Ministry of Science and Innovation under grant PID2019-104205GB-C21. SS was supported by the Swedish National Space Agency under contracts 137/19 and 2021-00092. KBK was supported by the Carlsberg Foundation, grant CF19-0023. SHE was supported by the Research Council of Norway under grants 301238 and 309835. The work of OB, AC, OF, LM, NM, CQN, PB, KB, BC, EC, ED, TF, JL, SLM, SM, PYM, PP, CP, PCP, CR, and VS on Mars 2020 was supported by CNES. KHL was supported by a UK Space Agency Aurora Research Fellowship. MAS was supported by UK Space Agency grants ST/V002732/1 and ST/V006134/1.

Author Contributions:
Conceptualization: KAF, RW, JAH, JIS, KMS, DLS
Methodology: KAF, KMS, ELS, JNM, JDT, AGH, PYM, GP, DAKP, CDT, KU, RCW, TVK, MES, JAH, JFB, BHNH, YL, RB, SEH, LM, CQN, CCM
Investigation: KAF, KMS, BHNH, JDT, JIS, VZS, ELS, KRM, SMM, RCW, AHT, LEM, OB, TVK, NJT, JAH, KHW, LSC, JFB, YL, JNM, MES, RB, TB, AJB, BCC, AC, OF, TSJB, YG, SG, SEH, CDKH, KHL, JRJ, LCK, PBK, KMK, LM, NM, CQN, MSR, PSR, SS, SS, AS, MW, BPW, AJW, BVW, PAW, TAAM, PB, KB, SB, ASB, ELC, BC, EC, EAC, BC, VD, ED, AGF, DTF, SZF, TF, JF, BJG, EFG, EMH, AGH, JH, JLJ, EMK, JL, SLM, JMM, SM, MM, PYM, SMM, CCM, RM, JIN, AMO, GP, DAP, PP, CP, PCP, CR, VS, MDS, MAS, SKS, SFS, MSC, CDT, KU, SJVB, MPZM, JWR, ADC, AGY, ACA, RS
Visualization: KAF, KMS, DLS, ELS, JNM, LWB, RB, JH, SS, LC, BHNH, JDT, JFB, SEH, PSR
Funding acquisition: KAF, KMS, KHW, MDS, AB, NS, ACA, SEH, RCW, LWB, JFB
Project administration: KAF, KMS, KHW, RCW, JAH, LWB, JFB, JNM, RB, TB, AJB, SEH, CDKH, SM, DAP, MDS, NS, SMM, ACA

Supervision: KAF, KMS, KHW, DLS, BHNH, JDT, JIS, VZS, LEM, YG, SG, KHL, JRJ, LCK, NM, MSR, BPW, AJW, PAW, ELC, BAC, DTF, JF,
Writing: KAF, KMS, DLS, BHNH, JDT, VZS, JIS, ES, KRM, JH, RW, KW, KRM, NJT, JAH, BLE, LEM, PMV SMM
Writing – review & editing: KAF, KMS, DLS, BE, SG

Competing interests: The authors declare that they have no competing interests.

Data and materials availability: All data used in this paper are archived in the NASA Planetary Data System ***(75–80)***. Details of which files were used are provided in the supplementary material.

Supplementary Materials

Materials and Methods

Supplementary Text

Figs. S1 to S9

Table S1 to S2

References (82-92)

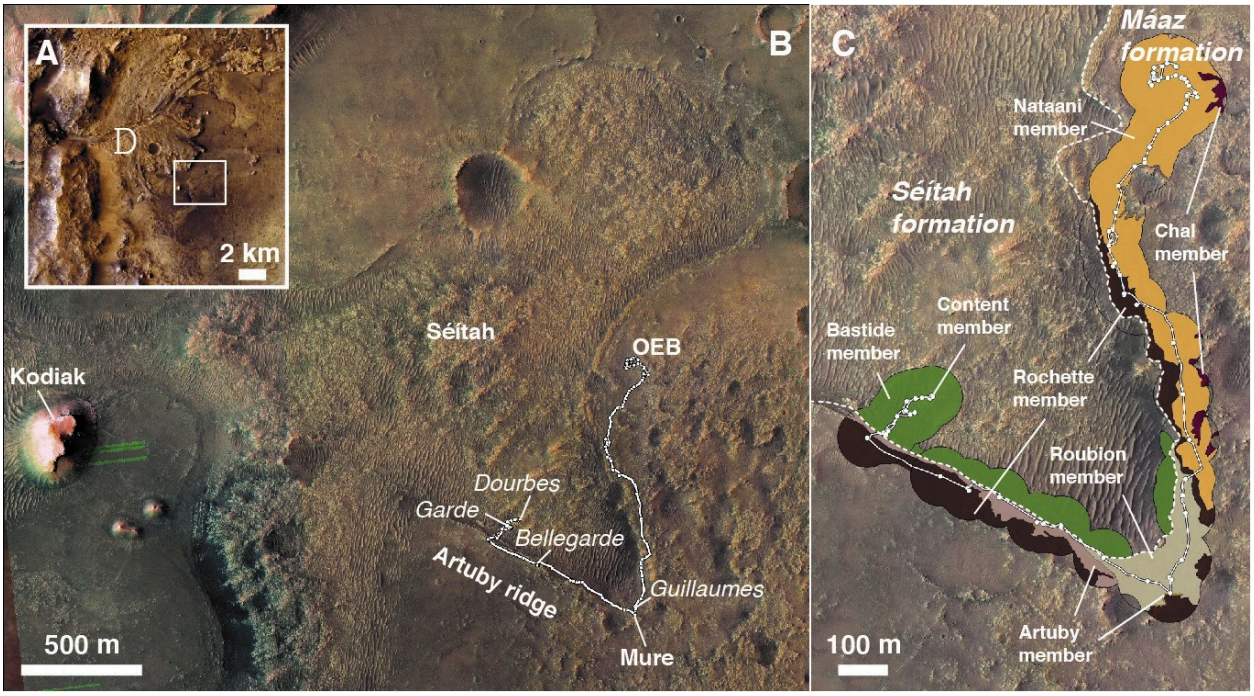

Fig. 1. Orbital images of the Jezero crater floor study area. (A) Mars Reconnaissance Orbiter (MRO) Context Camera **(**CTX) base map overlain by Mars Express High Resolution Stereo Camera color images. The study area is on the western side of Jezero crater, a few km east of the delta (indicated by letter D). (B) High Resolution Imaging Science Experiment (HiRISE) color image of the rover's landing site at Octavia E. Butler landing (OEB), and its traverse up to sol 290 (white path; each circle on the path is the end of a sol). The locations of the four abrasion patches are labelled in italics, and four landforms, Séítah, Artuby ridge, the Kodiak delta remnant (*60*) and the Mure outcrop are labelled in white. Séítah is characterized by abundant aeolian bedforms and northeast-southwest striking ridges. The region east and southeast of OEB is part of the Máaz formation, which exhibits high but variable impact crater density. (C) Enlarged part of panel B, overlain with a geologic map showing our interpreted distribution of the Séítah and Maaz formations. Colors indicate mapped distribution of formation members (labelled) and the formation contact is indicated by the dashed white line. The Content member is only visible at the point indicated. Figure S5 shows stratigraphic columns associated with this map.

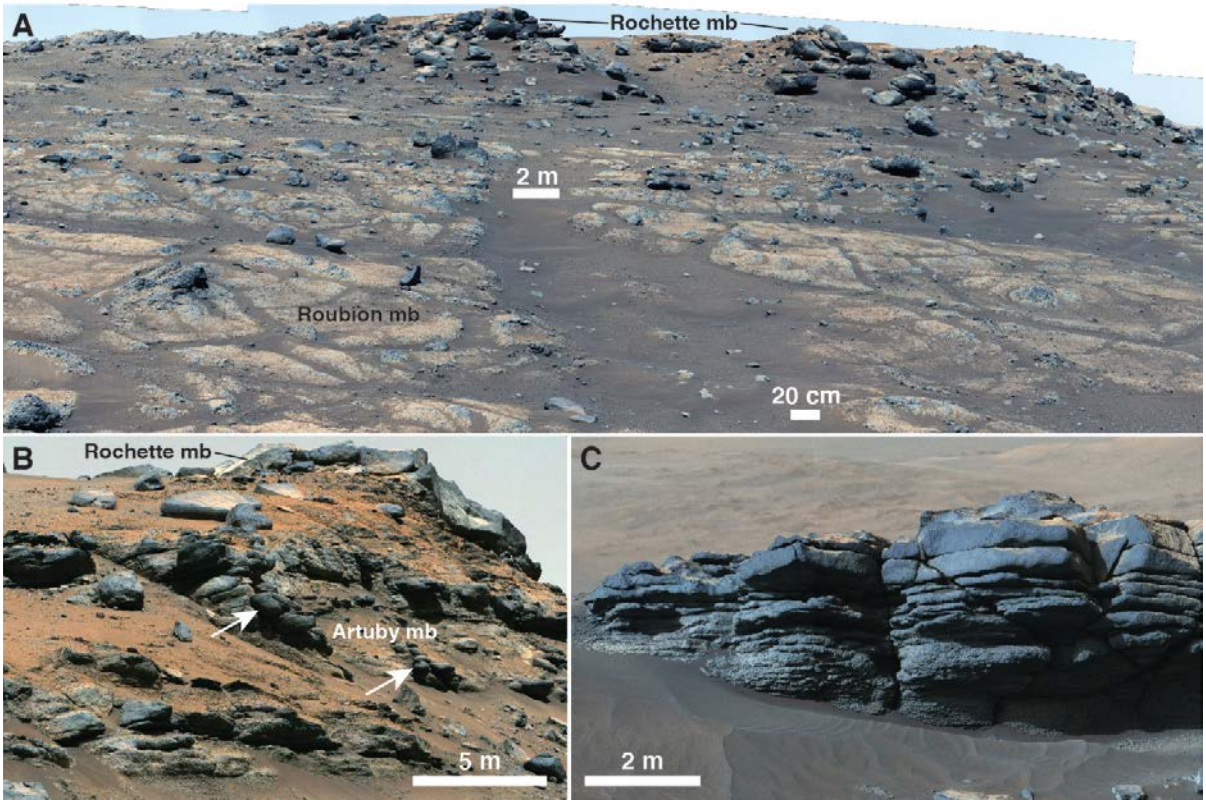

Fig. 2. Rover images of igneous rocks in the Máaz formation. All panels show enhanced-color Mastcam-Z images. (**A**) Image acquired on sol 138, showing low-relief, friable outcrops of the Roubion member (mb; foreground) overlain upslope by resistant caprocks of the Rochette member. (B) Image acquired on sol 175 showing layered rocks of the Artuby member, which are capped by the resistant rocks of the Rochette member. Artuby member layers range in thickness from less than 1 cm up to several decimeters and are generally planar. White arrows point to rounded outcrop protrusions. (C) Image acquired on sol 282, showing layered caprock of the Rochette member. Layers range in thickness from several centimeters to several decimeters and show an apparent thickening upward trend. Layers are planar and dip ~10º to the south (into the page). Source images (*38*) in this figure and shown below have been white-balanced, contrast-stretched, and gamma-corrected to improve viewability and contrast.

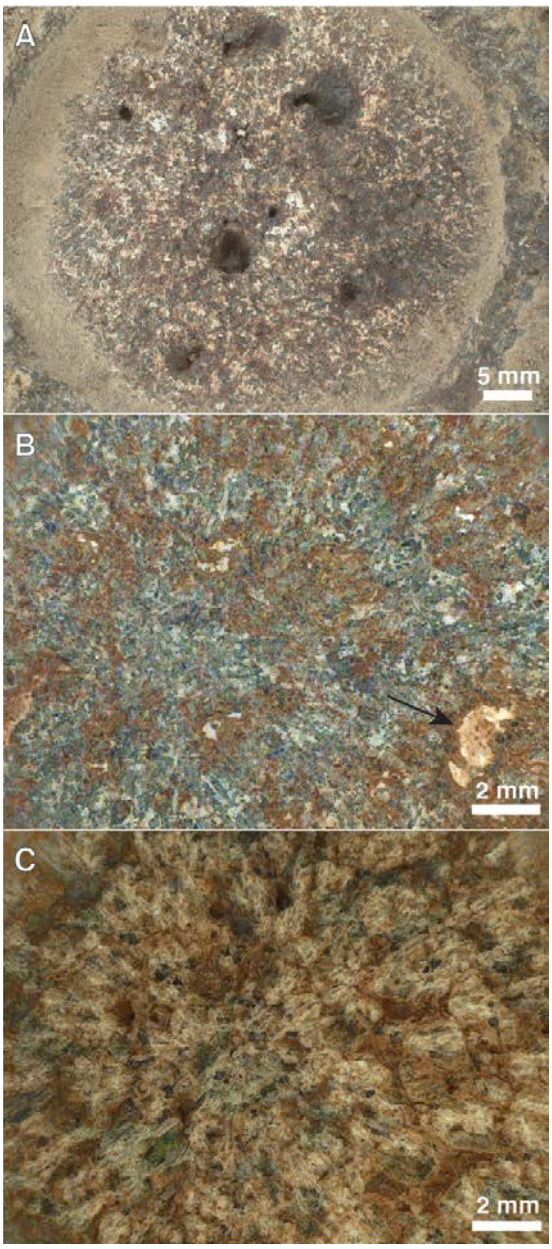

Fig. 3. Microscope images of abrasion patches. (**A**) WATSON image of the Guillaumes abrasion patch, on the Roubion member of the Máaz formation, acquired on sol 160. Millimeter-sized light and dark toned minerals interlock, bright white and brown-to-black material coats surfaces and fills interstices, and several holes and crevices penetrate into the rock. (B) Combined SHERLOC and WATSON images of the Bellegarde abrasion patch, on the Rochette member of the Máaz formation, acquired on sol 186. 0.5-1 mm light and dark minerals are present, coated or stained with brown material, but less extensively than in Guillaumes. The black arrow points to bright white material, also stained brown, likely filling a void in the rock. (C) Combined SHERLOC and WATSON images of the Dourbes abrasion patch, on the Bastide member of the Séítah formation, acquired on sol 257. 2-3 mm sized light-toned grains are surrounded by a dark green mineral. Brown material occurs on most grain boundaries and sometimes coating the lighter-toned grains.

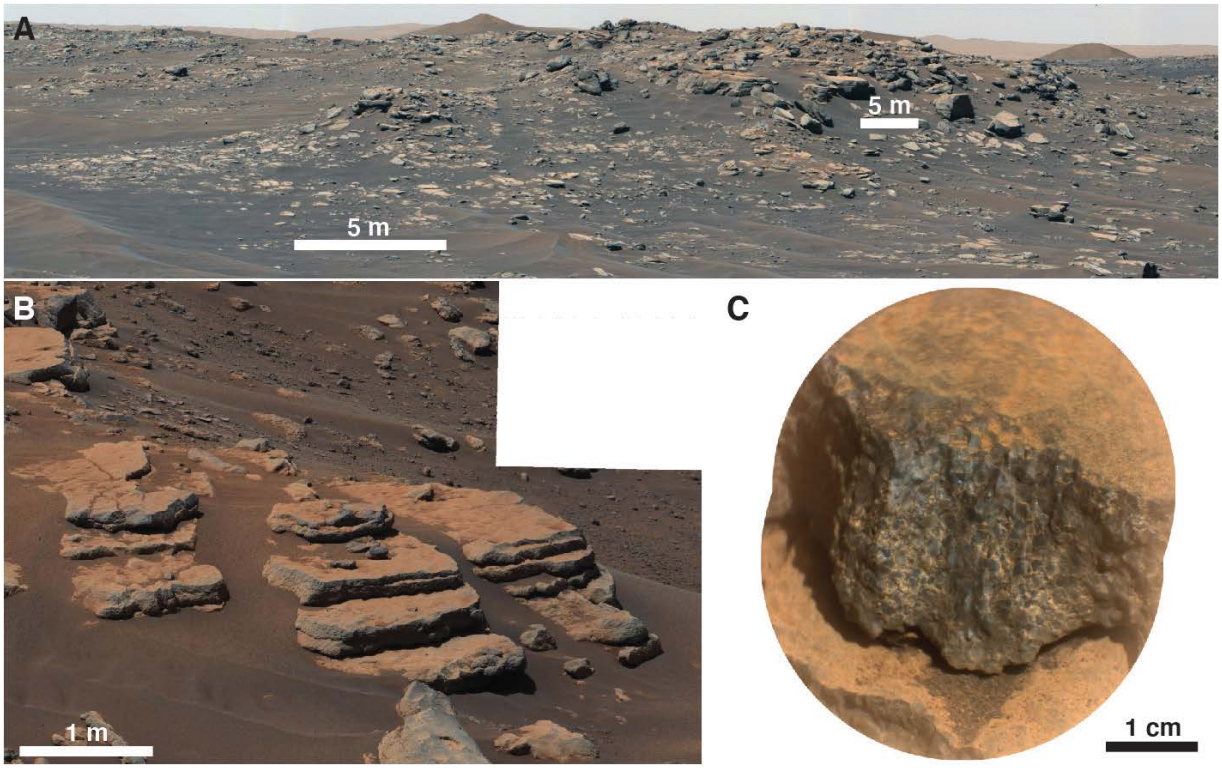

Fig. 4. Layered and coarse-grained appearance of the Bastide member of the Séítah formation. (A) Enhanced color Mastcam-Z mosaic of Bastide, acquired on sol 201, showing bedrock exposures eroding into tabular boulders, which occur mostly on ridges. Bastide member bedrock varies from thinly layered to structureless, and individual layers cannot typically be traced more than a few meters. The platy and tabular appearance of the Séítah formation contrasts strongly with the more-rounded boulders of Máaz (Fig. 2A). (B) Enhanced color Mastcam-Z mosaic acquired on sol 204, of the Bastide outcrop where the Garde abrasion was performed. Centimeter-scale layering is accentuated by differential erosion. (C) Supercam mosaic of the Cine abrasion target on the Bastide formation, acquired on sol 206. On surfaces with little dust or coating, the Bastide member rocks reveal abundant 2-3 mm angular to rounded grey-green grains, separated by lighter toned material.

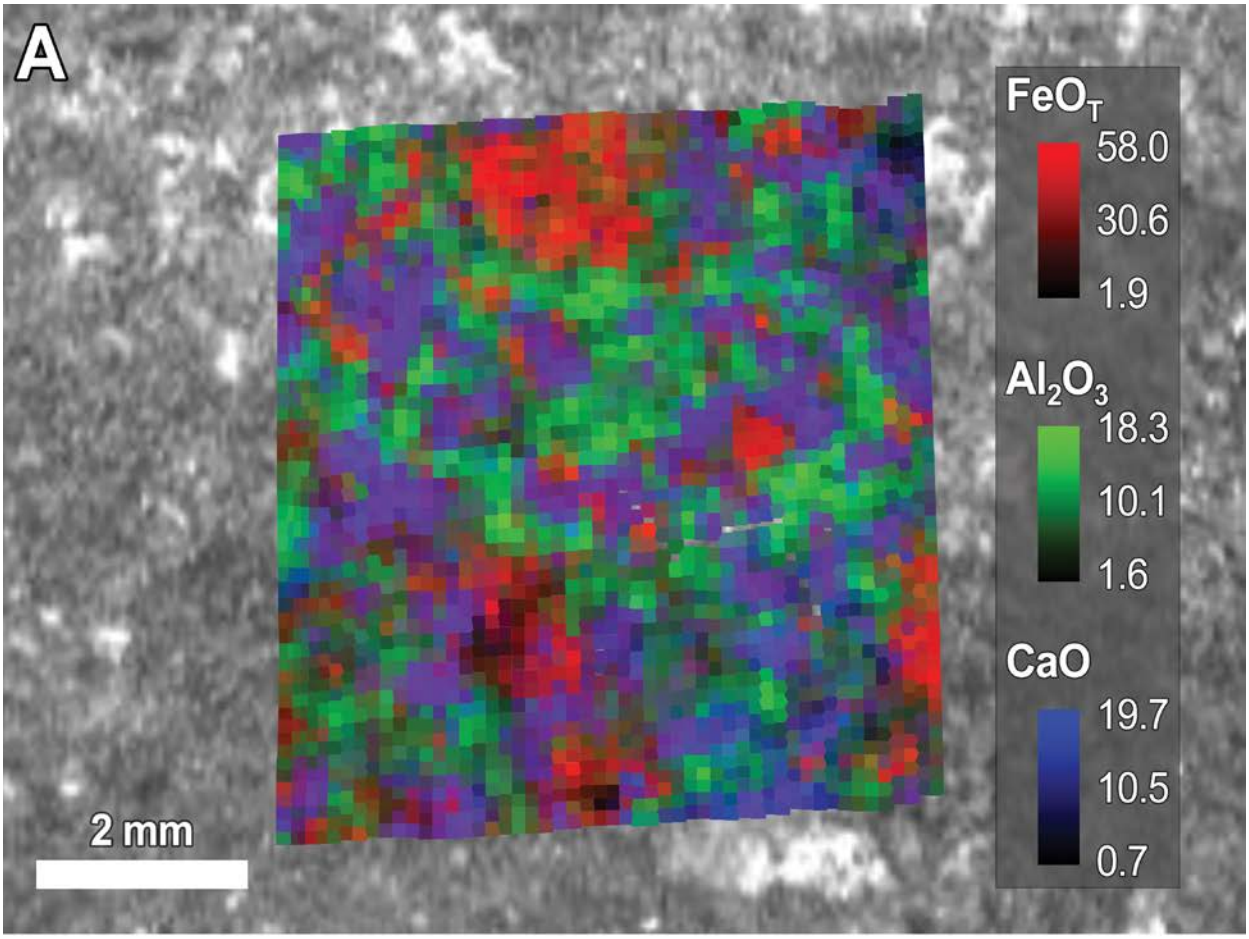
A
FeO_T
58.0
30.6
1.9
Al_2O_3
18.3
10.1
1.6
CaO
19.7
10.5
0.7
2 mm

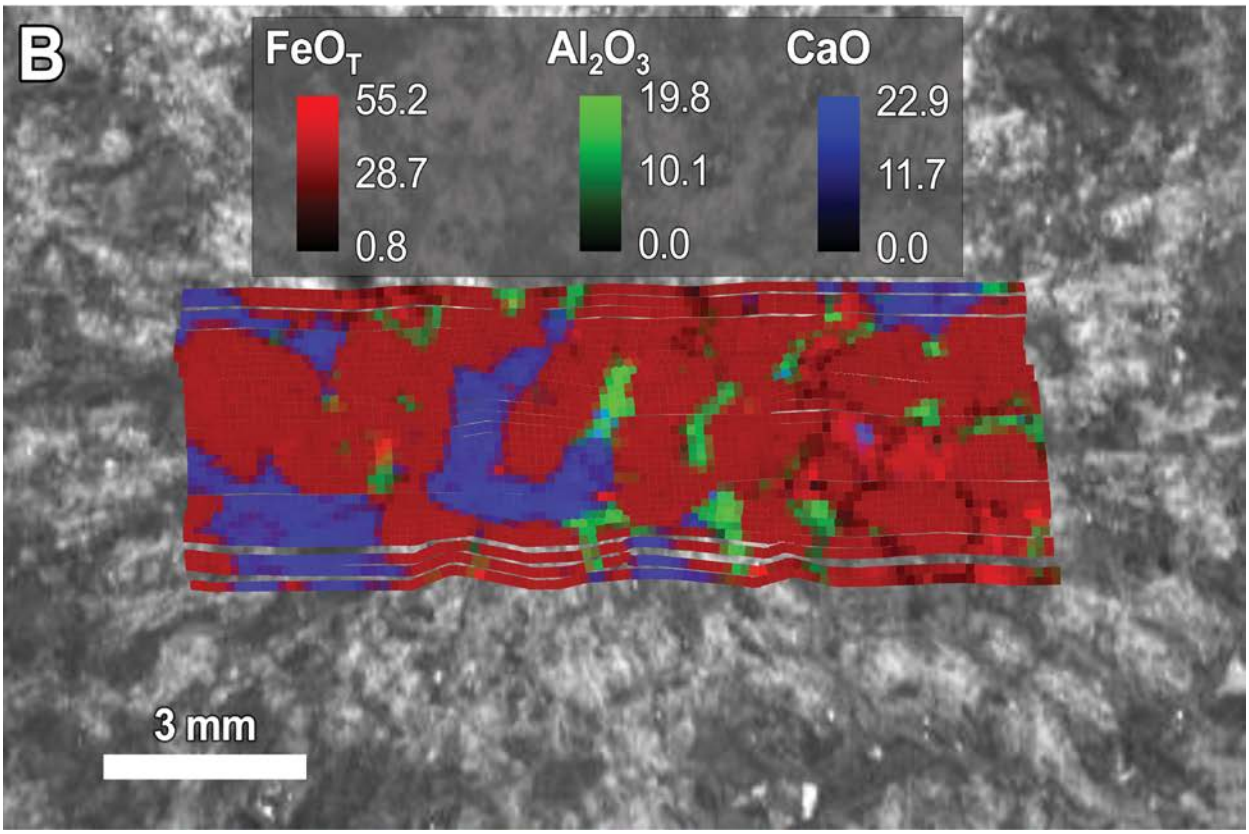
B
FeO_T
55.2
28.7
0.8
Al_2O_3
19.8
10.1
0.0
CaO
22.9
11.7
0.0
3 mm

Fig. 5. Compositional maps of Guillaumes and Dourbes abrasion patches. PIXL X-ray fluorescence maps indicating composition are shown in color (as indicated in the legends), with concentrations in wt %. These are overlain on greyscale visual images indicating rock texture. **(A)** Guillaumes is dominated by grains with compositions consistent with plagioclase (high Al, corresponding to the light grains visible in Fig. 3A) and augite (high Ca and Fe, corresponding to dark grains in Fig. 3A). Fe-rich material appears brown in Fig. 3A; it could be primary or secondary Fe silicates, iron oxides, both, or FeTi oxides and sulfates, as they are indistinguishable in this representation. (B) Dourbes is dominated by euhedral/subhedral olivine of ~Fo_{55} composition (Fe-rich, corresponding to light-toned grains in Fig. 3C). Augite (high Ca, corresponding to dark green grains in Fig. 3C) engulfs olivine, which a companion paper interprets as poikilitic igneous texture indicating an igneous olivine cumulate rock (*39*). High Al regions indicate plagioclase. Sulfates and carbonates appear as small areas with the highest Fe. Figure S9 provides plots of concentrations of Ca, Fe, and Al in blue-scale to assist in interpretation of colors on this figure. FeO_T is total iron as Fe^{+2}.

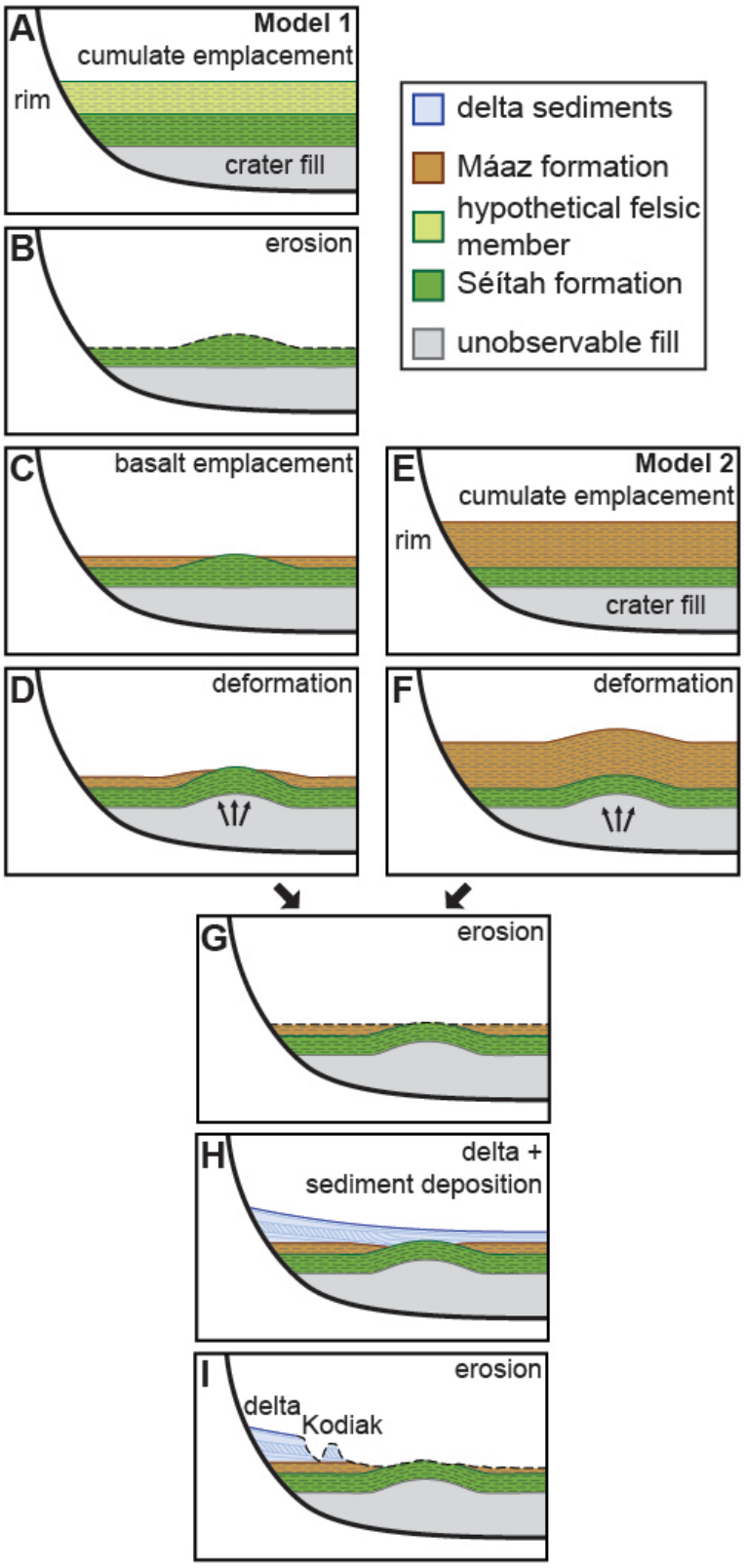
A
Model 1
cumulate emplacement
rim
crater fill
B
erosion
C
basalt emplacement
D
deformation
E
Model 2
cumulate emplacement
rim
crater fill
F
deformation
G
erosion
H
delta +
sediment deposition
I
erosion
delta
Kodiak
delta sediments
Máaz formation
hypothetical felsic member
Séitah formation
unobservable fill

Fig. 6. Two possible models for the evolution of Jezero crater floor. Proposed geological formations are indicated by the legend. (**A**) In Model 1, the differentiated magma body experienced (**B**) erosion that removed a less mafic complement, producing topography on the Séítah formation olivine cumulate. (**C**) Máaz formation lavas surrounded this underlying topography. (**D**) Deformation of unknown cause tilts both Séítah and Máaz, as observed along Artuby ridge. (**E**) In Model 2, flat-lying layers of a differentiated magma body (**F**) deformed in a way that tilted both the olivine cumulate (Séítah formation) and the less mafic complement (Máaz formation), and also uplifted Séítah relative to Máaz. In (**G**) and (**H**), common to both models, erosion occurred and delta and lacustrine sediments were deposited in the lake that filled Jezero. (**I**) Later, they were eroded to their current surface exposure distribution. Aqueous alteration processes could have occurred during any of these steps.

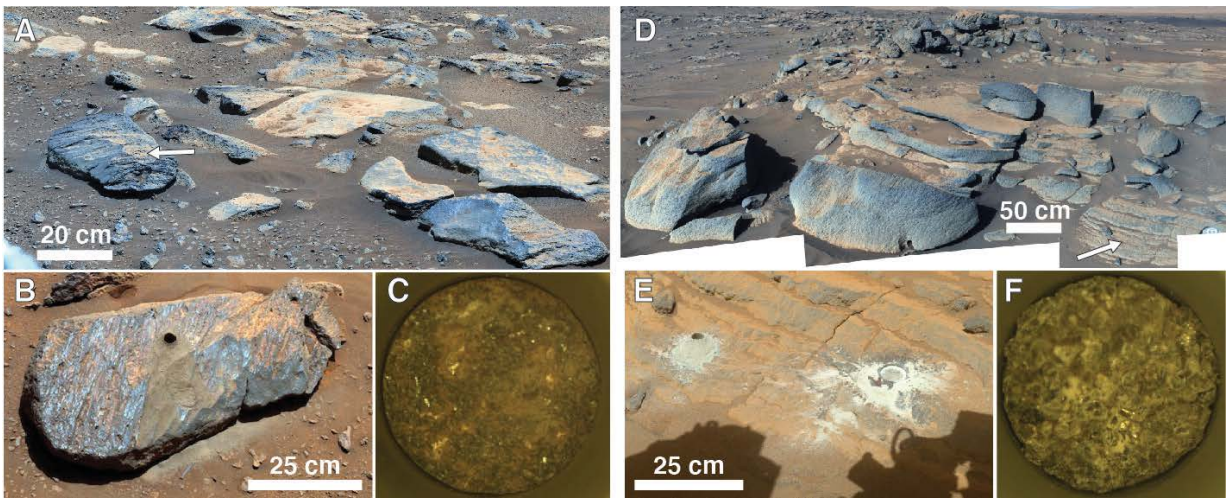

Fig. 7. Core samples collected for potential return to Earth. (**A**) Máaz formation Rochette member outcrop. The white arrow indicates the sampled rock, part of an apparent degrading layer on the crest of Artuby ridge. Enhanced color Mastcam-Z mosaic acquired on sol 180. (B) Close up of the sampled rock, showing the core hole. The Bellegarde abrasion patch is located directly below the hole, partly buried by tailings. Perseverance Navigation Camera (Navcam) (*81*) image acquired on sol 190, white-balanced with slight color saturation applied. (C) White-balanced Cache Camera (CacheCam) (*81*) image of the bottom of the core named Montdenier associated with the Bellegarde abrasion patch, contained in its sample tube, acquired on sol 194. The sample is 1.3 cm in diameter and about 5.5 cm long. (D) The white arrow indicates sampling site on thinly layered Séítah formation Bastide member outcrop. Enhanced color mosaic acquired by Mastcam-Z on sol 240. (E) Core hole and Dourbes abrasion patch imaged by the front Hazard Camera (Hazcam) (*81*) on sol 263. This image has been white-balanced with a slight color

saturation applied. (**F**) White-balanced CacheCam image of the bottom of the core named Salette associated with the Dourbes abrasion patch, acquired on sol 262.

Science
AAAS

Supplementary Materials for

Aqueously altered igneous rocks sampled on the floor of Jezero crater, Mars

K.A. Farley, K.M. Stack, D.L. Shuster, B.H.N. Horgan, J.A. Hurowitz, J..D. Tarnas, J.I. Simon, V.Z. Sun, E.L. Scheller, K.R. Moore, S.M. McLennan, P.M. Vasconcelos, R.C. Wiens, A.H. Treiman, L.E. Mayhew, O. Beyssac, T.V. Kizovski, N.J. Tosca, , Kenneth H. Williford, L. S. Crumpler, L.W. Beegle, J.F. Bell III, B.L. Ehlmann, Y. Liu, J.N. Maki, M.E. Schmidt, A.C. Allwood, H.E.F. Amundsen, R. Bhartia, T. Bosak, A.J. Brown, B.C. Clark, A. Cousin, O. Forni, T.S.J. Gabriel, Y. Goreva, S. Gupta, S.-E. Hamran, C.D.K. Herd, K. Hickman-Lewis, J.R. Johnson, L.C. Kah, P.B. Kelemen, K.B. Kinch, L. Mandon, N. Mangold, C. Quantin-Nataf, M.S. Rice, P. S. Russell, S. Sharma, S. Siljeström, A. Steele, R. Sullivan, M. Wadhwa, B.P. Weiss, A.J. Williams, B.V. Wogsland, P.A. Willis, T. A. Acosta-Maeda, P. Beck, K. Benzerara, S. Bernard, A.S. Burton, E.L. Cardarelli, B. Chide, E. Clavé, E.A. Cloutis, B.A. Cohen, A.D. Czaja, V. Debaille, E. Dehouck, A.G. Fairén, D.T. Flannery, S.Z. Fleron, T. Fouchet, J. Frydenvang, B.J. Garczynski, E.F. Gibbons, E.M. Hausrath, A.G. Hayes, J. Henneke, J.L. Jørgensen, E.M. Kelly, J. Lasue, S. Le Mouélic, J.M. Madariaga, S. Maurice, M. Merusi, P.-Y. Meslin, S.M. Milkovich, C.C. Million, R.C. Moeller, J.I. Núñez, A.M. Ollila, G. Paar, D.A. Paige, D.A.K. Pedersen, P. Pilleri, C. Pilorget, P.C. Pinet, J.W. Rice Jr., C. Royer, V. Sautter, M. Schulte, M.A. Sephton, S.K. Sharma, S.F. Sholes, N. Spanovich, M. St. Clair, C.D. Tate, K. Uckert, S.J. VanBommel, A.G. Yanchilina, M.-P. Zorzano

Correspondence to: Kenneth.a.farley@jpl.nasa.gov

This PDF file includes:

Materials and Methods

PIXL Data and Computation of Alteration-Corrected PIXL XRF Compositions

PIXL is an X-ray fluorescence instrument for mapping the elemental composition of a rock surface from a few cm standoff (*33*). The fully calibrated PIXL data described here are described and archived in the NASA Planetary Data System (*75*) with specific data references for each figure listed in the Figure Image and Data References section below. For further details see (*39*) and the data description in the Planetary Data System PIXL archive bundle (*75*).

PIXL data on abrasion patches include a large number of individual data points, some of which are associated with high S and Cl concentrations likely derived from external sources. To estimate the primary bulk compositions prior to the addition of S and Cl, we assumed zero initial concentrations of both of these elements and performed a three-step calculation:

i) We excluded from the bulk composition for the abrasion patch all individual points that exceeded threshold levels of SO_3 or Cl. The threshold levels were varied between abrasion patches and were chosen such that the bright white salt-rich regions (Figure 3) were effectively excluded. We selected 2 wt% of either SO_3 or Cl for Bellegarde, 2 wt% SO_3 or 5 wt % Cl for Guillaumes, and 1 wt% of either SO_3 or Cl for Dourbes.

ii) The remaining S was assumed to be associated with an exogenous phase, with a molar Ca/S ratio of 1 (e.g., $CaSO_4$). Cl was assumed to be associated with an exogenous phase with molar Na/Cl of 1 (e.g., halite or Na perchlorate). Eliminating this remaining S and Cl reduced both Ca and Na accordingly.

iii) Elemental totals for this average exogenous-element-free composition were normalized to 100%.

Ground Penetrating Radar Data and Processing

The data in Fig. S3 were collected with the Radar Imager for Mars' Subsurface Experiment (RIMFAX) ground penetrating radar, see (*29*) for a technical description of this instrument. The data used in this work can be found in the Planetary Data System RIMFAX archive bundle (*76*). The processing of the data is the same as described in the RIMFAX Calibrated Data Record (CDR) Software Interface Specification (*76*). Prior to plotting, a depth-dependent gain factor was applied to the time domain data to improve visibility of deeper reflectors.

SHERLOC Data and Reference Spectra

SHERLOC is a deep-ultraviolet Raman and fluorescence spectrometer for mapping organic molecules and certain minerals and chemicals on rock surfaces (*31*). The fully calibrated SHERLOC spectra described here are described and archived in the Planetary Data System SHERLOC archive bundle (*77*) with specific data references for each figure listed in the Figure Image and Data References section below. SHERLOC Raman and fluorescence spectra were interpreted based on libraries of reference spectra (*82–85*).

Supercam Data and Reference Spectra

Supercam is a multipurpose remote sensing instrument for elemental and mineralogical characterization (*32, 86*). The fully calibrated Supercam data reported here are described and archived in the Planetary Data System Supercam archive bundle (*78*) with specific data references for each figure listed in the Figure Image and Data References section below. For further methodological details on Supercam IR spectroscopy, see (*87*).

Creation of Stratigraphic Columns

Schematic stratigraphic columns were constructed throughout the study area through a synthesis of orbiter image and topographic data and in-situ rover image data via methods similar to those previously used (*88*). Specific outcrops were first localized in a HiRISE base map of the study area (*89*), and elevation values for the top and bottom of each outcrop were extracted from the HiRISE digital terrain model (DTM, (*90*)) to calculate the total elevation range of each outcrop. In-situ observations of lithology, texture, and fabric gleaned from Navcam,

Mastcam-Z, Supercam, and WATSON were used to determine which members were present within each outcrop. The location of individual member boundaries within each section was estimated using in-situ rover Navcam meshes, then translated to the stratigraphic column constrained in elevation by the HiRISE DTM. No correction for dip has been applied, therefore these columns represent the elevation distribution of geologic members throughout the study area, rather than true thickness.

Supplementary Text

Sampling

Perseverance collected samples from rock outcrops as drill cores, nominally 6 cm in length and ~1 cm in diameter. Each sample core was drilled directly into an ultraclean sample tube using a rotary-percussive coring drill (1). After coring, the filled sample tube was passed from the drill into the rover body, where an image was acquired viewing down the tube bore (Cachecam image (81)). The length of core was then estimated, and each tube was hermetically sealed. Sample tubes are currently stored on board Perseverance; they will potentially be returned to Earth by a future spacecraft mission. The design of that mission has not yet been determined; Perseverance has the facility for direct transfer, or to drop the sample tubes at a cache location on the Martian surface for later pickup.

Feature Names and Use of Navajo Language

Before launch, the Perseverance Science Team divided the rover's landing site into a grid of quadrangles 1.2 km by 1.2 km. Each quad was named after a national park or preserve on Earth, and provides the inspiration for informal names used for in-situ targets, abrasions, and sample cores. Perseverance landed in the quad named for Arizona's Canyon de Chelly National Monument in the heart of Navajo Nation. The Perseverance Science Team leadership worked with JPL engineer Aaron Yazzie and leaders of Navajo Nation including President Jonathan Nez and Vice President Myron Lizer to compose a list of Navajo terms that could be used to name features on Mars. The accent marks used to convey the intonation of the Navajo language cannot be read by mission software, so the mission uses English letters without special characters or punctuation to represent Navajo words. The simplified spelling used by the rover mission, the spelling, punctuation, and translation provided by Navajo Nation are shown below.

Mission Name	Navajo Term	Meaning
Seitah	Séítah	sand dunes, sandy, amidst the sand
Maaz	Máaz	Mars
Nataani	Naat'áanii	leader, leadership
Chal	Ch'ał	frog

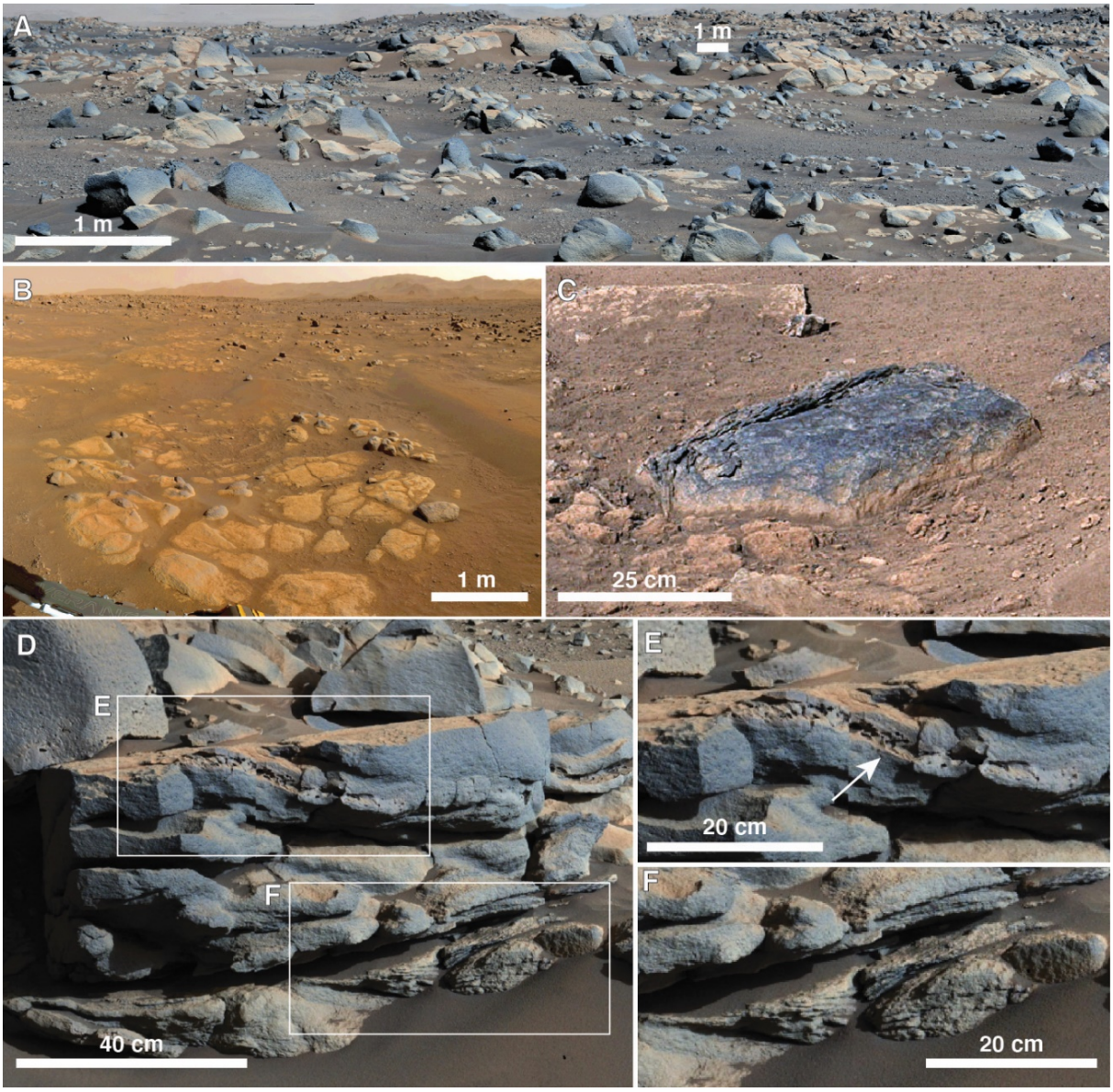

Fig. S1. Characteristic outcrops of the Máaz formation. (**A**) Apparently structureless boulders and blocky outcrop of the Chal member. Enhanced color Mastcam-Z mosaic of the target area Chal acquired on sol 78. (B) Low-relief, polygonally fractured outcrop (informally named Baa Big Han) of the Nataani member imaged by Navcam on sol 66. Mosaic has been white balanced with a slight color saturation applied. (C) Spheroidal weathering observed around the edges of a block of the Nataani member imaged by Mastcam-Z on sols 3-11. Mosaic has been color enhanced. (D) Erosion-resistant caprock of the Rochette member exposed at the Mure outcrop. Poorly developed dm-scale layers overlie, and possibly truncate, thin layers at the base of the outcrop. Enhanced color Mastcam-Z mosaic acquired on sol 168. (E) A concentration of voids several cm in thickness that aligns with the curvilinear shape of poorly developed layering within the Mure outcrop. (F) Cm-scale layers at the base of the Mure outcrop that truncate or pinch out below the resistant caprocks of the Rochette member.

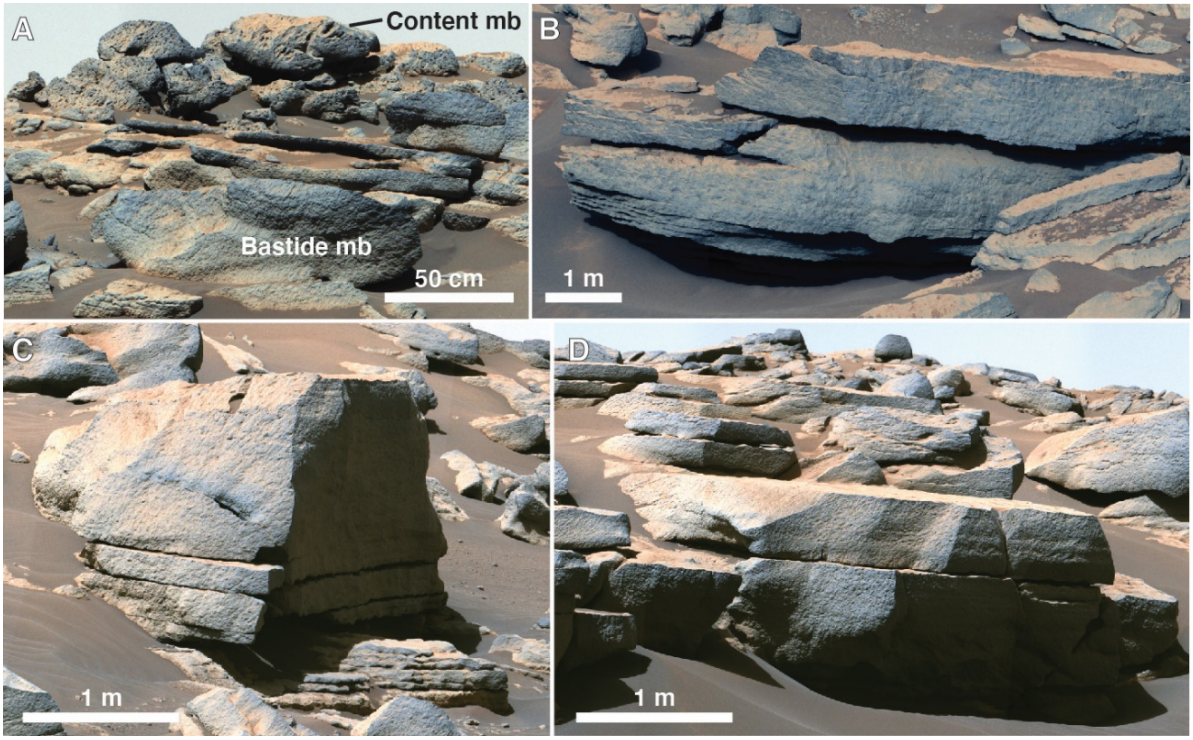

Fig. S2. Characteristic outcrops of the Séítah formation. (**A**) Heavily pitted, apparently structureless rocks of the Content member overlie the layered resistant rocks of the Bastide member. Enhanced color Mastcam-Z mosaic acquired on sol 238. (B) Cm to dm cyclic layers within the Bastide member at the Village outcrop. Enhanced color Mastcam-Z mosaic acquired on sol 211. (C) Apparent thickening upward trend observed in layers of Bastide member at the Val de Graves outcrop. Cyclic cm-scale layers at the base of the outcrop thicken upward to an apparently massive bed ~1.5 meters in thickness. Enhanced color Mastcam-Z mosaic acquired on sol 205. (D) Dm to m-thick tilted planar layers of the Bastide formation near the Val de Grave outcrop. Weak decimeter scale layering is observed within a thicker layer that is apparently massive on other faces. Enhanced color Mastcam-Z mosaic acquired on sol 205.

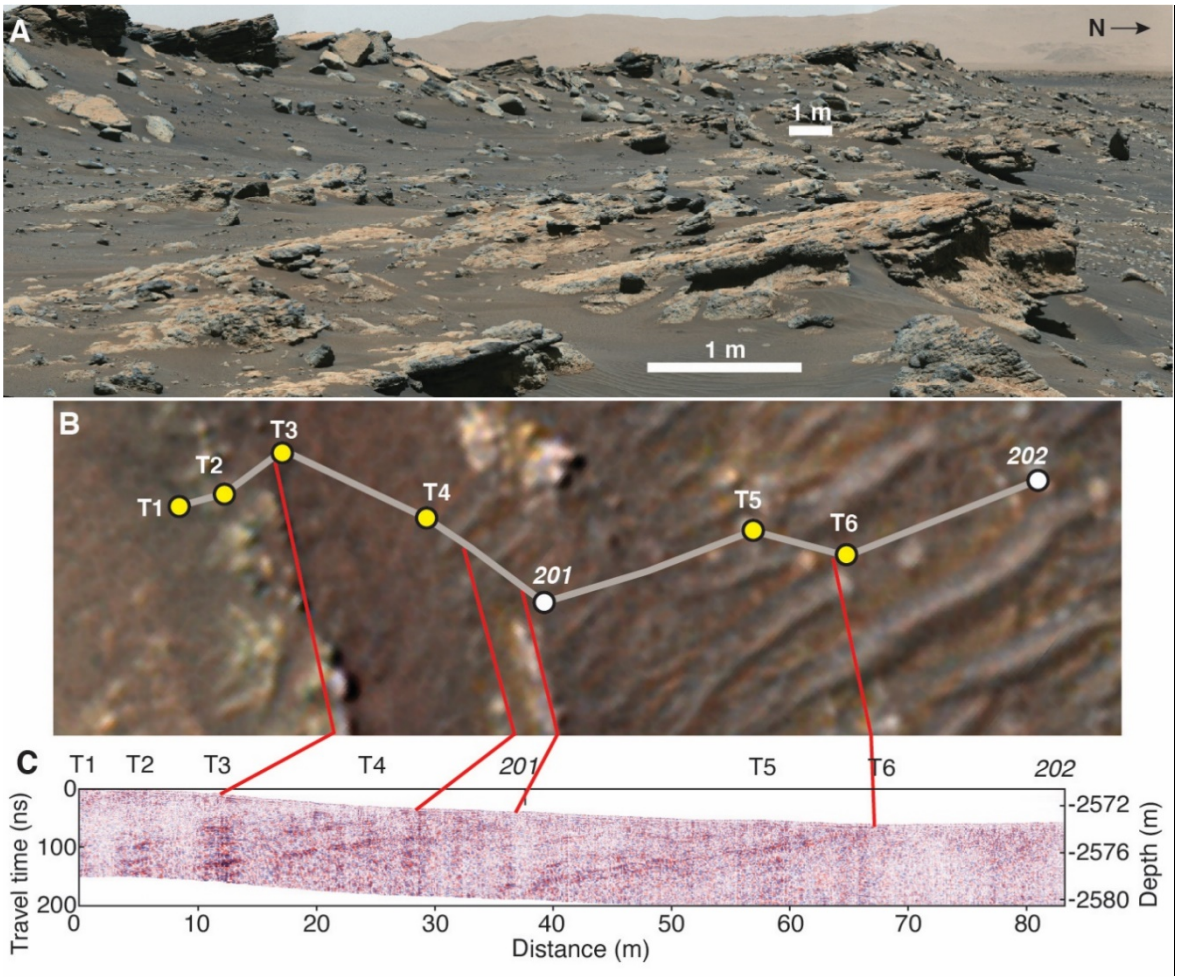

Fig. S3. Dipping layers of Artuby ridge and in the subsurface. (**A**) Lombard outcrop on Artuby ridge, showing the dipping layers of the Artuby (lower) and Rochette (upper) members of the Máaz formation. This enhanced color Mastcam-Z mosaic acquired on sol 202 has been mirrored to show same sense of dip as the lower panels. (B) HiRISE orbital image showing rover traverse (white line segments) from the crest of Artuby ridge into the Séítah formation. See Fig.1 for location. Yellow points labelled T indicate rover turns. White numbers indicate mission sol. Red lines map outcrop to the associated radar reflector in panel C. Based on the geochemical distinction between Máaz and Séítah, their contact lies beneath regolith between T3 and T4. (C) RIMFAX ground penetrating radar returned radar signal down to 7 m depth (~200 ns in the time domain) acquired during the sol 201 and 202 drives reveals subsurface layers dipping at the same angle as seen on Artuby ridge, panel A. Outcropping layers of the Séítah formation, e.g., at the Sol 201 point, dip below Artuby ridge and therefore lie stratigraphically below the Máaz formation. North is to the right in all panels.

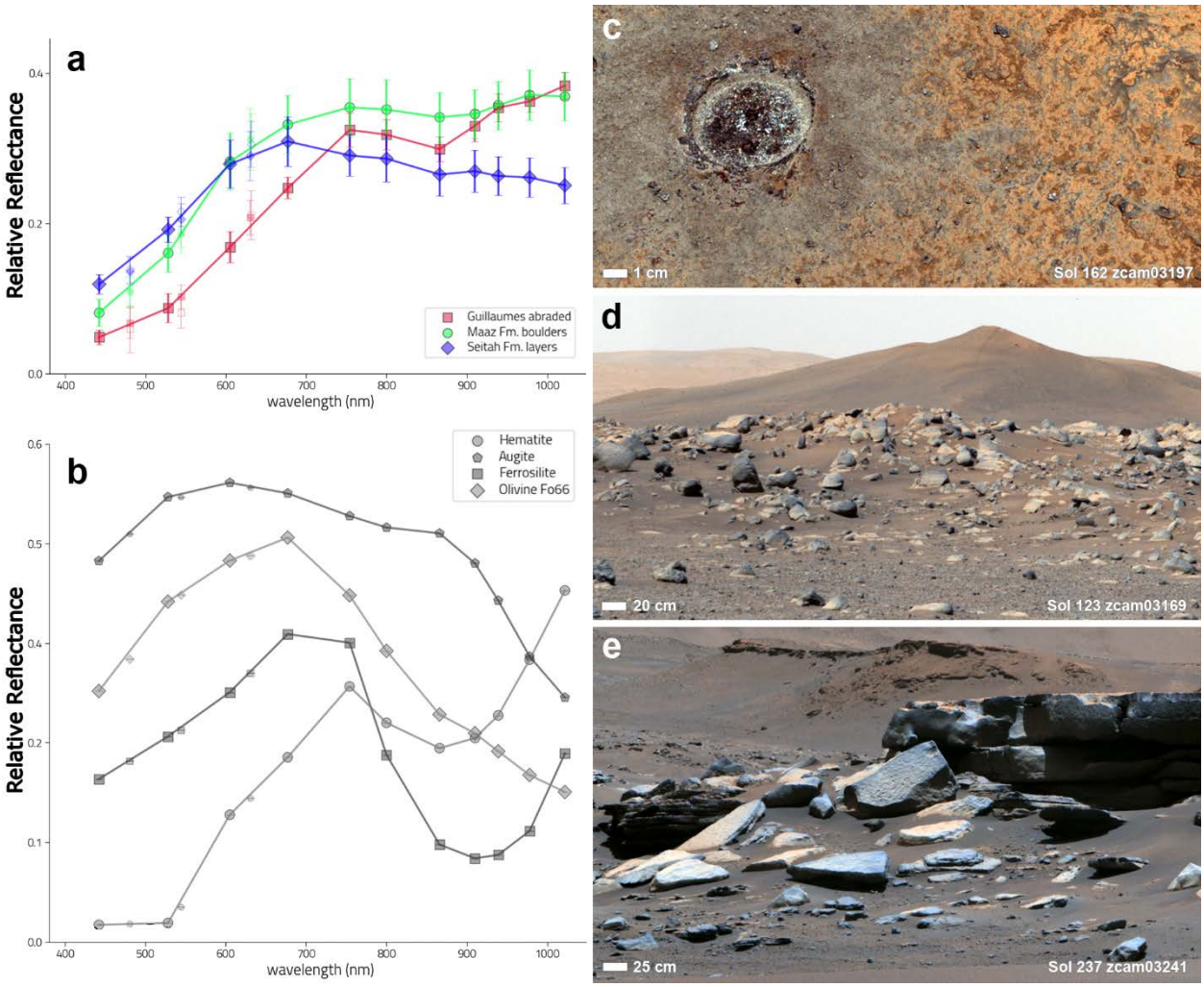

Fig S4. Mastcam-Z multispectral image summary. (A) Mastcam-Z visible/near-infrared reflectance spectra of representative endmembers from natural surfaces of the Máaz (green circles) and Séítah (blue diamonds) formations as well as red-brown zones within the Guillaumes abrasion patch within the Máaz formation (red squares). Source images are shown in panels C-E, and values are relative to a rover-mounted calibration target and assume Lambertian scattering. (b) Laboratory visible/near-infrared reflectance spectra (*91*) convolved with Mastcam-Z bandpasses. Mastcam-Z 110 mm focal length Bayer filter enhanced color images of (c) the Guillaumes abrasion patch, (d) Máaz formation boulders in the foreground of the Santa Cruz landform, and (e) the Roya target within the Séítah formation.

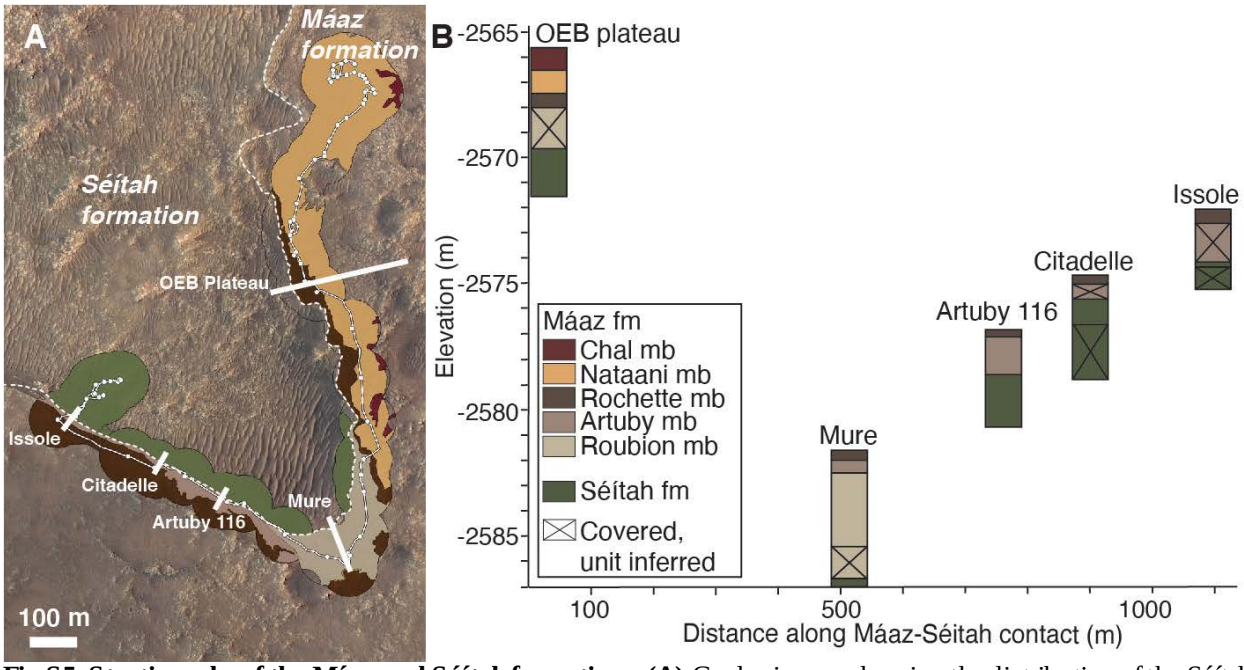

Fig S5. Stratigraphy of the Máaz and Séítah formations. (A) Geologic map showing the distribution of the Séítah and Máaz formations (contact dashed in white) and their members (mb). Bold white lines show the approximate locations of the five sections reported in (B). **(B)** Generalized stratigraphic columns showing the elevation and distribution of Máaz formation members laterally along the Máaz-Séítah contact.

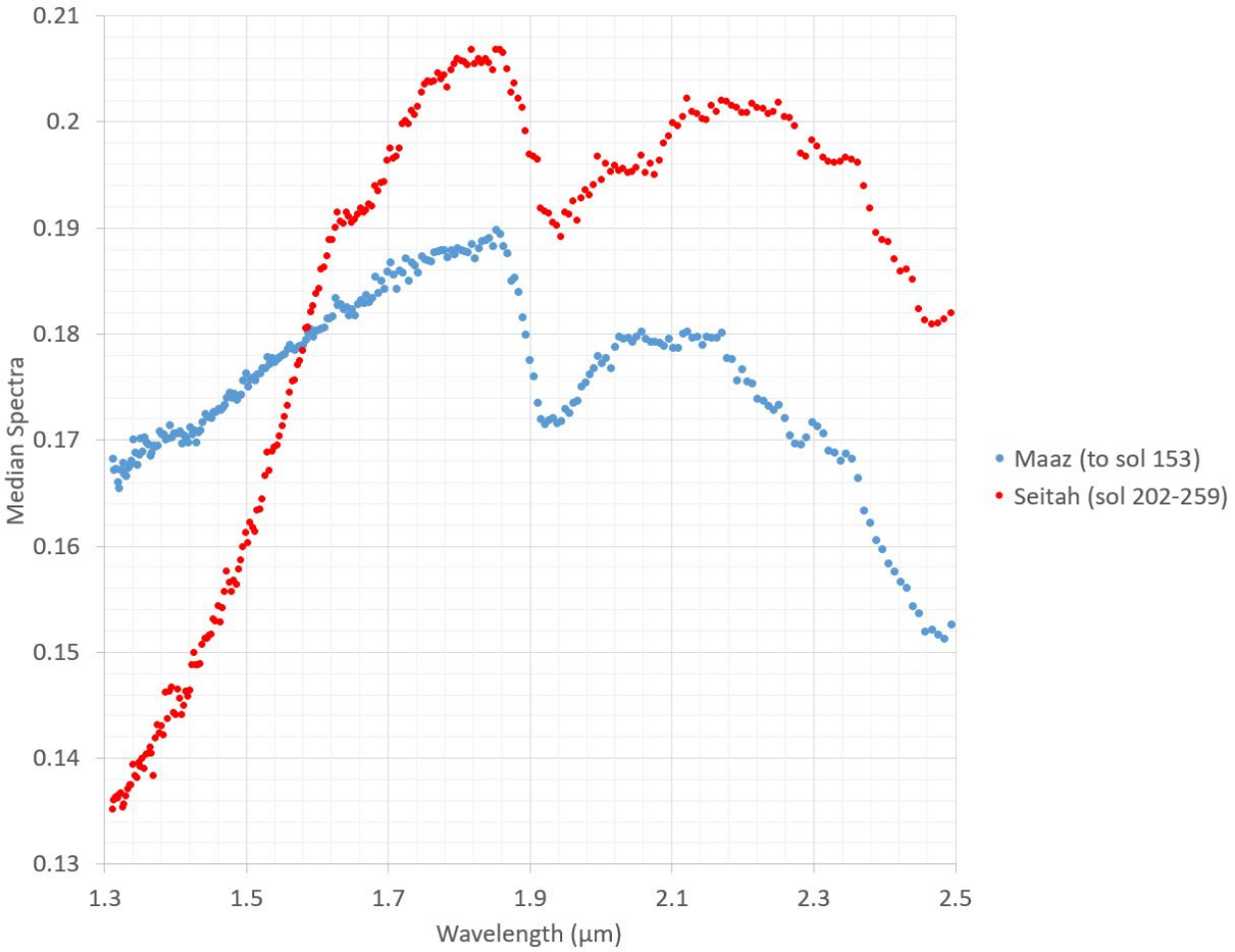

Fig S6. Supercam infrared spectra of Maaz and Seitah formation rocks. In blue is the median reflectance of all spectra acquired on Máaz targets before Sol 153. In red is the median reflectance of all spectra acquired on Séítah targets from Sol 202 to Sol 259. The spectra are calibrated and corrected for atmospheric absorption (*87*). Both formations show a prominent 1.9 um absorption band associated with hydrated iron oxides, ferric smectites, and/or hydrated salts (*36*). The steep slope at short wavelength in Séítah suggest the presence of olivine (*36*).

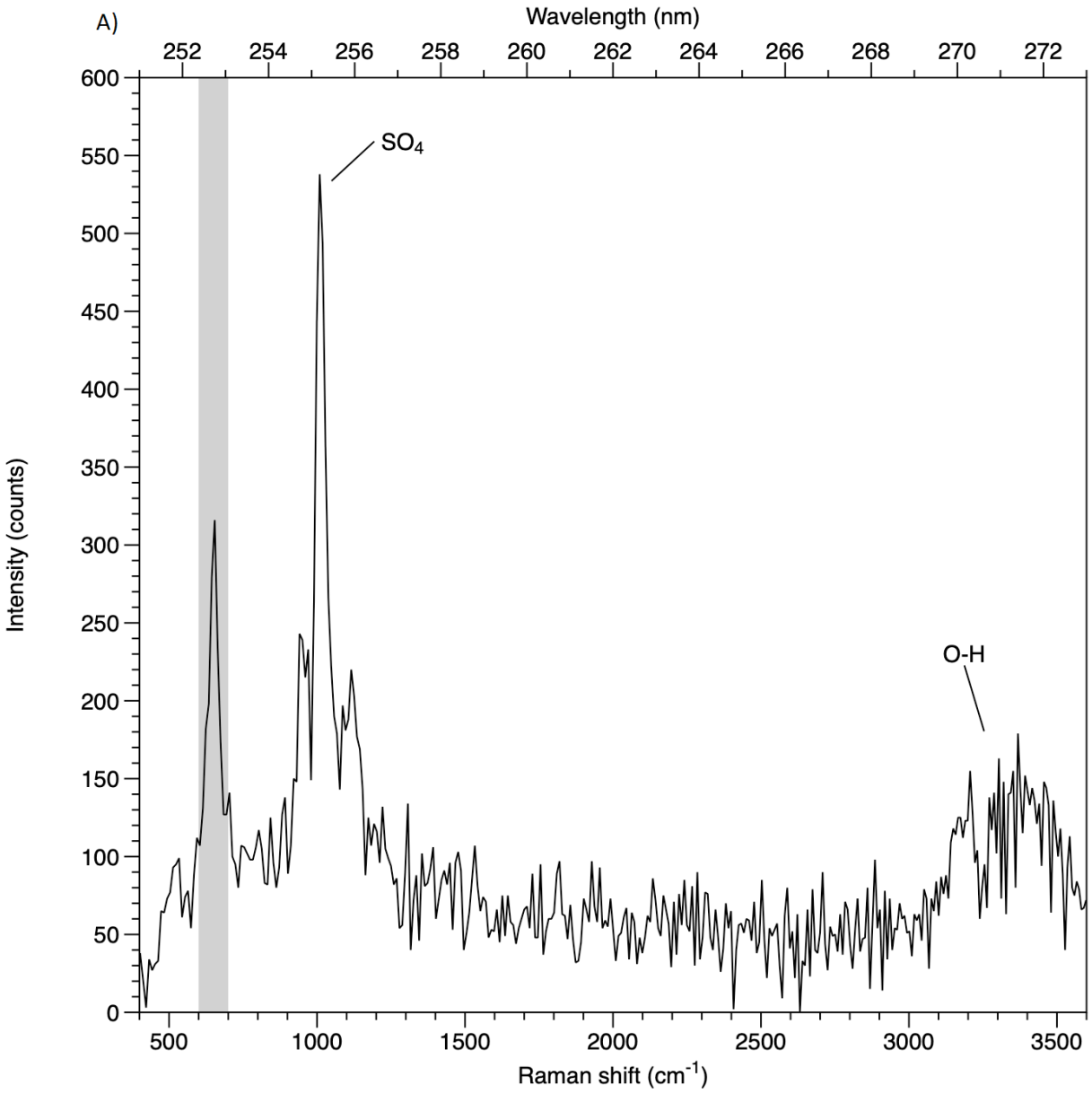
A)
Wavelength (nm)
252
254
256
258
260
262
264
266
268
270
272
600
550
500
450
400
350
300
250
200
150
100
50
0
Intensity (counts)
SO4
O-H
500
1000
1500
2000
2500
3000
3500
Raman shift (cm-1)

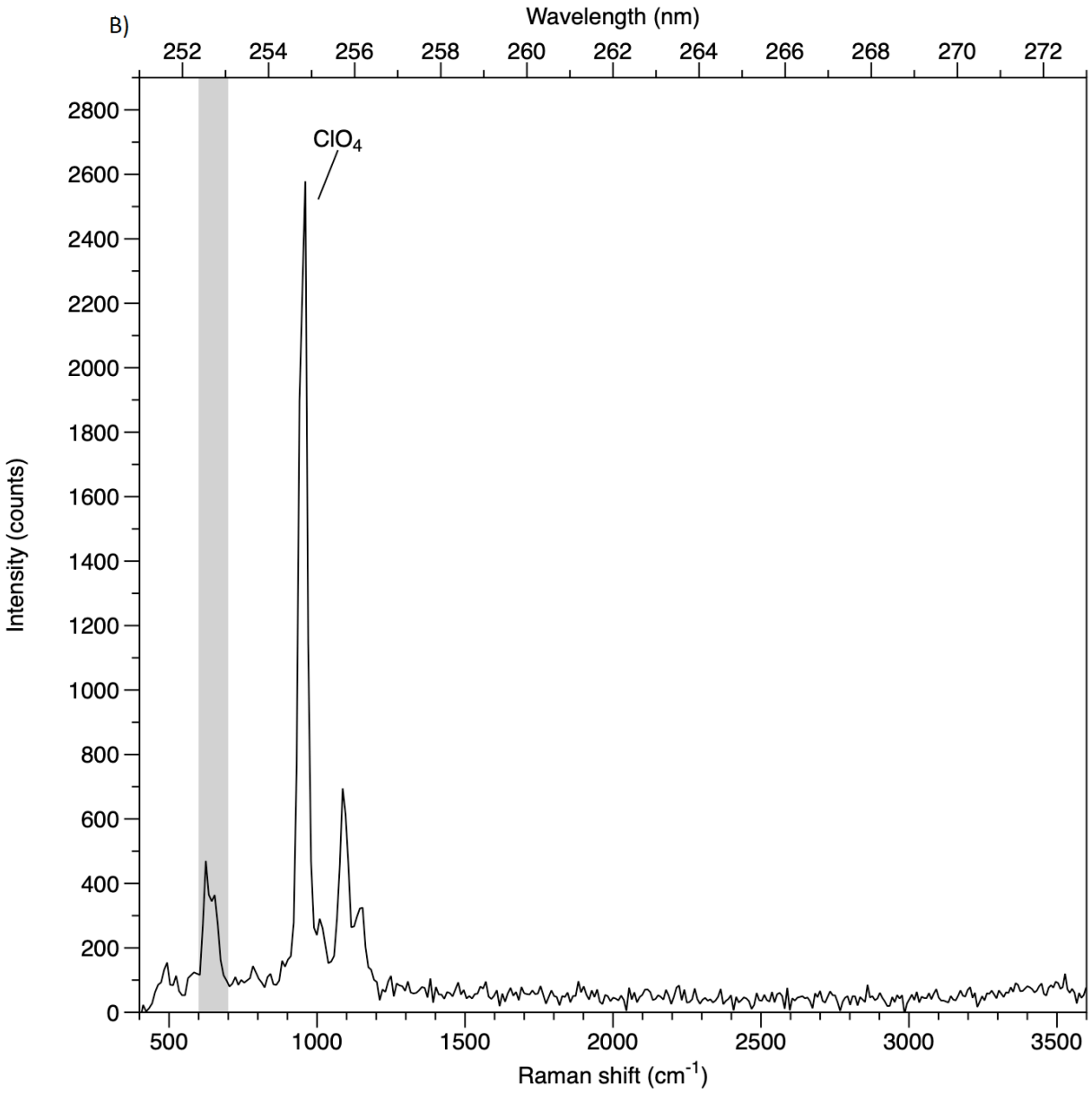
B)
Wavelength (nm)
252
254
256
258
260
262
264
266
268
270
272
2800
2600
2400
2200
2000
1800
1600
1400
1200
1000
800
600
400
200
0
ClO4
Intensity (counts)
500
1000
1500
2000
2500
3000
3500
Raman shift (cm-1)

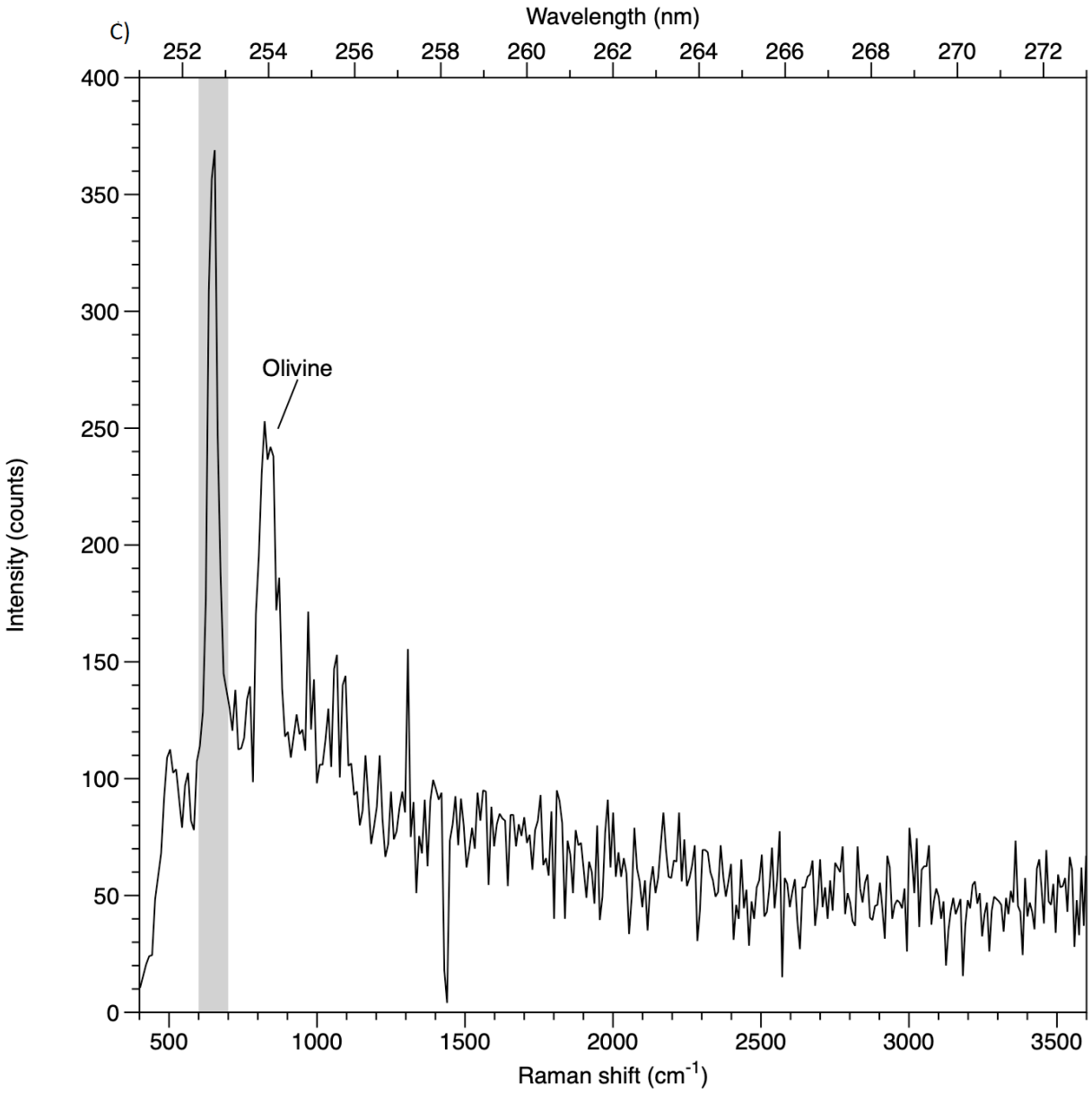
C)
Wavelength (nm)
252
254
256
258
260
262
264
266
268
270
272
400
350
300
250
200
150
100
50
0
Intensity (counts)
Olivine
500
1000
1500
2000
2500
3000
3500
Raman shift (cm-1)

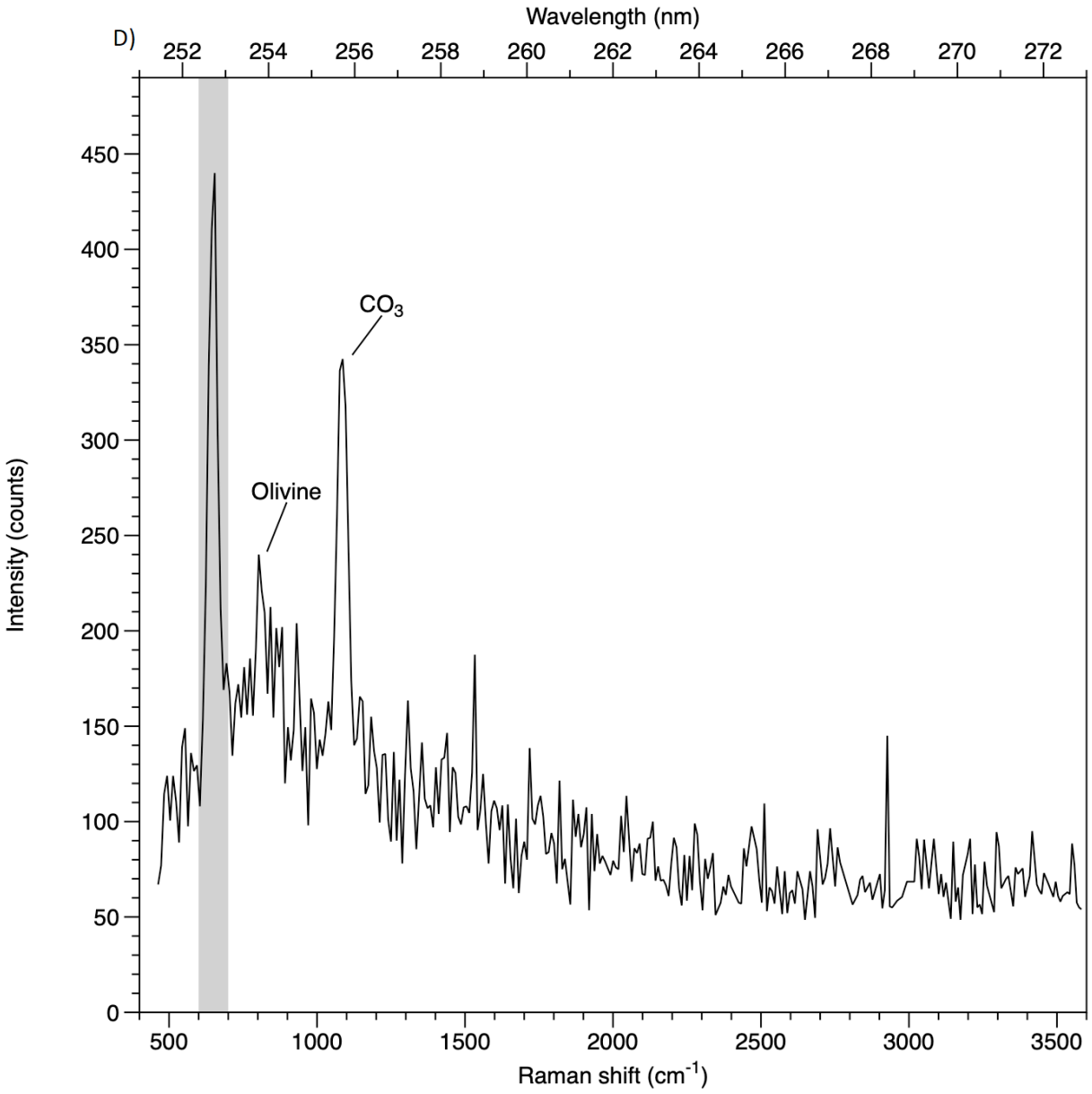
D)
Wavelength (nm)
252
254
256
258
260
262
264
266
268
270
272
Intensity (counts)
0
50
100
150
200
250
300
350
400
450
CO_3
Olivine
500
1000
1500
2000
2500
3000
3500
Raman shift (cm^{-1})

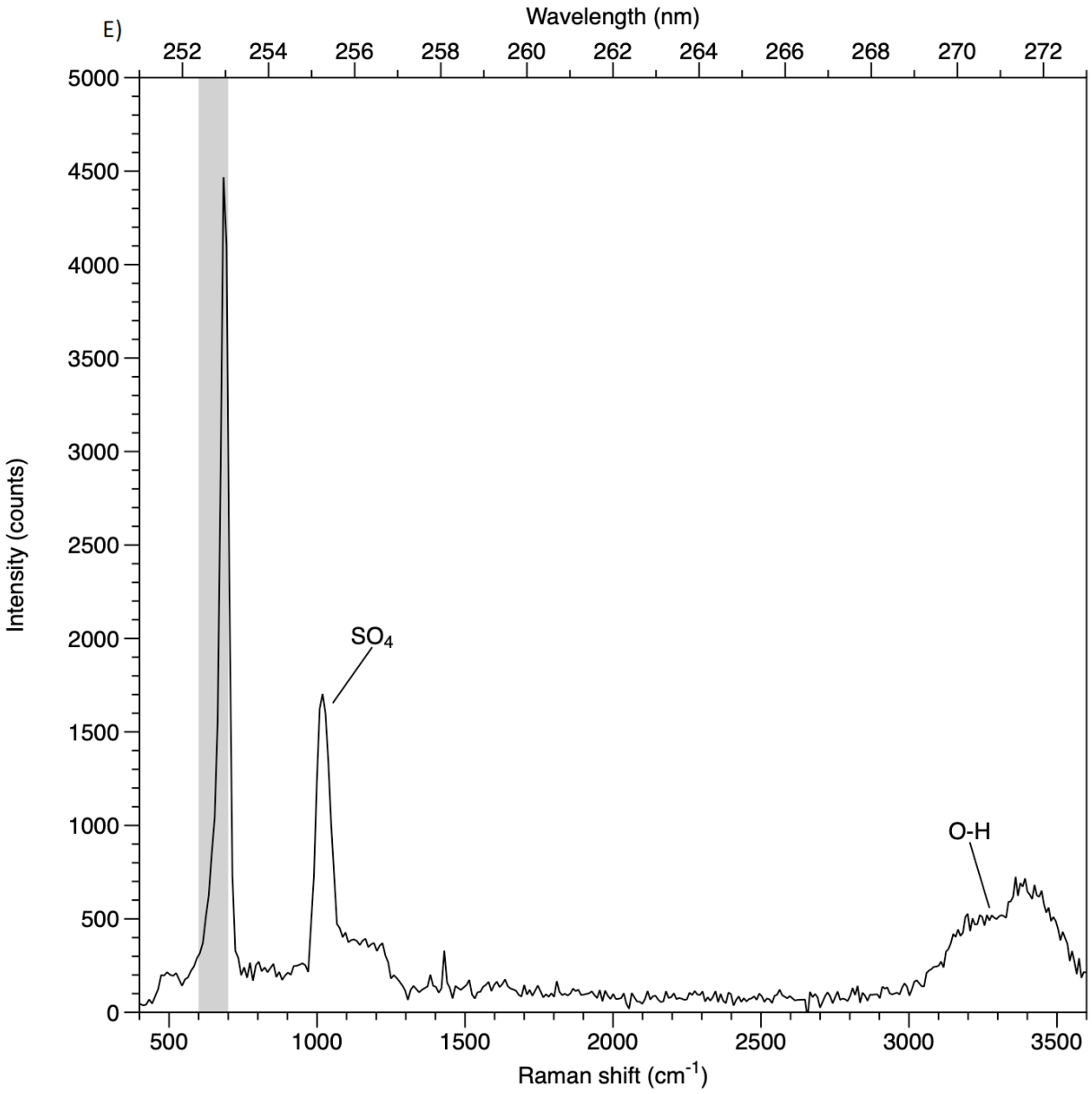
E)
Wavelength (nm)
252
254
256
258
260
262
264
266
268
270
272
5000
4500
4000
3500
3000
2500
2000
1500
1000
500
0
Intensity (counts)
SO4
O-H
500
1000
1500
2000
2500
3000
3500
Raman shift (cm-1)

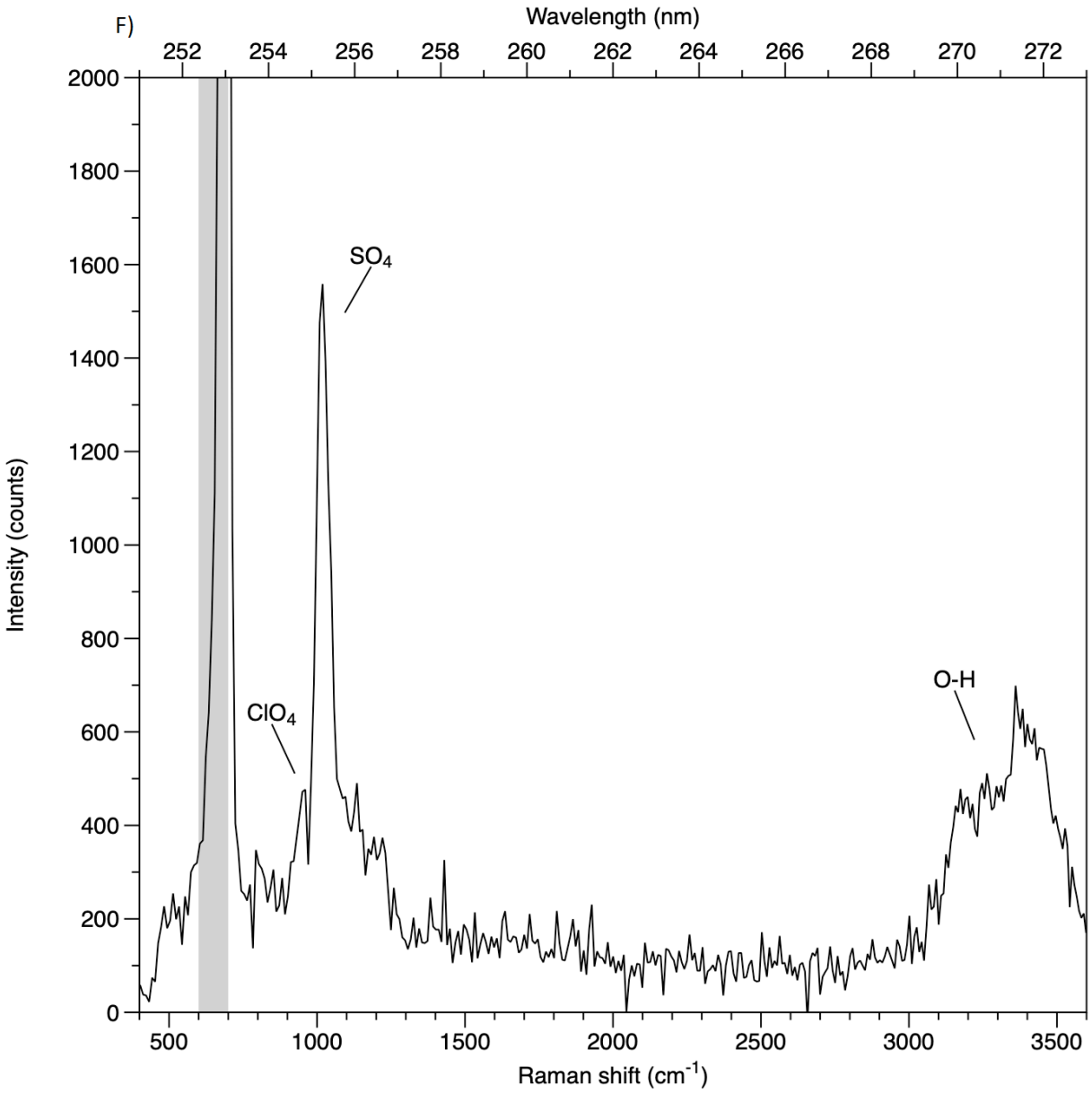
F)
Wavelength (nm)
252
254
256
258
260
262
264
266
268
270
272
2000
1800
1600
1400
1200
1000
800
600
400
200
0
Intensity (counts)
SO4
ClO4
O-H
500
1000
1500
2000
2500
3000
3500
Raman shift (cm-1)

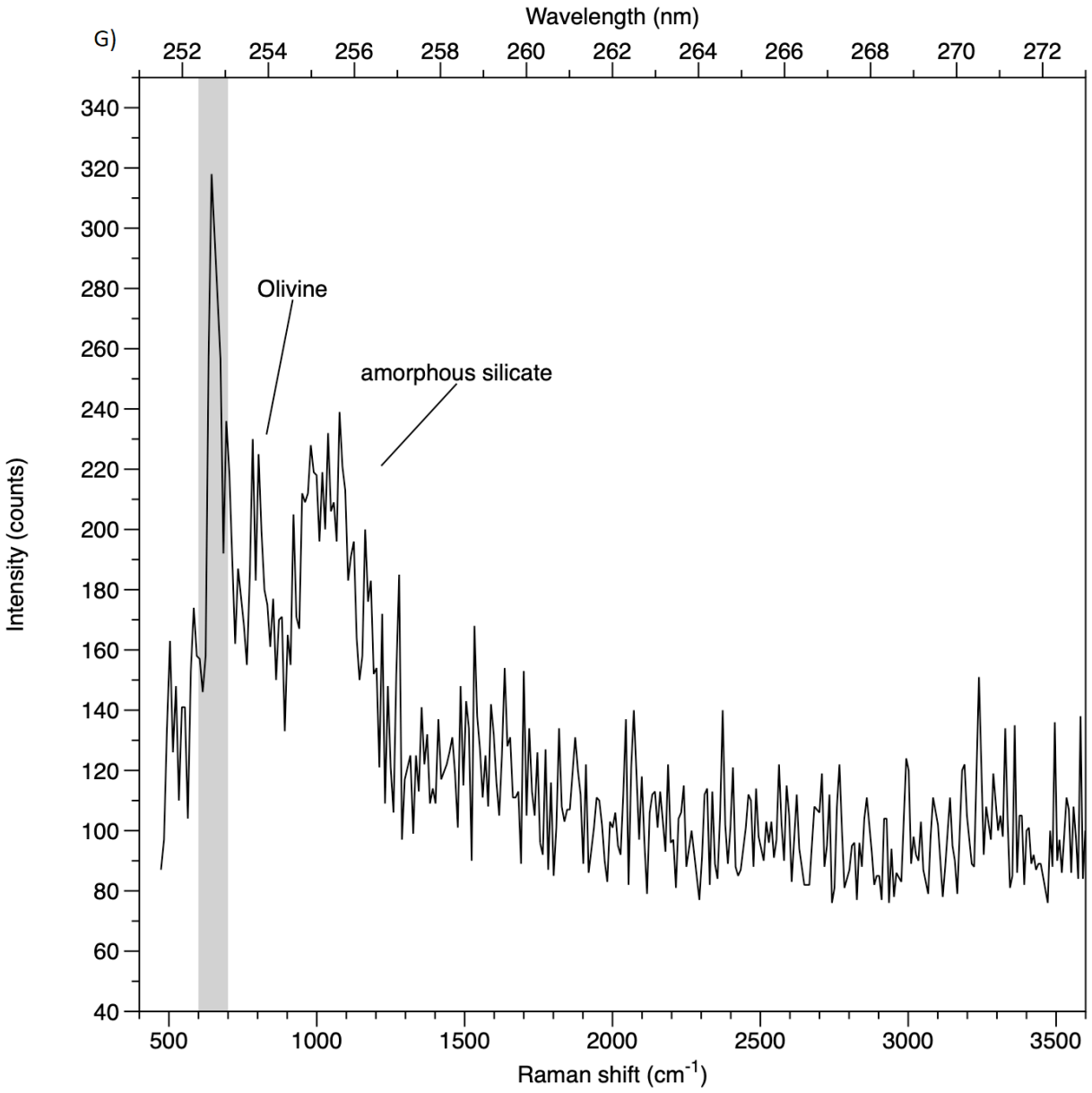

Fig. S7 SHERLOC Raman spectra. (A) Representative spectra interpreted as sulfate and (B) perchlorate in bright white material in Máaz abrasion patch Guillaumes on sol 169. Representative spectra interpreted to be (C) olivine and (D) mixed olivine and carbonate in Séítah abrasion patch Garde obtained on sol 208. (E) Representative spectrum interpreted to be sulfate in small white patch within red-brown interstitial material in Séítah abrasion patch Dourbes on sol 269. (F) Representative spectrum interpreted to be sulfate and perchlorate in bright white material in Séítah abrasion Dourbes on sol 269. (G) Raman spectrum tentatively interpreted as amorphous silicate broadly distributed in Séítah abrasion patch Dourbes on sol 269. In all panels the grey band indicates a region with lines associated with the excitation laser.

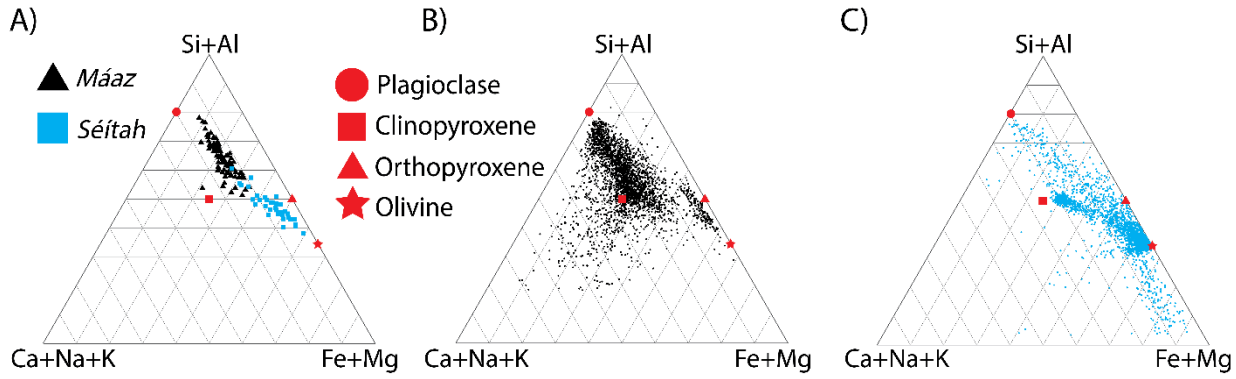

Fig. S8. Geochemistry of Máaz and Séítah formation rocks. (A) Ternary composition plot based on Supercam LIBS data, showing that target-averaged Máaz rocks (black triangles) are distinct from Séítah rocks (blue squares). While Máaz rocks are dominated by mixtures of augite and plagioclase, Séítah rocks are dominantly mixtures of olivine and augite (with or without minor plagioclase). (B) Equivalent ternary plot using PIXL XRF data from Guillaumes. The results are similar to panel A, but with greater heterogeneity because every data point in the abrasion patch is plotted. There are additional points at high Ca+Na+K, indicating the presence of Ca sulfates and NaCl or Na perchlorate. The array of points along the Si+Al - Fe+Mg join maps to the dark material in Fig. 3A. (C) Same as panel B, but for Dourbes in Seitah. Trend towards high Fe+Mg is indicative of carbonates and sulfates enriched in these cations. In each panel, red symbols indicate various mineral standards.

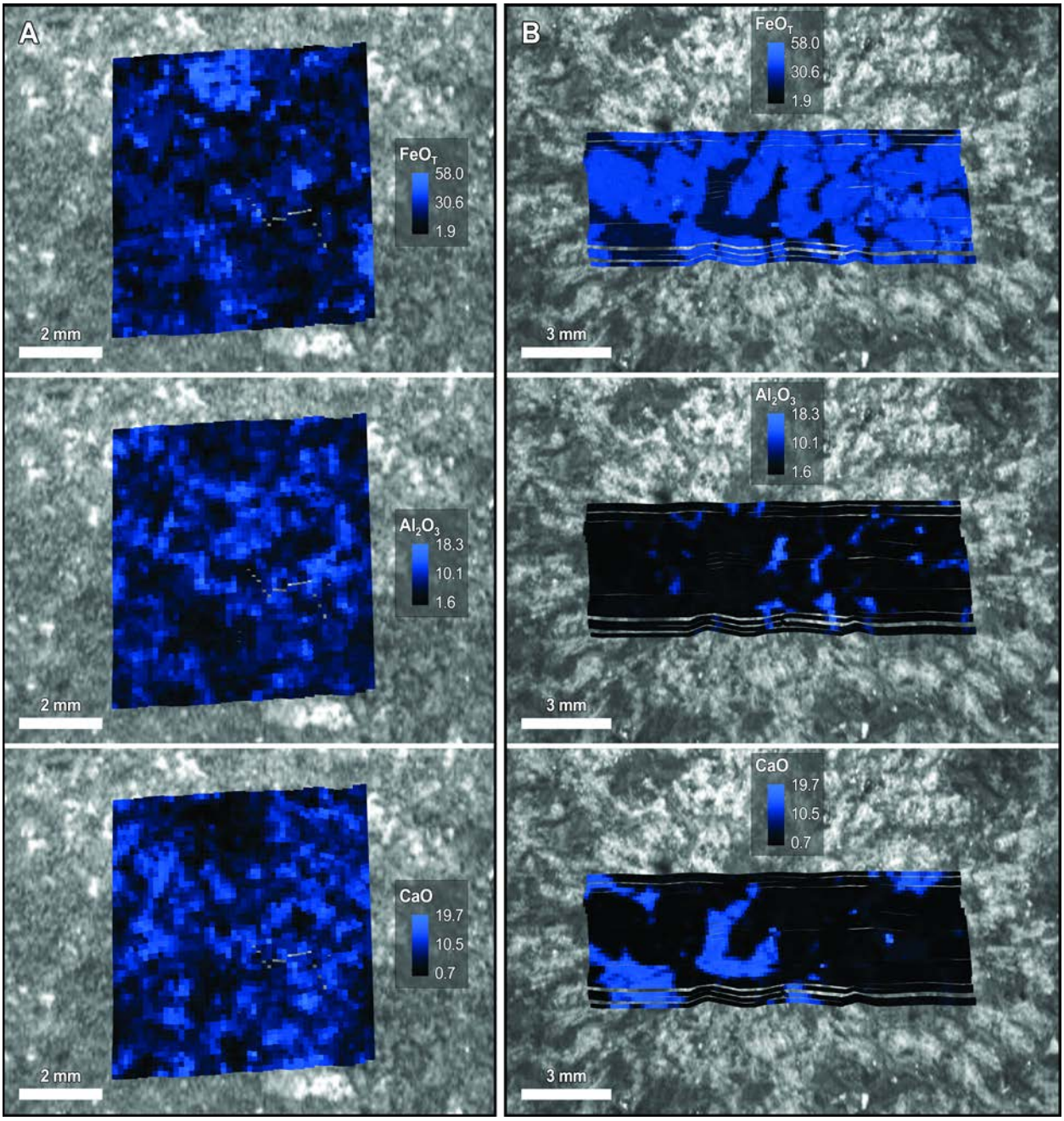

Fig S9. Blue-scale single-element concentration maps for (A) Guillaumes abrasion patch and (B) Dourbes abrasion patch. These data are equivalent to Figure 5 and are provided here to assist in interpretation of the color map**.** FeO_T is total iron reported as Fe^{+2}.

Table S1. LIBS average elemental compositions. Average elemental compositions for 67 Máaz formation rocks and 25 Séítah formation Bastide member rocks, derived using Supercam LIBS. N is the number of individual LIBS shot points in the average. LIBS is not sensitive to all major elements, and reported values are not normalized to 100%. Indicated uncertainties are the mean calibration accuracy of the instrument (*92*). FeO_T is total iron reported as Fe^{+2}.

	Máaz	*Séítah*
	LIBS	LIBS
Wt %	Average	Average
SiO_2	47.83 ± 6.1	45.03 ± 6.1
TiO_2	0.66 ± 0.3	0.23 ± 0.3
Al_2O_3	8.70 ± 1.8	4.14 ± 1.8
FeO_T	19.47 ± 3.1	22.88 ± 3.1
MgO	3.01 ± 1.1	21.10 ± 1.1
CaO	5.69 ± 1.3	3.97 ± 1.3
Na_2O	2.79 ± 0.5	1.32 ± 0.5
K_2O	0.91 ± 0.6	0.21 ± 0.6
Total	89.07	98.88
N	624	284

Table S2. PIXL XRF elemental data. Indicated uncertainty is estimated accuracy based on analysis of standards (see (*39*) for details). N is the number of individual data points averaged. Raw data are listed along with the results after adjustment for subsequent alteration processes, see Methods. Average Máaz includes data for both Bellegarde and Guillaumes abrasion patches. Séítah is the average composition of the Dourbes abrasion patch. FeO_T is total iron reported as Fe^{+2}.

	Average Máaz				Séítah			
wt %	All points		Alteration Adjusted		All points		Alteration Adjusted	
		±		±		±		±
SiO_2	41.90	2.10	48.81	2.89	39.42	1.98	40.42	2.35
TiO_2	2.04	0.62	2.44	0.70	0.37	0.25	0.39	0.25
Al_2O_3	7.43	0.37	8.80	0.52	2.42	0.55	2.25	0.54
FeO_T	21.47	1.07	21.69	1.28	30.05	1.50	30.61	1.78
MgO	2.46	0.55	2.28	0.57	19.24	0.97	20.29	1.19
CaO	7.87	0.39	7.85	0.58	2.94	0.56	3.15	0.57
Na_2O	5.34	0.67	3.97	0.82	1.93	0.70	1.32	0.65
K_2O	0.92	0.31	1.11	0.36	0.18	0.19	0.15	0.17
MnO	0.46	0.22	0.48	0.25	0.69	0.29	0.70	0.30
Cr_2O_3	0.02	0.05	0.01	0.04	0.26	0.23	0.30	0.24
P_2O_5	2.24	0.65	2.57	0.72	0.48	0.23	0.42	0.25
SO_3	3.01	0.57			0.78	0.27		
Cl	2.56	0.56			0.66	0.23		
SUM	97.72		100.00		99.42		100.00	
N	5618.0		3524.0		5670.0		3878.0	

Data Sources

All Mars 2020 mission data, including fully calibrated data products, are archived on NASA's Planetary Data System. Data used in this paper appear in six data bundles, each associated with one of the mission's instruments.
1. Mastcam-Z (*79*)
2. RIMFAX (*76*)
3. SHERLOC (*77*)
4. PIXL (*75*)
5. Engineering cameras (*80*)
6. Supercam (*78*)

Figure Image and Data References

Figure 1A CTX Color mosaic
https://astrogeology.usgs.gov/search/map/Mars/Mars2020/Jez_MARS2020_CTX_DEM_Scienceh5270_0000_re4
h5270_0000_gr4
h5270_0000_bl4
h5252_0000_re4
h5252_0000_gr4
h5252_0000_bl4

Figure 1B,C HiRISE RGB color mosaic
https://planetarymaps.usgs.gov/mosaic/mars2020_trn/HiRISE/JEZ_hirise_soc_007_orthoMosaic
PSP_002387_1985
PSP_003798_1985
ESP_045994_1985
ESP_059352_1985
ESP_065431_1985
ESP_068426_1985
ESP_065985_1985

Figure 2A
ZL0_0138_0679192442_338RAD_N0051812ZCAM08147_1100LMA03.IMG
ZL0_0138_0679192512_331RAD_N0051812ZCAM08147_1100LMA03.IMG
ZL0_0138_0679192531_331RAD_N0051812ZCAM08147_1100LMA03.IMG
ZL0_0138_0679192544_331RAD_N0051812ZCAM08147_1100LMA03.IMG
ZL0_0138_0679192558_331RAD_N0051812ZCAM08147_1100LMA03.IMG
ZL0_0138_0679192570_331RAD_N0051812ZCAM08147_1100LMA03.IMG
ZL0_0138_0679192582_331RAD_N0051812ZCAM08147_1100LMA03.IMG
ZL0_0138_0679192594_331RAD_N0051812ZCAM08147_1100LMA03.IMG
ZL0_0138_0679192606_331RAD_N0051812ZCAM08147_1100LMA03.IMG
ZL0_0138_0679192618_331RAD_N0051812ZCAM08147_1100LMA03.IMG
ZL0_0138_0679192630_331RAD_N0051812ZCAM08147_1100LMA03.IMG
ZL0_0138_0679192656_331RAD_N0051812ZCAM08147_1100LMA03.IMG
ZL0_0138_0679192688_331RAD_N0051812ZCAM08147_1100LMA03.IMG
ZL0_0138_0679192718_331RAD_N0051812ZCAM08147_1100LMA03.IMG
ZL0_0138_0679192735_331RAD_N0051812ZCAM08147_1100LMA03.IMG
ZL0_0138_0679192747_331RAD_N0051812ZCAM08147_1100LMA03.IMG
ZL0_0138_0679192759_364RAD_N0051812ZCAM08147_1100LMA03.IMG
ZL0_0138_0679192772_331RAD_N0051812ZCAM08147_1100LMA03.IMG
ZL0_0138_0679192784_331RAD_N0051812ZCAM08147_1100LMA03.IMG
ZL0_0138_0679192797_331RAD_N0051812ZCAM08147_1100LMA03.IMG
ZL0_0138_0679192810_331RAD_N0051812ZCAM08147_1100LMA03.IMG
ZL0_0138_0679192838_332RAD_N0051812ZCAM08147_1100LMA03.IMG
ZL0_0138_0679192855_331RAD_N0051812ZCAM08147_1100LMA03.IMG

ZL0_0138_0679192882_332RAD_N0051812ZCAM08147_1100LMA03.IMG
ZL0_0138_0679192899_331RAD_N0051812ZCAM08147_1100LMA03.IMG
ZL0_0138_0679192911_331RAD_N0051812ZCAM08147_1100LMA03.IMG
ZL0_0138_0679192923_331RAD_N0051812ZCAM08147_1100LMA03.IMG
ZL0_0138_0679192937_331RAD_N0051812ZCAM08147_1100LMA03.IMG
ZL0_0138_0679192951_331RAD_N0051812ZCAM08147_1100LMA03.IMG
ZL0_0138_0679192963_331RAD_N0051812ZCAM08147_1100LMA03.IMG
ZL0_0138_0679192975_331RAD_N0051812ZCAM08147_1100LMA03.IMG
ZL0_0138_0679192987_331RAD_N0051812ZCAM08147_1100LMA04.IMG
ZL0_0138_0679192999_331RAD_N0051812ZCAM08147_1100LMA03.IMG

Figure 2B
ZR0_0175_0682469398_495RAD_N0061648ZCAM08188_063085A03.IMG
ZR0_0175_0682469548_523RAD_N0061648ZCAM08188_063085A03.IMG
ZR0_0175_0682469570_488RAD_N0061648ZCAM08188_063085A03.IMG
ZR0_0175_0682469585_488RAD_N0061648ZCAM08188_063085A03.IMG
ZR0_0175_0682469599_488RAD_N0061648ZCAM08188_063085A03.IMG
ZR0_0175_0682469626_488RAD_N0061648ZCAM08188_063085A03.IMG

Figure 2C
ZL0_0288_0692488133_415RAD_N0090000ZCAM08312_1100LMA02.IMG
ZL0_0288_0692488223_410RAD_N0090000ZCAM08312_1100LMA02.IMG
ZL0_0288_0692488243_409RAD_N0090000ZCAM08312_1100LMA02.IMG
ZL0_0288_0692488270_410RAD_N0090000ZCAM08312_1100LMA02.IMG
ZL0_0288_0692488287_409RAD_N0090000ZCAM08312_1100LMA03.IMG
ZL0_0288_0692488301_409RAD_N0090000ZCAM08312_1100LMA03.IMG
ZL0_0288_0692488315_409RAD_N0090000ZCAM08312_1100LMA02.IMG
ZL0_0288_0692488344_410RAD_N0090000ZCAM08312_1100LMA02.IMG
ZL0_0288_0692488361_409RAD_N0090000ZCAM08312_1100LMA02.IMG
ZL0_0288_0692488390_410RAD_N0090000ZCAM08312_1100LMA02.IMG
ZL0_0288_0692488407_409RAD_N0090000ZCAM08312_1100LMA02.IMG
ZL0_0288_0692488419_409RAD_N0090000ZCAM08312_1100LMA02.IMG
ZL0_0288_0692488445_410RAD_N0090000ZCAM08312_1100LMA02.IMG
ZL0_0288_0692488464_409RAD_N0090000ZCAM08312_1100LMA02.IMG
ZL0_0288_0692488493_410RAD_N0090000ZCAM08312_1100LMA02.IMG
ZL0_0288_0692488510_409RAD_N0090000ZCAM08312_1100LMA02.IMG
ZL0_0288_0692488522_409RAD_N0090000ZCAM08312_1100LMA03.IMG
Figure 3A
SI1_0160_0681180536_921ECZ_N0060000SRLC00003_000095J03.IMG
Figure 3B
SC3_0186_0683478369_789ECM_N0070000SRLC11420_0000LUJ04.IMG
SC3_0186_0683478371_539ECM_N0070000SRLC11420_0000LUJ04.IMG
SC3_0186_0683478373_289ECM_N0070000SRLC11420_0000LUJ04.IMG
SC3_0186_0683478375_039ECM_N0070000SRLC11420_0000LUJ04.IMG
SC3_0186_0683478376_789ECM_N0070000SRLC11420_0000LUJ04.IMG
SC3_0186_0683478378_539ECM_N0070000SRLC11420_0000LUJ04.IMG
Colorized using:
SIF_0185_0683368207_957FDR_N0070000SRLC00720_0000LUJ03.IMG
Figure 3C
SC3_0257_0689787001_324ECM_N0080000SRLC10401_0000LUJ03.IMG
SC3_0257_0689787003_148ECM_N0080000SRLC10401_0000LUJ03.IMG
SC3_0257_0689787004_972ECM_N0080000SRLC10401_0000LUJ03.IMG
SC3_0257_0689787006_796ECM_N0080000SRLC10401_0000LUJ03.IMG
SC3_0257_0689787008_621ECM_N0080000SRLC10401_0000LUJ03.IMG
SC3_0257_0689787010_445ECM_N0080000SRLC10401_0000LUJ03.IMG
SC3_0257_0689787012_269ECM_N0080000SRLC10401_0000LUJ03.IMG
SC3_0257_0689787014_093ECM_N0080000SRLC10401_0000LUJ03.IMG

Colorized using:
SIF_0257_0689757397_902FDR_N0080000SRLC00672_0000LMJ03.IMG

Figure 4A
ZR0_0201_0684782666_073RAD_N0071172ZCAM08221_110085A02.IMG
ZR0_0201_0684782715_069RAD_N0071172ZCAM08221_110085A02.IMG
ZR0_0201_0684782736_069RAD_N0071172ZCAM08221_110085A02.IMG
ZR0_0201_0684782748_069RAD_N0071172ZCAM08221_110085A02.IMG
ZR0_0201_0684782760_069RAD_N0071172ZCAM08221_110085A02.IMG
ZR0_0201_0684782773_069RAD_N0071172ZCAM08221_110085A02.IMG
ZR0_0201_0684782785_069RAD_N0071172ZCAM08221_110085A02.IMG
ZR0_0201_0684782797_069RAD_N0071172ZCAM08221_110085A02.IMG
ZR0_0201_0684782823_069RAD_N0071172ZCAM08221_110085A02.IMG
ZR0_0201_0684782840_069RAD_N0071172ZCAM08221_110085A02.IMG
ZR0_0201_0684782852_069RAD_N0071172ZCAM08221_110085A02.IMG
ZR0_0201_0684782879_069RAD_N0071172ZCAM08221_110085A02.IMG
ZR0_0201_0684782896_069RAD_N0071172ZCAM08221_110085A02.IMG
ZR0_0201_0684782922_069RAD_N0071172ZCAM08221_110085A02.IMG
ZR0_0201_0684782941_069RAD_N0071172ZCAM08221_110085A02.IMG
ZR0_0201_0684782955_069RAD_N0071172ZCAM08221_110085A02.IMG
ZR0_0201_0684782967_069RAD_N0071172ZCAM08221_110085A02.IMG
ZR0_0201_0684782980_069RAD_N0071172ZCAM08221_110085A02.IMG
ZR0_0201_0684782994_069RAD_N0071172ZCAM08221_110085A02.IMG
ZR0_0201_0684783008_069RAD_N0071172ZCAM08221_110085A02.IMG
ZR0_0201_0684783022_069RAD_N0071172ZCAM08221_110085A02.IMG
ZR0_0201_0684783047_069RAD_N0071172ZCAM08221_110085A02.IMG
ZR0_0201_0684783066_069RAD_N0071172ZCAM08221_110085A02.IMG
ZR0_0201_0684783078_069RAD_N0071172ZCAM08221_110085A02.IMG
ZR0_0201_0684783092_069RAD_N0071172ZCAM08221_110085A02.IMG
ZR0_0201_0684783106_069RAD_N0071172ZCAM08221_110085A02.IMG
ZR0_0201_0684783121_069RAD_N0071172ZCAM08221_110085A02.IMG
ZR0_0201_0684783134_069RAD_N0071172ZCAM08221_110085A02.IMG
ZR0_0201_0684783146_069RAD_N0071172ZCAM08221_110085A02.IMG
ZR0_0201_0684783173_069RAD_N0071172ZCAM08221_110085A02.IMG

Figure 4B
ZL0_0204_0685052018_216RAD_N0071716ZCAM08228_110085A02.IMG
ZL0_0204_0685052130_206RAD_N0071716ZCAM08228_110085A02.IMG
ZL0_0204_0685052151_223RAD_N0071716ZCAM08228_110085A02.IMG
ZL0_0204_0685052179_206RAD_N0071716ZCAM08228_110085A02.IMG
ZL0_0204_0685052198_206RAD_N0071716ZCAM08228_110085A02.IMG
ZL0_0204_0685052212_206RAD_N0071716ZCAM08228_110085A02.IMG
ZL0_0204_0685052224_206RAD_N0071716ZCAM08228_110085A02.IMG
ZL0_0204_0685052252_206RAD_N0071716ZCAM08228_110085A02.IMG
ZL0_0204_0685052270_206RAD_N0071716ZCAM08228_110085A02.IMG
ZL0_0204_0685052284_206RAD_N0071716ZCAM08228_110085A02.IMG
ZL0_0204_0685052311_206RAD_N0071716ZCAM08228_110085A02.IMG
ZL0_0204_0685052331_206RAD_N0071716ZCAM08228_110085A02.IMG
ZL0_0204_0685052346_206RAD_N0071716ZCAM08228_110085A02.IMG
ZL0_0204_0685052384_206RAD_N0071716ZCAM08228_110085A02.IMG
ZL0_0204_0685052403_206RAD_N0071716ZCAM08228_110085A02.IMG
ZL0_0204_0685052415_206RAD_N0071716ZCAM08228_110085A02.IMG
ZL0_0204_0685052429_206RAD_N0071716ZCAM08228_110085A02.IMG
ZL0_0204_0685052443_206RAD_N0071716ZCAM08228_110085A02.IMG
ZL0_0204_0685052456_223RAD_N0071716ZCAM08228_110085A02.IMG
ZL0_0204_0685052483_206RAD_N0071716ZCAM08228_110085A02.IMG
ZL0_0204_0685052501_206RAD_N0071716ZCAM08228_110085A02.IMG

ZL0_0204_0685052515_206RAD_N0071716ZCAM08228_110085A02.IMG
ZL0_0204_0685052527_223RAD_N0071716ZCAM08228_110085A02.IMG
ZL0_0204_0685052556_206RAD_N0071716ZCAM08228_110085A02.IMG
ZL0_0204_0685052573_206RAD_N0071716ZCAM08228_110085A02.IMG
ZL0_0204_0685052600_206RAD_N0071716ZCAM08228_110085A02.IMG
ZL0_0204_0685052618_239RAD_N0071716ZCAM08228_110085A02.IMG
ZL0_0204_0685052630_206RAD_N0071716ZCAM08228_110085A02.IMG
ZL0_0204_0685052642_206RAD_N0071716ZCAM08228_110085A02.IMG
ZL0_0204_0685052654_223RAD_N0071716ZCAM08228_110085A02.IMG
ZL0_0204_0685052685_206RAD_N0071716ZCAM08228_110085A02.IMG
ZL0_0204_0685052718_207RAD_N0071716ZCAM08228_110085A02.IMG
ZL0_0204_0685052735_206RAD_N0071716ZCAM08228_110085A02.IMG
ZL0_0204_0685052747_206RAD_N0071716ZCAM08228_110085A02.IMG
ZL0_0204_0685052775_206RAD_N0071716ZCAM08228_110085A02.IMG
ZL0_0204_0685052792_206RAD_N0071716ZCAM08228_110085A02.IMG
ZL0_0204_0685052806_206RAD_N0071716ZCAM08228_110085A02.IMG
ZL0_0204_0685052821_206RAD_N0071716ZCAM08228_110085A02.IMG
ZL0_0204_0685052835_206RAD_N0071716ZCAM08228_110085A02.IMG
ZL0_0204_0685052863_206RAD_N0071716ZCAM08228_110085A02.IMG
ZL0_0204_0685052881_206RAD_N0071716ZCAM08228_110085A02.IMG
ZL0_0204_0685052908_206RAD_N0071716ZCAM08228_110085A02.IMG
ZL0_0204_0685052925_206RAD_N0071716ZCAM08228_110085A02.IMG
ZL0_0204_0685052937_206RAD_N0071716ZCAM08228_110085A02.IMG
ZL0_0204_0685052951_223RAD_N0071716ZCAM08228_110085A02.IMG
ZL0_0204_0685052986_223RAD_N0071716ZCAM08228_110085A02.IMG
ZL0_0204_0685053003_206RAD_N0071716ZCAM08228_110085A02.IMG
ZL0_0204_0685053017_206RAD_N0071716ZCAM08228_110085A02.IMG
ZL0_0204_0685053029_206RAD_N0071716ZCAM08228_110085A02.IMG
ZL0_0204_0685053041_206RAD_N0071716ZCAM08228_110085A02.IMG
ZL0_0204_0685053053_206RAD_N0071716ZCAM08228_110085A02.IMG
ZL0_0204_0685053080_206RAD_N0071716ZCAM08228_110085A02.IMG
ZL0_0204_0685053097_206RAD_N0071716ZCAM08228_110085A02.IMG
ZL0_0204_0685053109_206RAD_N0071716ZCAM08228_110085A02.IMG
ZL0_0204_0685053136_206RAD_N0071716ZCAM08228_110085A02.IMG
ZL0_0204_0685053153_206RAD_N0071716ZCAM08228_110085A02.IMG

Figure 4C
LRE_0206_0685219280_352ECM_N0071836SCAM01206_0010I6J02.IMG
LRE_0206_0685220408_265ECM_N0071836SCAM01206_0050I6J02.IMG

Figure 5 PIXL PDS data bundle (*75*), Processed data collection. Guillaumes and Dourbes abrasion patch data are listed under sols 167 and 269, respectively.

Figure 7A
ZL0_0180_0682918130_087RAD_N0062666ZCAM08195_110085A02.IMG
ZL0_0180_0682918181_081RAD_N0062666ZCAM08195_110085A02.IMG
ZL0_0180_0682918198_081RAD_N0062666ZCAM08195_110085A02.IMG
ZL0_0180_0682918211_081RAD_N0062666ZCAM08195_110085A02.IMG
ZL0_0180_0682918225_081RAD_N0062666ZCAM08195_110085A02.IMG
ZL0_0180_0682918237_081RAD_N0062666ZCAM08195_110085A02.IMG
ZL0_0180_0682918264_081RAD_N0062666ZCAM08195_110085A02.IMG
ZL0_0180_0682918281_081RAD_N0062666ZCAM08195_110085A02.IMG
ZL0_0180_0682918307_081RAD_N0062666ZCAM08195_110085A02.IMG
ZL0_0180_0682918327_081RAD_N0062666ZCAM08195_110085A02.IMG
ZL0_0180_0682918339_081RAD_N0062666ZCAM08195_110085A02.IMG
ZL0_0180_0682918365_081RAD_N0062666ZCAM08195_110085A02.IMG
ZL0_0180_0682918384_081RAD_N0062666ZCAM08195_110085A02.IMG

ZL0_0180_0682918403_081RAD_N0062666ZCAM08195_110085A02.IMG
ZL0_0180_0682918432_081RAD_N0062666ZCAM08195_110085A02.IMG
ZL0_0180_0682918468_081RAD_N0062666ZCAM08195_110085A02.IMG
ZL0_0180_0682918486_081RAD_N0062666ZCAM08195_110085A02.IMG
ZL0_0180_0682918499_081RAD_N0062666ZCAM08195_110085A02.IMG
ZL0_0180_0682918511_113RAD_N0062666ZCAM08195_110085A02.IMG
ZL0_0180_0682918524_081RAD_N0062666ZCAM08195_110085A02.IMG
ZL0_0180_0682918537_081RAD_N0062666ZCAM08195_110085A02.IMG
ZL0_0180_0682918567_081RAD_N0062666ZCAM08195_110085A02.IMG
ZL0_0180_0682918584_114RAD_N0062666ZCAM08195_110085A02.IMG
ZL0_0180_0682918597_081RAD_N0062666ZCAM08195_110085A02.IMG
ZL0_0180_0682918611_113RAD_N0062666ZCAM08195_110085A02.IMG
ZL0_0180_0682918639_081RAD_N0062666ZCAM08195_110085A02.IMG
ZL0_0180_0682918656_081RAD_N0062666ZCAM08195_110085A02.IMG
ZL0_0180_0682918669_081RAD_N0062666ZCAM08195_110085A02.IMG
ZL0_0180_0682918682_081RAD_N0062666ZCAM08195_110085A02.IMG
ZL0_0180_0682918695_081RAD_N0062666ZCAM08195_110085A02.IMG
ZL0_0180_0682918708_081RAD_N0062666ZCAM08195_110085A02.IMG
ZL0_0180_0682918722_081RAD_N0062666ZCAM08195_110085A02.IMG
ZL0_0180_0682918748_081RAD_N0062666ZCAM08195_110085A02.IMG
ZL0_0180_0682918767_081RAD_N0062666ZCAM08195_110085A02.IMG
ZL0_0180_0682918780_081RAD_N0062666ZCAM08195_110085A02.IMG
ZL0_0180_0682918793_081RAD_N0062666ZCAM08195_110085A02.IMG
ZL0_0180_0682918822_081RAD_N0062666ZCAM08195_110085A02.IMG
ZL0_0180_0682918839_081RAD_N0062666ZCAM08195_110085A02.IMG
ZL0_0180_0682918852_081RAD_N0062666ZCAM08195_110085A02.IMG

Figure 7B
NLE_0190_0683808498_362ECM_N0070000NCAM00705_01_0LLJ02.IMG
NLE_0190_0683808498_362ECM_N0070000NCAM00705_02_0LLJ02.IMG
NLE_0190_0683808498_362ECM_N0070000NCAM00705_03_0LLJ02.IMG
NLE_0190_0683808498_362ECM_N0070000NCAM00705_04_0LLJ02.IMG
Figure 7C
CCF_0194_0684174847_162ECM_N0070000CACH00105_01_295J02.IMG
CCF_0194_0684174877_427ECM_N0070000CACH00105_01_295J02.IMG
CCF_0194_0684174914_897ECM_N0070000CACH00105_01_295J02.IMG
CCF_0194_0684174952_699ECM_N0070000CACH00105_01_295J02.IMG
CCF_0194_0684175132_073ECM_N0070000CACH00105_01_295J02.IMG
CCF_0194_0684175175_443ECM_N0070000CACH00105_01_295J02.IMG
CCF_0194_0684175213_381ECM_N0070000CACH00106_01_295J02.IMG
CCF_0194_0684175254_729ECM_N0070000CACH00106_01_295J02.IMG
CCF_0194_0684175288_395ECM_N0070000CACH00106_01_295J02.IMG
CCF_0194_0684175338_287ECM_N0070000CACH00106_01_295J02.IMG
CCF_0194_0684175380_037ECM_N0070000CACH00106_01_295J02.IMG
CCF_0194_0684175410_488ECM_N0070000CACH00106_01_295J02.IMG
CCF_0194_0684176479_117ECM_N0070000CACH00105_01_295J02.IMG
CCF_0194_0684176514_115ECM_N0070000CACH00105_01_295J02.IMG
CCF_0194_0684176583_320ECM_N0070000CACH00105_01_295J02.IMG
CCF_0194_0684176622_856ECM_N0070000CACH00105_01_295J02.IMG
CCF_0194_0684176662_991ECM_N0070000CACH00106_01_295J02.IMG
CCF_0194_0684177386_804ECM_N0070000CACH00200_01_295J02.IMG
CCF_0194_0684179248_776ECM_N0070000CACH00200_01_295J02.IMG
Figure 7D
ZL0_0240_0688257476_667RAD_N0072440ZCAM08264_110085A02.IMG
ZL0_0240_0688257556_660RAD_N0072440ZCAM08264_110085A02.IMG
ZL0_0240_0688257579_659RAD_N0072440ZCAM08264_110085A02.IMG
ZL0_0240_0688257612_660RAD_N0072440ZCAM08264_110085A02.IMG

ZL0_0240_0688257647_693RAD_N0072440ZCAM08264_110085A02.IMG
ZL0_0240_0688257666_693RAD_N0072440ZCAM08264_110085A02.IMG
ZL0_0240_0688257701_660RAD_N0072440ZCAM08264_110085A02.IMG
ZL0_0240_0688257738_660RAD_N0072440ZCAM08264_110085A02.IMG
ZL0_0240_0688257758_660RAD_N0072440ZCAM08264_110085A02.IMG
ZL0_0240_0688257791_660RAD_N0072440ZCAM08264_110085A02.IMG
ZL0_0240_0688257826_660RAD_N0072440ZCAM08264_110085A02.IMG
ZL0_0240_0688257863_660RAD_N0072440ZCAM08264_110085A02.IMG
ZL0_0240_0688257882_659RAD_N0072440ZCAM08264_110085A02.IMG
ZL0_0240_0688257915_660RAD_N0072440ZCAM08264_110085A02.IMG
ZL0_0240_0688257956_660RAD_N0072440ZCAM08264_110085A02.IMG
ZL0_0240_0688257998_660RAD_N0072440ZCAM08264_110085A02.IMG
ZL0_0240_0688258037_660RAD_N0072440ZCAM08264_110085A02.IMG
ZL0_0240_0688258056_659RAD_N0072440ZCAM08264_110085A02.IMG
ZL0_0240_0688258085_660RAD_N0072440ZCAM08264_110085A02.IMG
ZL0_0240_0688258121_660RAD_N0072440ZCAM08264_110085A02.IMG
ZL0_0240_0688258141_660RAD_N0072440ZCAM08264_110085A02.IMG
ZL0_0240_0688258157_660RAD_N0072440ZCAM08264_110085A02.IMG
ZL0_0240_0688258174_660RAD_N0072440ZCAM08264_110085A02.IMG
ZL0_0240_0688258192_660RAD_N0072440ZCAM08264_110085A02.IMG
ZL0_0240_0688258208_660RAD_N0072440ZCAM08264_110085A02.IMG
ZL0_0240_0688258225_660RAD_N0072440ZCAM08264_110085A02.IMG
ZL0_0240_0688258259_660RAD_N0072440ZCAM08264_110085A02.IMG
ZL0_0240_0688258296_660RAD_N0072440ZCAM08264_110085A02.IMG
ZL0_0240_0688258316_693RAD_N0072440ZCAM08264_110085A02.IMG
ZL0_0240_0688258347_660RAD_N0072440ZCAM08264_110085A02.IMG
ZL0_0240_0688258368_660RAD_N0072440ZCAM08264_110085A02.IMG
ZL0_0240_0688258397_660RAD_N0072440ZCAM08264_110085A02.IMG
ZL0_0240_0688258416_659RAD_N0072440ZCAM08264_110085A02.IMG
ZL0_0240_0688258444_660RAD_N0072440ZCAM08264_110085A02.IMG
ZL0_0240_0688258464_660RAD_N0072440ZCAM08264_110085A02.IMG
ZL0_0240_0688258480_660RAD_N0072440ZCAM08264_110085A02.IMG
ZL0_0240_0688258514_660RAD_N0072440ZCAM08264_110085A02.IMG
ZL0_0240_0688258535_660RAD_N0072440ZCAM08264_110085A02.IMG
ZL0_0240_0688258569_660RAD_N0072440ZCAM08264_110085A02.IMG
ZL0_0240_0688258590_660RAD_N0072440ZCAM08264_110085A02.IMG
ZL0_0240_0688258611_660RAD_N0072440ZCAM08264_110085A02.IMG
ZL0_0240_0688258642_660RAD_N0072440ZCAM08264_110085A02.IMG
ZL0_0240_0688258677_660RAD_N0072440ZCAM08264_110085A02.IMG
ZL0_0240_0688258699_660RAD_N0072440ZCAM08264_110085A02.IMG
ZL0_0240_0688258717_660RAD_N0072440ZCAM08264_110085A02.IMG
ZL0_0240_0688258750_660RAD_N0072440ZCAM08264_110085A02.IMG
ZL0_0240_0688258785_660RAD_N0072440ZCAM08264_110085A02.IMG
ZL0_0240_0688258805_660RAD_N0072440ZCAM08264_110085A02.IMG
ZL0_0240_0688258821_660RAD_N0072440ZCAM08264_110085A02.IMG
ZL0_0240_0688258851_660RAD_N0072440ZCAM08264_110085A02.IMG
ZL0_0240_0688258870_693RAD_N0072440ZCAM08264_110085A02.IMG
ZL0_0240_0688258899_660RAD_N0072440ZCAM08264_110085A02.IMG
ZL0_0240_0688258936_660RAD_N0072440ZCAM08264_110085A02.IMG
ZL0_0240_0688258957_660RAD_N0072440ZCAM08264_110085A02.IMG
ZL0_0240_0688258971_659RAD_N0072440ZCAM08264_110085A02.IMG
ZL0_0240_0688259000_660RAD_N0072440ZCAM08264_110085A02.IMG
ZL0_0240_0688259033_660RAD_N0072440ZCAM08264_110085A02.IMG
ZL0_0240_0688259053_660RAD_N0072440ZCAM08264_110085A02.IMG
ZL0_0240_0688259069_659RAD_N0072440ZCAM08264_110085A02.IMG
ZL0_0240_0688259087_660RAD_N0072440ZCAM08264_110085A02.IMG
ZL0_0240_0688259118_660RAD_N0072440ZCAM08264_110085A02.IMG

ZL0_0240_0688259152_660RAD_N0072440ZCAM08264_110085A02.IMG
ZL0_0240_0688259186_660RAD_N0072440ZCAM08264_110085A02.IMG
ZL0_0240_0688259220_660RAD_N0072440ZCAM08264_110085A02.IMG
ZL0_0240_0688259241_693RAD_N0072440ZCAM08264_110085A02.IMG
ZL0_0240_0688259259_660RAD_N0072440ZCAM08264_110085A02.IMG
ZL0_0240_0688259290_660RAD_N0072440ZCAM08264_110085A02.IMG
ZL0_0240_0688259325_660RAD_N0072440ZCAM08264_110085A02.IMG
ZL0_0240_0688259345_660RAD_N0072440ZCAM08264_110085A02.IMG
ZL0_0240_0688259363_660RAD_N0072440ZCAM08264_110085A02.IMG
ZL0_0240_0688259393_660RAD_N0072440ZCAM08264_110085A02.IMG
ZL0_0240_0688259415_660RAD_N0072440ZCAM08264_110085A02.IMG
ZL0_0240_0688259451_660RAD_N0072440ZCAM08264_110085A02.IMG
ZL0_0240_0688259469_659RAD_N0072440ZCAM08264_110085A02.IMG
ZL0_0240_0688259482_659RAD_N0072440ZCAM08264_110085A02.IMG
ZL0_0240_0688259512_660RAD_N0072440ZCAM08264_110085A02.IMG

Figure 7E

FLE_0263_0690291288_693ECM_N0080000FHAZ02008_01_0LLJ02.IMG
FLE_0263_0690291288_693ECM_N0080000FHAZ02008_02_0LLJ02.IMG
FLE_0263_0690291288_693ECM_N0080000FHAZ02008_03_0LLJ02.IMG
FLE_0263_0690291288_693ECM_N0080000FHAZ02008_04_0LLJ02.IMG
FLE_0263_0690291288_693ECM_N0080000FHAZ02008_05_0LLJ02.IMG
FLE_0263_0690291288_693ECM_N0080000FHAZ02008_06_0LLJ02.IMG
FLE_0263_0690291288_693ECM_N0080000FHAZ02008_07_0LLJ02.IMG
FLE_0263_0690291288_693ECM_N0080000FHAZ02008_08_0LLJ02.IMG
FLE_0263_0690291288_693ECM_N0080000FHAZ02008_09_0LLJ02.IMG
FLE_0263_0690291288_693ECM_N0080000FHAZ02008_10_0LLJ02.IMG
FLE_0263_0690291288_693ECM_N0080000FHAZ02008_11_0LLJ02.IMG
FLE_0263_0690291288_693ECM_N0080000FHAZ02008_12_0LLJ02.IMG

Figure 7F

CCE_0262_0690225931_534ECM_N0080000CACH00105_00_0LLJ02.IMG
CCE_0262_0690225940_740ECM_N0080000CACH00105_00_0LLJ02.IMG
CCE_0262_0690225954_013ECM_N0080000CACH00105_00_0LLJ02.IMG
CCE_0262_0690225962_693ECM_N0080000CACH00105_00_0LLJ02.IMG
CCE_0262_0690225967_534ECM_N0080000CACH00105_00_0LLJ02.IMG
CCE_0262_0690225976_793ECM_N0080000CACH00105_00_0LLJ02.IMG
CCE_0262_0690226016_863ECM_N0080000CACH00105_00_0LLJ02.IMG
CCE_0262_0690226021_862ECM_N0080000CACH00105_00_0LLJ02.IMG
CCE_0262_0690226031_021ECM_N0080000CACH00105_00_0LLJ02.IMG
CCE_0262_0690226040_053ECM_N0080000CACH00105_00_0LLJ02.IMG
CCE_0262_0690226045_050ECM_N0080000CACH00105_00_0LLJ02.IMG
CCE_0262_0690226049_896ECM_N0080000CACH00105_00_0LLJ02.IMG
CCE_0262_0690226107_847ECM_N0080000CACH00105_00_0LLJ02.IMG
CCE_0262_0690226112_899ECM_N0080000CACH00105_00_0LLJ02.IMG
CCE_0262_0690226122_288ECM_N0080000CACH00105_00_0LLJ02.IMG
CCE_0262_0690226131_038ECM_N0080000CACH00105_00_0LLJ02.IMG
CCE_0262_0690226140_098ECM_N0080000CACH00105_00_0LLJ02.IMG
CCE_0262_0690226144_987ECM_N0080000CACH00105_00_0LLJ02.IMG
CCE_0262_0690226189_862ECM_N0080000CACH00105_00_0LLJ02.IMG
CCE_0262_0690226194_862ECM_N0080000CACH00105_00_0LLJ02.IMG
CCE_0262_0690226199_862ECM_N0080000CACH00105_00_0LLJ04.IMG
CCE_0262_0690226209_019ECM_N0080000CACH00105_00_0LLJ03.IMG
CCE_0262_0690226218_052ECM_N0080000CACH00105_00_0LLJ03.IMG
CCE_0262_0690226222_862ECM_N0080000CACH00105_00_0LLJ03.IMG
CCE_0262_0690226272_102ECM_N0080000CACH00105_00_0LLJ03.IMG
CCE_0262_0690226276_909ECM_N0080000CACH00105_00_0LLJ03.IMG
CCE_0262_0690226281_997ECM_N0080000CACH00105_00_0LLJ04.IMG
CCE_0262_0690226291_132ECM_N0080000CACH00105_00_0LLJ02.IMG

CCE_0262_0690226300_099ECM_N0080000CACH00105_00_0LLJ02.IMG
CCE_0262_0690226305_488ECM_N0080000CACH00105_00_0LLJ02.IMG
CCF_0262_0690224439_974ECM_N0080000CACH00105_01_295J02.IMG
CCF_0262_0690224474_869ECM_N0080000CACH00105_01_295J02.IMG
CCF_0262_0690224511_897ECM_N0080000CACH00105_01_295J02.IMG
CCF_0262_0690224550_120ECM_N0080000CACH00105_01_295J02.IMG
CCF_0262_0690224588_116ECM_N0080000CACH00105_01_295J02.IMG
CCF_0262_0690224626_269ECM_N0080000CACH00105_01_295J02.IMG
CCF_0262_0690224664_246ECM_N0080000CACH00106_01_295J02.IMG
CCF_0262_0690224698_238ECM_N0080000CACH00106_01_295J02.IMG
CCF_0262_0690224732_300ECM_N0080000CACH00106_01_295J02.IMG
CCF_0262_0690224786_635ECM_N0080000CACH00106_01_295J02.IMG
CCF_0262_0690224826_352ECM_N0080000CACH00106_01_295J02.IMG
CCF_0262_0690224860_364ECM_N0080000CACH00106_01_295J02.IMG
CCF_0262_0690225916_901ECM_N0080000CACH00105_01_295J02.IMG
CCF_0262_0690226001_990ECM_N0080000CACH00105_01_295J02.IMG
CCF_0262_0690226092_917ECM_N0080000CACH00105_01_295J02.IMG
CCF_0262_0690226174_948ECM_N0080000CACH00105_01_295J02.IMG
CCF_0262_0690226253_223ECM_N0080000CACH00105_01_295J02.IMG
CCF_0262_0690226998_168ECM_N0080000CACH00200_01_295J02.IMG
CCF_0262_0690228858_395ECM_N0080000CACH00200_01_295J02.IMG

Figure S1A
ZL0_0078_0673871034_046RAD_N0032430ZCAM08041_110085A03.IMG
ZL0_0078_0673871091_035RAD_N0032430ZCAM08041_110085A03.IMG
ZL0_0078_0673871108_053RAD_N0032430ZCAM08041_110085A03.IMG
ZL0_0078_0673871120_034RAD_N0032430ZCAM08041_110085A03.IMG
ZL0_0078_0673871132_035RAD_N0032430ZCAM08041_110085A03.IMG
ZL0_0078_0673871144_053RAD_N0032430ZCAM08041_110085A03.IMG
ZL0_0078_0673871171_053RAD_N0032430ZCAM08041_110085A03.IMG
ZL0_0078_0673871188_035RAD_N0032430ZCAM08041_110085A03.IMG
ZL0_0078_0673871217_035RAD_N0032430ZCAM08041_110085A03.IMG
ZL0_0078_0673871234_053RAD_N0032430ZCAM08041_110085A03.IMG
ZL0_0078_0673871246_081RAD_N0032430ZCAM08041_110085A03.IMG
ZL0_0078_0673871259_054RAD_N0032430ZCAM08041_110085A03.IMG
ZL0_0078_0673871271_034RAD_N0032430ZCAM08041_110085A03.IMG
ZL0_0078_0673871298_053RAD_N0032430ZCAM08041_110085A03.IMG
Figure S1B
NLF_0066_0672808655_353ECM_N0032208NCAM03066_01_295J03.IMG
NLF_0066_0672808703_559ECM_N0032208NCAM03066_01_295J03.IMG
NLF_0066_0672808703_559ECM_N0032208NCAM03066_04_195J03.IMG
NLF_0066_0672808703_559ECM_N0032208NCAM03066_07_195J03.IMG
NLF_0066_0672808703_559ECM_N0032208NCAM03066_10_195J03.IMG
NLF_0066_0672808703_559ECM_N0032208NCAM03066_13_195J03.IMG
NLF_0066_0672808904_803ECM_N0032208NCAM03066_01_295J03.IMG
NLF_0066_0672809359_976ECM_N0032208NCAM00303_01_195J03.IMG
NLF_0066_0672809359_976ECM_N0032208NCAM00303_04_195J03.IMG
NLF_0066_0672809359_976ECM_N0032208NCAM00303_07_195J03.IMG
NLF_0066_0672809359_976ECM_N0032208NCAM00303_10_195J03.IMG
Figure S1C
ZL0_0003_0667218571_000RAD_N0010052AUT_04096_034085A03.IMG
ZL0_0003_0667218023_000RAD_N0010052AUT_04096_034085A03.IMG
Figure S1D, E, F
ZL0_0168_0681868155_149RAD_N0060170ZCAM08180_048085A04.IMG
ZL0_0168_0681868268_144RAD_N0060170ZCAM08180_048085A04.IMG
ZL0_0168_0681868313_145RAD_N0060170ZCAM08180_048085A04.IMG
ZL0_0168_0681868358_144RAD_N0060170ZCAM08180_048085A04.IMG

ZL0_0168_0681868401_144RAD_N0060170ZCAM08180_048085A04.IMG
ZL0_0168_0681868442_144RAD_N0060170ZCAM08180_048085A04.IMG
ZL0_0168_0681868480_144RAD_N0060170ZCAM08180_048085A04.IMG
ZL0_0168_0681868514_144RAD_N0060170ZCAM08180_048085A04.IMG
ZL0_0168_0681868548_146RAD_N0060170ZCAM08180_048085A04.IMG
ZL0_0168_0681868581_144RAD_N0060170ZCAM08180_048085A04.IMG
ZL0_0168_0681868621_144RAD_N0060170ZCAM08180_048085A04.IMG
ZL0_0168_0681868660_144RAD_N0060170ZCAM08180_048085A04.IMG
ZL0_0168_0681868698_148RAD_N0060170ZCAM08180_048085A04.IMG
ZL0_0168_0681868734_144RAD_N0060170ZCAM08180_048085A04.IMG
ZL0_0168_0681868755_145RAD_N0060170ZCAM08180_048085A04.IMG
ZL0_0168_0681868786_144RAD_N0060170ZCAM08180_048085A04.IMG
ZL0_0168_0681868805_144RAD_N0060170ZCAM08180_048085A04.IMG
ZL0_0168_0681868841_144RAD_N0060170ZCAM08180_048085A04.IMG
ZL0_0168_0681868860_146RAD_N0060170ZCAM08180_048085A04.IMG
ZL0_0168_0681868874_144RAD_N0060170ZCAM08180_048085A04.IMG
ZL0_0168_0681868888_144RAD_N0060170ZCAM08180_048085A04.IMG
ZL0_0168_0681868921_144RAD_N0060170ZCAM08180_048085A04.IMG
ZL0_0168_0681868958_144RAD_N0060170ZCAM08180_048085A04.IMG
ZL0_0168_0681868994_144RAD_N0060170ZCAM08180_048085A04.IMG
ZL0_0168_0681869032_144RAD_N0060170ZCAM08180_048085A04.IMG
ZL0_0168_0681869050_144RAD_N0060170ZCAM08180_048085A04.IMG

Figure S2A
ZL0_0238_0688068238_650RAD_N0072246ZCAM08261_110085A02.IMG
ZL0_0238_0688068358_644RAD_N0072246ZCAM08261_1100LMA03.IMG
ZL0_0238_0688068390_649RAD_N0072246ZCAM08261_1100LMA03.IMG
ZL0_0238_0688068407_644RAD_N0072246ZCAM08261_110085A02.IMG
ZL0_0238_0688068419_644RAD_N0072246ZCAM08261_110085A02.IMG
ZL0_0238_0688068431_644RAD_N0072246ZCAM08261_1100LMA03.IMG
ZL0_0238_0688068455_645RAD_N0072246ZCAM08261_1100LMA03.IMG
ZL0_0238_0688068468_644RAD_N0072246ZCAM08261_110085A02.IMG
ZL0_0238_0688068480_644RAD_N0072246ZCAM08261_110085A02.IMG
ZL0_0238_0688068492_644RAD_N0072246ZCAM08261_1100LMA03.IMG
ZL0_0238_0688068519_644RAD_N0072246ZCAM08261_1100LMA03.IMG
ZL0_0238_0688068536_644RAD_N0072246ZCAM08261_1100LMA03.IMG
ZL0_0238_0688068566_649RAD_N0072246ZCAM08261_1100LMA03.IMG
ZL0_0238_0688068583_646RAD_N0072246ZCAM08261_110085A02.IMG
ZL0_0238_0688068595_644RAD_N0072246ZCAM08261_110085A02.IMG
ZL0_0238_0688068622_644RAD_N0072246ZCAM08261_1100LMA03.IMG
ZL0_0238_0688068639_646RAD_N0072246ZCAM08261_1100LMA03.IMG
ZL0_0238_0688068669_644RAD_N0072246ZCAM08261_1100LMA03.IMG
ZL0_0238_0688068687_646RAD_N0072246ZCAM08261_110085A02.IMG
ZL0_0238_0688068700_678RAD_N0072246ZCAM08261_110085A02.IMG
ZL0_0238_0688068726_644RAD_N0072246ZCAM08261_110085A02.IMG
ZL0_0238_0688068757_644RAD_N0072246ZCAM08261_110085A02.IMG
ZL0_0238_0688068776_646RAD_N0072246ZCAM08261_110085A02.IMG
ZL0_0238_0688068790_644RAD_N0072246ZCAM08261_110085A02.IMG
ZL0_0238_0688068804_644RAD_N0072246ZCAM08261_110085A02.IMG
ZL0_0238_0688068816_649RAD_N0072246ZCAM08261_1100LMA03.IMG
ZL0_0238_0688068842_644RAD_N0072246ZCAM08261_1100LMA03.IMG
ZL0_0238_0688068873_648RAD_N0072246ZCAM08261_110085A02.IMG
Figure S2B
ZL0_0211_0685688063_091RAD_N0072050ZCAM08246_1100LMA02.IMG
ZL0_0211_0685688169_081RAD_N0072050ZCAM08246_1100LMA02.IMG
ZL0_0211_0685688187_081RAD_N0072050ZCAM08246_1100LMA02.IMG
ZL0_0211_0685688214_081RAD_N0072050ZCAM08246_1100LMA02.IMG

ZL0_0211_0685688247_081RAD_N0072050ZCAM08246_1100LMA02.IMG
ZL0_0211_0685688264_081RAD_N0072050ZCAM08246_1100LMA02.IMG
ZL0_0211_0685688290_081RAD_N0072050ZCAM08246_1100LMA02.IMG
ZL0_0211_0685688307_081RAD_N0072050ZCAM08246_1100LMA02.IMG
ZL0_0211_0685688319_081RAD_N0072050ZCAM08246_1100LMA02.IMG
ZL0_0211_0685688350_098RAD_N0072050ZCAM08246_1100LMA02.IMG

Figure S2C, D

ZL0_0205_0685142514_874RAD_N0071836ZCAM08231_1100LMA02.IMG
ZL0_0205_0685142570_889RAD_N0071836ZCAM08231_1100LMA02.IMG
ZL0_0205_0685142589_864RAD_N0071836ZCAM08231_1100LMA02.IMG
ZL0_0205_0685142602_889RAD_N0071836ZCAM08231_1100LMA02.IMG
ZL0_0205_0685142614_889RAD_N0071836ZCAM08231_1100LMA02.IMG
ZL0_0205_0685142626_889RAD_N0071836ZCAM08231_1100LMA02.IMG
ZL0_0205_0685142652_864RAD_N0071836ZCAM08231_1100LMA02.IMG
ZL0_0205_0685142683_889RAD_N0071836ZCAM08231_1100LMA02.IMG
ZL0_0205_0685142715_894RAD_N0071836ZCAM08231_1100LMA02.IMG
ZL0_0205_0685142745_898RAD_N0071836ZCAM08231_1100LMA02.IMG
ZL0_0205_0685142777_896RAD_N0071836ZCAM08231_1100LMA02.IMG
ZL0_0205_0685142808_864RAD_N0071836ZCAM08231_1100LMA02.IMG
ZL0_0205_0685142827_864RAD_N0071836ZCAM08231_1100LMA02.IMG
ZL0_0205_0685142854_888RAD_N0071836ZCAM08231_1100LMA02.IMG
ZL0_0205_0685142871_864RAD_N0071836ZCAM08231_1100LMA02.IMG
ZL0_0205_0685142886_889RAD_N0071836ZCAM08231_1100LMA02.IMG
ZL0_0205_0685142912_889RAD_N0071836ZCAM08231_1100LMA02.IMG

Figure S3A

ZL0_0202_0684869633_091RAD_N0071358ZCAM08224_1100LMA02.IMG
ZL0_0202_0684869662_098RAD_N0071358ZCAM08224_1100LMA02.IMG
ZL0_0202_0684869675_081RAD_N0071358ZCAM08224_1100LMA02.IMG
ZL0_0202_0684869687_081RAD_N0071358ZCAM08224_1100LMA02.IMG
ZL0_0202_0684869699_081RAD_N0071358ZCAM08224_1100LMA02.IMG
ZL0_0202_0684869726_081RAD_N0071358ZCAM08224_1100LMA02.IMG
ZL0_0202_0684869743_081RAD_N0071358ZCAM08224_1100LMA02.IMG
ZL0_0202_0684869756_081RAD_N0071358ZCAM08224_1100LMA02.IMG

Figure S3C RIMFAX PDS data bundle (*76*), Calibrated data collection, sols 201 and 202.

Figure S4A

ZL0_0162_0681324362_749IOF_N0060000ZCAM03197_1100LMA03.IMG
ZL0_0162_0681324559_774IOF_N0060000ZCAM03197_1100LMA06.IMG
ZL1_0162_0681324515_771IOF_N0060000ZCAM03197_1100LMA03.IMG
ZL1_0162_0681324588_763IOF_N0060000ZCAM03197_1100LMA03.IMG
ZL2_0162_0681324520_738IOF_N0060000ZCAM03197_1100LMA03.IMG
ZL2_0162_0681324595_764IOF_N0060000ZCAM03197_1100LMA03.IMG
ZL3_0162_0681324526_761IOF_N0060000ZCAM03197_1100LMA03.IMG
ZL3_0162_0681324602_764IOF_N0060000ZCAM03197_1100LMA03.IMG
ZL4_0162_0681324532_785IOF_N0060000ZCAM03197_1100LMA03.IMG
ZL4_0162_0681324609_738IOF_N0060000ZCAM03197_1100LMA03.IMG
ZL5_0162_0681324539_772IOF_N0060000ZCAM03197_1100LMA03.IMG
ZL5_0162_0681324616_765IOF_N0060000ZCAM03197_1100LMA03.IMG
ZL6_0162_0681324549_738IOF_N0060000ZCAM03197_1100LMA03.IMG
ZL6_0162_0681324623_738IOF_N0060000ZCAM03197_1100LMA03.IMG
ZR0_0162_0681324362_749IOF_N0060000ZCAM03197_1100LMA03.IMG
ZR0_0162_0681324630_764IOF_N0060000ZCAM03197_1100LMA04.IMG
ZR1_0162_0681324515_771IOF_N0060000ZCAM03197_1100LMA03.IMG
ZR1_0162_0681324659_770IOF_N0060000ZCAM03197_1100LMA03.IMG

ZR2_0162_0681324520_738IOF_N0060000ZCAM03197_1100LMA03.IMG
ZR2_0162_0681324667_764IOF_N0060000ZCAM03197_1100LMA03.IMG
ZR3_0162_0681324526_761IOF_N0060000ZCAM03197_1100LMA03.IMG
ZR3_0162_0681324674_770IOF_N0060000ZCAM03197_1100LMA03.IMG
ZR4_0162_0681324532_785IOF_N0060000ZCAM03197_1100LMA03.IMG
ZR4_0162_0681324681_771IOF_N0060000ZCAM03197_1100LMA03.IMG
ZR5_0162_0681324539_772IOF_N0060000ZCAM03197_1100LMA03.IMG
ZR5_0162_0681324689_773IOF_N0060000ZCAM03197_1100LMA03.IMG
ZR6_0162_0681324549_738IOF_N0060000ZCAM03197_1100LMA03.IMG
ZR6_0162_0681324698_771IOF_N0060000ZCAM03197_1100LMA03.IMG
ZL0_0123_0677860755_718IOF_N0041422ZCAM03169_1100LMA03.IMG
ZL1_0123_0677860813_707IOF_N0041422ZCAM03169_1100LMA03.IMG
ZL2_0123_0677860826_724IOF_N0041422ZCAM03169_1100LMA03.IMG
ZL3_0123_0677860838_723IOF_N0041422ZCAM03169_1100LMA03.IMG
ZL4_0123_0677860850_723IOF_N0041422ZCAM03169_1100LMA03.IMG
ZL5_0123_0677860863_707IOF_N0041422ZCAM03169_1100LMA03.IMG
ZL6_0123_0677860875_723IOF_N0041422ZCAM03169_1100LMA03.IMG
ZR0_0123_0677860887_723IOF_N0041422ZCAM03169_1100LMA03.IMG
ZR1_0123_0677860928_724IOF_N0041422ZCAM03169_1100LMA05.IMG
ZR2_0123_0677860941_723IOF_N0041422ZCAM03169_1100LMA03.IMG
ZR3_0123_0677860956_724IOF_N0041422ZCAM03169_1100LMA03.IMG
ZR4_0123_0677860972_724IOF_N0041422ZCAM03169_1100LMA03.IMG
ZR5_0123_0677860988_707IOF_N0041422ZCAM03169_1100LMA03.IMG
ZR6_0123_0677861006_707IOF_N0041422ZCAM03169_1100LMA03.IMG
ZL0_0237_0687977581_733IOF_N0072050ZCAM03241_1100LMA02.IMG
ZL1_0237_0687977641_738IOF_N0072050ZCAM03241_1100LMA02.IMG
ZL2_0237_0687977652_723IOF_N0072050ZCAM03241_1100LMA02.IMG
ZL3_0237_0687977664_723IOF_N0072050ZCAM03241_1100LMA02.IMG
ZL4_0237_0687977675_724IOF_N0072050ZCAM03241_1100LMA02.IMG
ZL5_0237_0687977686_723IOF_N0072050ZCAM03241_1100LMA02.IMG
ZL6_0237_0687977697_738IOF_N0072050ZCAM03241_1100LMA02.IMG
ZR0_0237_0687977708_738IOF_N0072050ZCAM03241_1100LMA02.IMG
ZR1_0237_0687977742_738IOF_N0072050ZCAM03241_1100LMA02.IMG
ZR2_0237_0687977753_738IOF_N0072050ZCAM03241_1100LMA02.IMG
ZR3_0237_0687977766_738IOF_N0072050ZCAM03241_1100LMA02.IMG
ZR4_0237_0687977779_764IOF_N0072050ZCAM03241_1100LMA02.IMG
ZR5_0237_0687977793_723IOF_N0072050ZCAM03241_1100LMA02.IMG
ZR6_0237_0687977809_738IOF_N0072050ZCAM03241_1100LMA02.IMG

Figure S4C

ZL0_0162_0681324362_749RAD_N0060000ZCAM03197_1100LMA03.IMG
ZL0_0162_0681324559_774RAD_N0060000ZCAM03197_1100LMA06.IMG
ZL1_0162_0681324515_771RAD_N0060000ZCAM03197_1100LMA03.IMG
ZL1_0162_0681324588_763RAD_N0060000ZCAM03197_1100LMA03.IMG
ZL2_0162_0681324520_738RAD_N0060000ZCAM03197_1100LMA03.IMG
ZL2_0162_0681324595_764RAD_N0060000ZCAM03197_1100LMA03.IMG
ZL3_0162_0681324526_761RAD_N0060000ZCAM03197_1100LMA03.IMG
ZL3_0162_0681324602_764RAD_N0060000ZCAM03197_1100LMA03.IMG
ZL4_0162_0681324532_785RAD_N0060000ZCAM03197_1100LMA03.IMG
ZL4_0162_0681324609_738RAD_N0060000ZCAM03197_1100LMA03.IMG
ZL5_0162_0681324539_772RAD_N0060000ZCAM03197_1100LMA03.IMG
ZL5_0162_0681324616_765RAD_N0060000ZCAM03197_1100LMA03.IMG
ZL6_0162_0681324549_738RAD_N0060000ZCAM03197_1100LMA03.IMG
ZL6_0162_0681324623_738RAD_N0060000ZCAM03197_1100LMA03.IMG
ZR0_0162_0681324362_749RAD_N0060000ZCAM03197_1100LMA03.IMG
ZR0_0162_0681324630_764RAD_N0060000ZCAM03197_1100LMA04.IMG
ZR1_0162_0681324515_771RAD_N0060000ZCAM03197_1100LMA03.IMG
ZR1_0162_0681324659_770RAD_N0060000ZCAM03197_1100LMA03.IMG

ZR2_0162_0681324520_738RAD_N0060000ZCAM03197_1100LMA03.IMG
ZR2_0162_0681324667_764RAD_N0060000ZCAM03197_1100LMA03.IMG
ZR3_0162_0681324526_761RAD_N0060000ZCAM03197_1100LMA03.IMG
ZR3_0162_0681324674_770RAD_N0060000ZCAM03197_1100LMA03.IMG
ZR4_0162_0681324532_785RAD_N0060000ZCAM03197_1100LMA03.IMG
ZR4_0162_0681324681_771RAD_N0060000ZCAM03197_1100LMA03.IMG
ZR5_0162_0681324539_772RAD_N0060000ZCAM03197_1100LMA03.IMG
ZR5_0162_0681324689_773RAD_N0060000ZCAM03197_1100LMA03.IMG
ZR6_0162_0681324549_738RAD_N0060000ZCAM03197_1100LMA03.IMG
ZR6_0162_0681324698_771RAD_N0060000ZCAM03197_1100LMA03.IMG
Figure S4D
ZL0_0123_0677860755_718RAD_N0041422ZCAM03169_1100LMA03.IMG
ZL1_0123_0677860813_707RAD_N0041422ZCAM03169_1100LMA03.IMG
ZL2_0123_0677860826_724RAD_N0041422ZCAM03169_1100LMA03.IMG
ZL3_0123_0677860838_723RAD_N0041422ZCAM03169_1100LMA03.IMG
ZL4_0123_0677860850_723RAD_N0041422ZCAM03169_1100LMA03.IMG
ZL5_0123_0677860863_707RAD_N0041422ZCAM03169_1100LMA03.IMG
ZL6_0123_0677860875_723RAD_N0041422ZCAM03169_1100LMA03.IMG
ZR0_0123_0677860887_723RAD_N0041422ZCAM03169_1100LMA03.IMG
ZR1_0123_0677860928_724RAD_N0041422ZCAM03169_1100LMA05.IMG
ZR2_0123_0677860941_723RAD_N0041422ZCAM03169_1100LMA03.IMG
ZR3_0123_0677860956_724RAD_N0041422ZCAM03169_1100LMA03.IMG
ZR4_0123_0677860972_724RAD_N0041422ZCAM03169_1100LMA03.IMG
ZR5_0123_0677860988_707RAD_N0041422ZCAM03169_1100LMA03.IMG
ZR6_0123_0677861006_707RAD_N0041422ZCAM03169_1100LMA03.IMG
Figure S4E
ZL0_0237_0687977581_733RAD_N0072050ZCAM03241_1100LMA02.IMG
ZL1_0237_0687977641_738RAD_N0072050ZCAM03241_1100LMA02.IMG
ZL2_0237_0687977652_723RAD_N0072050ZCAM03241_1100LMA02.IMG
ZL3_0237_0687977664_723RAD_N0072050ZCAM03241_1100LMA02.IMG
ZL4_0237_0687977675_724RAD_N0072050ZCAM03241_1100LMA02.IMG
ZL5_0237_0687977686_723RAD_N0072050ZCAM03241_1100LMA02.IMG
ZL6_0237_0687977697_738RAD_N0072050ZCAM03241_1100LMA02.IMG
ZR0_0237_0687977708_738RAD_N0072050ZCAM03241_1100LMA02.IMG
ZR1_0237_0687977742_738RAD_N0072050ZCAM03241_1100LMA02.IMG
ZR2_0237_0687977753_738RAD_N0072050ZCAM03241_1100LMA02.IMG
ZR3_0237_0687977766_738RAD_N0072050ZCAM03241_1100LMA02.IMG
ZR4_0237_0687977779_764RAD_N0072050ZCAM03241_1100LMA02.IMG
ZR5_0237_0687977793_723RAD_N0072050ZCAM03241_1100LMA02.IMG
ZR6_0237_0687977809_738RAD_N0072050ZCAM03241_1100LMA02.IMG

Figure S6 Supercam PDS data bundle (*78*), Derived Spectra data collection. Máaz spectrum is the median spectrum from all rock targets through Sol 153. Séitah spectrum is the median spectrum taken on rock targets between Sols 202 and 259.

Figure S7 SHERLOC PDS data bundle (*77*) Processed Spectroscopy data collection, Sol 162 (Guillaumes), Sol 208 (Garde) and Sol 269 (Dourbes).

Figure S8 and Tables S1 and S2 Supercam PDS data bundle (*78*), Derived Spectra data collection. Máaz data are mean of all rock targets through Sol 153. Séitah data are mean of all rock targets between Sols 202 and 259. PIXL PDS data bundle (*75*), Processed data collection. Guillaumes, Bellegarde, and Dourbes abrasion patch data listed under sols 167, 196, and 269, respectively.

Figure S9 - same sources as Figure 5.